Near Critical Density Laser Beat-Wave Acceleration for Radiotherapy Applications

by

Carlton Sangmin Kim

A thesis submitted in partial fulfilment of the requirements for the degree of

Master of Science

Department of Physics

University of Alberta

Abstract

This thesis examines 2D Particle-in-Cell (PIC) simulations of a beat-wave interacting with a Near-Critical Density (NCD) plasma to generate an electron beam suitable for radiotherapy. The beat-wave is generated from the co-propagation of an 800nm laser, the primary laser, and a 400nm laser, the secondary laser. The lasers are simulated with a pulse duration of 35 fs and a respective energy of 100 mJ each. A beat-wave is used due to the desirability of a compact setup appropriate in a medical environment. Beat-wave accelerators have historically been used when the typical high-intensity lasers used to reach the bubble-regime were not accessible, as the beat-wave is able to accelerate electrons in the plasma with relatively low intensity. Additionally, NCD plasmas are examined to enhance the charge generated from the interaction while limiting the maximum energy gain of the electrons. The lasers are examined with both linear and circular polarization to examine the polarization effect on overall charge and electron energy gain.

The beat-wave is compared to the propagation of the primary laser alone and is found to better propagate through NCD plasmas. The single laser is only able to form cavitons in the first half of the plasma and does not lead to a peak of MeV electrons. Additionally, the limiting of the energy differs from typical, high-energy laser acceleration setups due to the different energy range used in radiotherapy. Linear accelerators currently used for electron radiotherapy generate electron beams with energies from 5-25 MeV and a dose rate of 1-10 Gy/min. The NCD plasma interactions lead to MeV order electrons which meet the energy and dose requirements set by linear accelerators and show aptitude for high-dose rate electron radiotherapy applications.

Acknowledgements

Table of Contents

List of Tables

List of Figures

Chapter 1 - Introduction and Background Theory

1.1 Development of Particle Accelerators

Particle accelerators were developed as a way of allowing study of high-energy physics unachievable through radiation sources available in earlier stages of the field. One of the earliest particle accelerators was developed by Cockcroft and Walton in 1932 [1]. Their device creates an electric field through an electrode of 400 kV at the entrance of a hydrogen proton source, 200 kV at the middle of an accelerating tube, and a ground state electrode at the target position [1] to create an accelerating column for protons. While the development of this method led to great discoveries and a Nobel Prize in 1951, the device is limited in application due to discharge created from breakdown of the surrounding air. To surpass this limitation, Ernst Ising in 1924 proposed acceleration of particles by utilizing fields alternating in time [1]. Accelerators using this method are known as Radiofrequency (RF) Linear Accelerators or as a LINAC. LINACs consist of a linear accelerating structure lined with a series of cavities that confine electromagnetic fields and cause their oscillation [3]. These fields accelerate particles forward given they cross through the accelerating fields at a time when it is properly polarized. LINACs were developed to generate an acceleration gradient of 100 MV/m[4]. One of the most prominent LINACs currently in use is at the Stanford Linear Accelerator Laboratory (SLAC). The SLAC accelerator extends 3.2 km and can generate electron beams with an energy of 50 GeV [1]. However, the widespread usage of LINACs is also limited by the amount of space needed to accelerate to high energies. Similarly, usage is limited by the cost required to build large scale devices. A higher acceleration gradient is desired, as it would allow a more compact and cheaper setup; LINACs cannot achieve such a feat due to the material breakdown limitation of voltage

applied to the equipment. As such, alternate forms of acceleration are continually being researched.

1.2 Laser-Plasma Acceleration

In 1979, Tajima and Dawson proposed the idea of Laser Wakefield Acceleration (LWFA) [7] – a means of using plasma as an acceleration medium to surpass LINACs by overcoming the material breakdown limitation. Because of this limitation, LINACs can support accelerating fields of up to 100 MV/m [4]. However, plasma exists in a broken-down state and can thus support large fields without experiencing breakdown which limits the acceleration. Through LWFA, acceleration gradients of 100 GV/m are obtained and lead to considerably smaller scale experimental setups to achieve similar electron energies as LINACs. LWFA occurs when a laser pulse propagates into a sufficiently underdense plasma. The ponderomotive force of the laser, a nonlinear effect, pushes electrons within the plasma towards areas of lower intensity while ions stay relatively stationary. This allows the laser to couple to the plasma by forming a wave in the plasma resembling a train of wakes. These wakes serve as accelerating structures within the plasma and trap many of the electrons within them, as a region of deceleration also exists. However, electrons can use the wakes as regions of acceleration if they begin with enough energy to move beyond the decelerating regions behind the driving pulse. An early scheme to achieve LWFA examined the interaction between a beat-wave generated from two co-propagating laser pulses with an underdense plasma [7]. The two lasers are chosen to beat at or near the frequency of the plasma to resonantly excite a plasma and induce acceleration. With great advances in laser technology, however, the most studied interaction is between an underdense plasma with a single intense, ultrashort laser pulse.

The accelerating field strength within the plasma depends on the density perturbation created by the laser; with a stronger laser, a sharper density gradient can be formed within the plasma. When the field is sufficiently strong, the electrons trapped in the wakes can accelerate to velocities higher than the phase velocity of the plasma wave. When this happens, the wake breaks down and leads to a phenomenon known as wave-breaking [4]. When wave-breaking occurs, bulk electrons are self-injected and accelerated in addition to the low population of high-energy electrons. Wave-breaking thus leads to an electron beam with a high energy spread rather than a monoenergetic beam. However, as injection caused by wave-breaking allows bulk electrons to accelerate, a high-charge beam can form. It can thus be considered that a trade-off between charge and maximum energy exists in this specific injection method.

Most LWFA experimental setups use plasmas with density on the order of 10^{18}-10^{19} cm^{-3} for the purpose of creating high energy, monoenergetic beams. A separate regime involves raising the density which allows the laser to excite a plasma wave with a lower phase velocity and can therefore couple to the bulk of a plasma. In such a medium, the acceleration mechanism no longer resembles the clean form visible in LWFA but transitions to a more turbulent interaction. By taking advantage of a higher-density interaction, a greater charge electron beam can be generated. While this beam will not have the GeV scale, monoenergetic beam desired in high-energy physics research, such a scheme would serve applications requiring high charge with MeV order electrons instead.

Aside from high-energy physics, a major application of accelerators is the use of comparatively lower energy electrons for radiotherapy. Particle beams generated by accelerators target cancer cells in a patient, which are then removed by the human body once the radiation damages the DNA of the cancer cells [9]. X-rays are typically used in different forms of

radiotherapy due to their ability to penetrate into the body to target deep-seated tumors using equipment which is readily available. Proton beams are used to similarly target deep-seated tumors and potentially decrease the level of radiation damage done to surrounding tissue [9]. Electron beams lead to radiation which is comparatively shallower than proton and x-ray based radiotherapy devices. Electrons are more suitable in treating shallow cancers, such as that of the skin, as they cannot penetrate further into the body but will not damage healthy tissue beyond the human exterior during treatment [9].

1.3 Objective

This thesis seeks to optimize a potential laser-plasma acceleration scheme for the application of electron radiotherapy. Allowing the transition from LINACs to laser-plasma accelerators would allow for a more compact setup which could conserve space and cost, and potentially making the machinery less imposing from the perspective of a patient. Current electron radiotherapy equipment generates electrons on the order of 5-25 MeV [10]. As such, a near-critical density (NCD) plasma is used to generate these electron energies. This work utilizes a Particle-in-Cell (PIC) simulation model to examine the interaction between a single laser and a laser beat-wave with a near-critical density plasma as a potential setup for an electron radiotherapy accelerator. The higher density effects were examined by scanning through densities approaching the critical density. The results point towards the beat-wave setup which allows for further propagation of the pulses into a NCD plasma compared to a single pulse despite similar overall intensities. The beat-wave proves especially advantageous in selectively generating MeV order electrons. In addition to optimization, the acceleration mechanism in this interaction is analyzed due to transition to higher densities having indicators of differing acceleration mechanisms.

Chapter 2 - Theoretical Background

2.1 Plasma Equations

To understand plasma as a combination of individual and collective behavior, equations are formed using both particle and fluid approximations of plasma. In a fluid description considering two or more particle types, such as ions and electrons, the plasma is treated as two different fluids mixing together. In this description, the individual particle velocity $\vec{v}$ is replaced with a fluid velocity, $\vec{u}$, which represents the velocity of an element of the fluid.
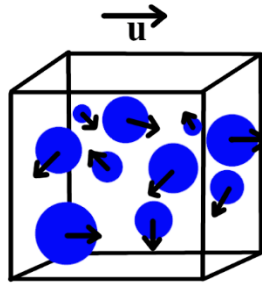
Figure 2.1: Example of differential fluid element with collection of particles with individual velocities represented by a singular fluid velocity, u.

The fluid description is generally insufficient in capturing complicated behavior in plasma and thus moves onward into a more complete, kinetic description. In the kinetic description, each particle species adheres to a Maxwellian distribution, $f(\vec{v})$ [12]:

$$f(\vec{v}) = \left[\frac{m}{2\pi k_b T}\right]^{\frac{3}{2}} \exp\left(-\frac{mv^2}{2k_b T}\right) = \left[\frac{m}{2\pi k_b T}\right]^{\frac{3}{2}} \exp\left(-\frac{v^2}{v_{th}^2}\right) \quad (2.8)$$
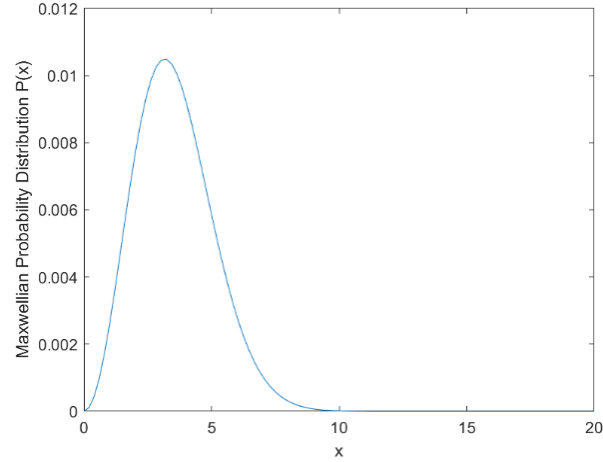
Figure 2.2: Example of a Maxwellian distribution.

where $\vec{v}$ is the three-dimensional velocity vector, m is the mass of the particle species, k_b is the

Boltzmann constant, T is the species temperature, and v_{th} is the thermal velocity defined as:

$$v_{th} \equiv \sqrt{\frac{2k_b T}{m}} \ (2.9).$$

This distribution function, plotted in Figure 2.2, is used in conjunction with the Boltzmann

equation to relate the distribution to the effects from external forces and collision effects and is

given as [12]:

$$\frac{\partial f}{\partial t} + \vec{v} \cdot \nabla f + \frac{q(\vec{E} + \vec{v} \times \vec{B})}{m} \cdot \frac{\partial f}{\partial v} = \left(\frac{\partial f}{\partial t}\right)_c (2.10)$$

Where the term involving E and B represent the effect of electromagnetic fields, and the right-

hand term represents temporal collisional effects. In a collisionless plasma, the right-hand term

can be neglected.

From taking moments through integration of the Boltzmann equation, the fluid equations

of plasma are obtained [12, 13]:

$$\frac{\partial n}{\partial t} + \nabla \cdot (n\vec{u}) = 0 \quad \textit{Zeroth Moment: Continuity Equation (2.11a)}$$

$$mn\frac{\partial \vec{u}}{\partial t} + mn\overrightarrow{(u \cdot \nabla)}\vec{u} = qn(\vec{E} + \vec{u} \times \vec{B}) - \nabla p \quad \textit{First Moment: Equation of Motion (2.11b)}$$

$$\left(\frac{\partial}{\partial t} + \vec{u} \cdot \nabla\right)\frac{p}{n^\gamma} = 0 \quad \textit{Second Moment: Equation of State (2.11c)}$$

With $\vec{u}$ representing the fluid velocity of the particle species, n the number density, p the pressure of the fluid, and γ the term relating the number of degrees of freedom.

From the plasma equations, paired with a physical description, the oscillatory behavior of plasma is derived; the evolution of an initial push on the plasma converting into an oscillation is shown in Figure 2.3. In a plasma consisting of ions and electrons, motion of ions relative to electrons can be considered stationary due to the longer response times and higher mass of the ions. The ions are thus considered stationary when the electron density is perturbed. The electrons push forward from perturbation and create a space-charge gradient as the electrons pile together. This charge imbalance creates a reactionary electric field which pulls the electrons back towards their initial position. However, the inertia of the electrons in motion cause them to move beyond their initial position of equilibrium which causes another space-charge gradient. This converts into an oscillation of the electrons about their initial equilibrium point and represents the parameter known as the plasma frequency. The plasma equations can be linearized through treating the density, velocities, and fields as equilibrium terms with perturbations added on, e.g.:

$$n = n_0 + n_1 \quad (2.12)$$

where n_0 is the initial density at equilibrium, and n_1 is the treated as an oscillatory perturbation such that $n_1 = n_1 \exp[i(kx - \omega t)]$ [12,13] and $n_1 \ll n_0$. Using the linearized equations, the plasma frequency is found as:

$$\omega_p = \sqrt{\frac{n_0 e^2}{\epsilon_0 m_e}} \ (2.13)$$
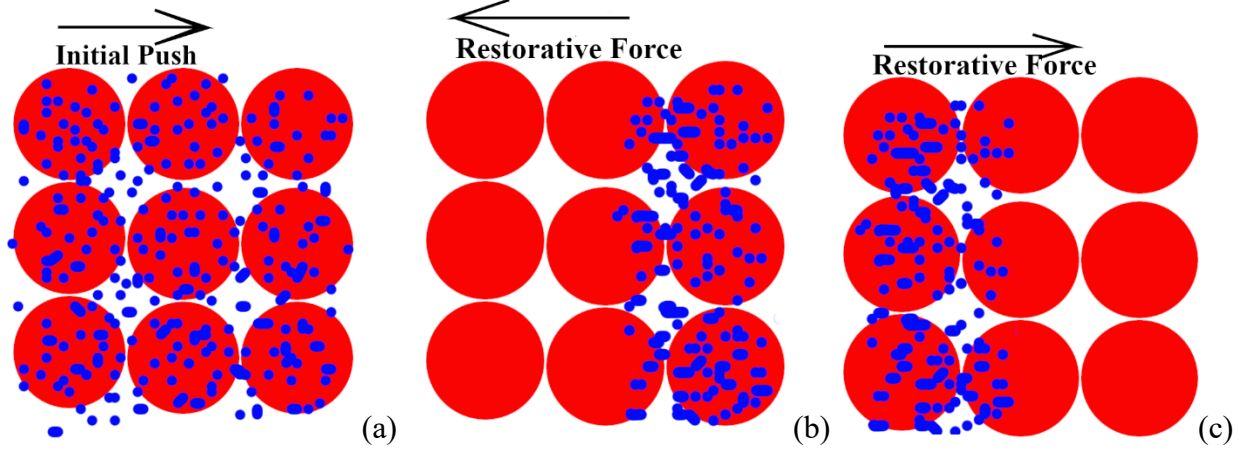
Figure 2.3: (a) Plasma at equilibrium with a background of ions in red and electrons in blue experiences force pushing electrons forward. (b) Space charge imbalance creates a restorative force on the electrons. (c) Electrons overshoot equilibrium and experience restorative force once again and converts to an oscillation.

From the Vlasov equation, the dispersion relation of electron plasma waves is derived:

$$\omega^2 = \omega_p^2 + \frac{3}{2} k^2 v_{th}^2 \ (2.14)$$

The field generated by each particle has an effective range caused by shielding from other particles called the Debye screening length, λ_{Debye}. The Poisson equation solves for the electric potential:

$$\nabla^2 \phi = -\frac{\rho}{\epsilon_0} \ (2.15)$$

where ϕ is the electric potential and ρ is the charge density. Using this, ϕ is found to be [13]:

$$\phi = \frac{q}{r} \exp\left[-\frac{r}{\lambda_{Debye}}\right] \ (2.16)$$

With the Debye length found to be:

$$\lambda_{Debye} = \sqrt{\frac{\epsilon_0 k_b T}{ne^2}} \ (2.17)$$

From (2.16) and (2.17), the effect of the Debye length is visible in that the potential drops drastically beyond the Debye length. This illustrates the collective effect of particle shielding and shows that the particles affect each other only within the range of the Debye length.

2.2 Laser Interaction with Plasma

With the groundwork for plasma behavior when experiencing small perturbations, interactions with a propagating electromagnetic wave can be analyzed.

2.2.1 Gaussian Laser Pulses

The electromagnetic waves in lasers are described through Maxwell's equations which derive relationships in interactions from charge and electromagnetic waves. Maxwell's equations are given in differential form as [11]:

$$\nabla \cdot \vec{E} = \frac{\rho}{\epsilon_0} \quad (2.3a) \qquad\qquad \nabla \cdot \vec{B} = 0 \quad (2.3b)$$

$$\nabla \times \vec{E} = -\frac{\partial B}{\partial t} \ (2.3c) \qquad \nabla \times \vec{B} = \mu_0 \epsilon_0 \frac{\partial \vec{E}}{\partial t} + \mu_0 \vec{J} \ (2.3d)$$

where ρ is the charge density of the medium, ϵ_0 is the permittivity of free space, μ_0 is the permeability of free space, and $\vec{J}$ is the current density present in the medium. From Maxwell's equations, the E and B fields are solved and presented in potential form through a scalar potential, ϕ, and vector potential, $\vec{A}$ [11]:

$$\vec{E} = -\nabla \phi - \frac{\partial \vec{A}}{\partial t} \ (2.4a) \qquad \vec{B} = \nabla \times \vec{A} \ (2.4b)$$

9

The normalized vector potential, a_0, is a frequently used parameter in laser physics to indicate the strength of a laser and is defined as:

$$\vec{a} = \frac{e\vec{A}}{m_e c} \ (2.5a) \qquad\qquad a_0 = \frac{e|E_0|}{m_e \omega_L c} = 0.85 \times \sqrt{I \left[\frac{W}{cm^2}\right]} \times \lambda_L [\mu m] \ (2.5b)$$

with e as the charge of an electron, m_e the mass of an electron, E as the electric field strength of the laser, ω_L and λ_L the laser frequency and wavelength, and I as the intensity of the laser.

The primary focus of this work is analyzing the interaction between a Gaussian laser pulse and plasma. A Gaussian pulse propagating in the z-direction is presented in Figure 2.4 and with the equation [4,14]:

$$\vec{E}(r,z,t) = \frac{E_0}{2} \exp\left[-\frac{r^2}{w(z)^2}\right] \exp\left[-\frac{\left(t-\frac{z}{c}\right)^2}{\tau_0^2}\right] \cos(\omega_L t - k_L z + \phi_L)\, \vec{e}_{pol} (2.18)$$

$$w(z) = w_0 \sqrt{1 + \left(\frac{z}{z_R}\right)^2} (2.19)$$

$$z_R = \frac{\pi w_0^2}{\lambda_L} \ (2.20)$$

E_0 is the peak electric field of the laser, r is the radial distance from the axis of propagation; $w(z)$ is the waist width of the beam as it propagates with w_0 representing the initial beam width; τ_0 as an indicator of the pulse duration; ω_L and k_L represent the frequency and wavenumber of the laser respectively; ϕ_L is the phase of the laser; and $\vec{e}_{pol}$ is the polarization vector of the pulse, which can change depending on whether the pulse is linearly, circularly, or elliptically polarized. Additionally, z_R is defined as the Rayleigh length. The Rayleigh length indicates how far a pulse can propagate until defocusing effects grow and intensity becomes markedly weaker where the beam waist becomes $w = \sqrt{2}w_0$.
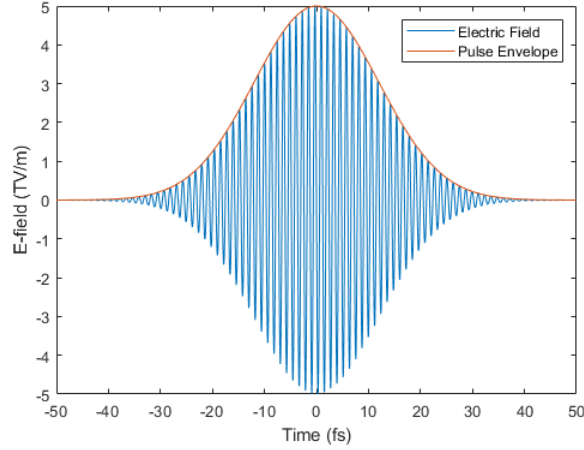
Figure 2.4: Temporal profile of a gaussian pulse with $t_{fwhm} = 30\ fs$.

Further parameters of importance in laser considerations are the peak intensity and power of the pulse, which are given as [4]:

$$I_0 = 0.83 \frac{W_L}{t_{fwhm} d_{fwhm}^2} \text{ (2.21a)} \qquad P_0 = 0.94 \frac{W_L}{t_{fwhm}} \text{ (2.21b)}$$

W_L is the energy of the laser used, d_{fwhm} is the spot size of the laser, and t_{fwhm} is the pulse duration of the laser, where d_{fwhm} and t_{fwhm} are defined as:

$$d_{fwhm} = \sqrt{2\ln(2)} w_0 \text{ (2.22a)} \qquad t_{fwhm} = \sqrt{2\ln(2)} \tau_0 \text{ (2.22b)}$$

2.2.2 Laser Propagation

The dispersion relation of an electromagnetic wave propagating into a plasma is given as:

$$\omega^2 = \omega_p^2 + c^2 k^2 \text{ (2.23)}$$

where c is the speed of light, and ω and k are the frequency and wavenumber of the electromagnetic wave respectively. For a laser, the condition $\omega_p = \omega$ leads to a solution of a density known as the critical density, given from using (2.23) with (2.13) as:

11

$$n_c = \frac{\omega^2 \epsilon_0 m_e}{e^2} \ (2.24)$$

When $n > n_c$, the plasma is called an overdense plasma and cause the incident laser to fully

reflect from the surface. The phase and group velocities of waves are known to be:

$$v_{ph} = \frac{\omega}{k} \ (2.25a) \quad v_{group} = \frac{\partial \omega}{\partial k} \ (2.25b)$$

From these relations, an underdense plasma is found to have a higher v_{ph} than in higher density

plasmas. The high phase velocity waves only couple to the portion of electron population on the

tail-end of the distribution with similarly high velocities. When $n \geq n_c$, the phase velocity of the

excited plasma wave approaches v_{th} and interacts with the bulk of the plasma. In such a

condition, the generated wave has a much smaller wavenumber and appears as a sheath structure.

The ponderomotive force of a laser, which serves as the main coupling mechanism of a laser to a

plasma, is determined by the gradient of the electric field of the laser. For a Gaussian pulse, it is

given as $\vec{F}_p = -m_e c^2 \nabla a$ (2.25) [4]. From the ponderomotive force, the ponderomotive potential

takes the form [4,7,13]:

$$\phi_{pond} = mc^2(\sqrt{1 + a_0^2} - 1) \ (2.26)$$

Using the ponderomotive potential, the expected energy gain supplied directly by the laser is

derived.

Energy gain in a laser-plasma accelerator is limited by a characteristic length of

acceleration called the dephasing length, L_d. The dephasing length describes the length electrons

trapped in the laser wakes travel before experiencing deceleration. This deceleration occurs when

the electrons are accelerated to velocities approaching and greater than the plasma wave v_{ph}.

When the electrons move past the plasma wave, they enter the positive regions of the plasma wave which serve to decelerate them. L_d is given as [4]:

$$L_d = \frac{\lambda_p}{2} \frac{\omega_L^2}{\omega_p^2} \quad (2.27)$$

Laser-plasma accelerators optimize energy gain through increasing the dephasing length based on its density dependence. A separate characteristic length is called the pump depletion length, L_{pd}, which describes the length along a plasma the laser can travel and transfer energy to the plasma through a plasma wave and is given as [4]:

$$L_{pd} = \frac{\omega_L^2}{\omega_p^2} \frac{c\tau_L}{a_0^2} \quad (2.28)$$

In underdense plasmas, the pump depletion length becomes the main limiting factor of acceleration in the relativistic regime of $a_0 > 1$, while the dephasing length dominates in the linear regime. However, the dephasing length is the dominating term in near-critical and above interactions.

The energy gain formula depends on the acceleration length, as it follows an integration of the longitudinal fields in the direction of the acceleration length. The formula for a relativistic interaction is found to be [4, 7]:

$$\Delta W = \frac{2}{3} m_e c^2 a_0 \frac{\omega_L^2}{\omega_p^2} \quad (2.29)$$

2.2.3 Beat-wave Advantages

The laser beat-wave setup utilizes two co-propagating lasers which beat at the plasma frequency. Therefore, their frequencies must adhere to the condition:

$$\omega_p = |\omega_{L1} - \omega_{L2}| = \omega_{beat} \quad (4.1)$$

where ω_{L1} and ω_{L2} correspond to the frequencies of the first and second lasers respectively. By matching this condition, the beat-wave resonantly excites a plasma wave to facilitate acceleration. Beat-waves have typically been used in the long-pulse, relatively low intensity regime [56, 79]. The beat-wave setup allows for efficient plasma wave generation with lower energies compared to single lasers used to achieve wakefield conditions. Additionally, the higher frequency laser has a larger critical density value. This larger limit means the higher frequency laser creating the beat-wave propagates through NCD plasmas of the lower frequency laser without facing the same limitation. As such, the beat-wave propagates with little disruption in NCD plasmas compared to usage of the single, lower frequency laser alone.

2.3 Instabilities

Instabilities in laser-plasma interactions arise when a laser propagates and excites a wave in a plasma which grows and evolves continuously until it can no longer be supported by the plasma. The plasma instabilities discussed in this text are the Raman (scattering) instability and modulational instability. These instabilities are important to study especially in the NCD regime. The Raman scattering density limit outlined in section 2.3.1 is reached, and the effect of its absence is seen in higher density interactions. Additionally, modulational instability occurs in higher density interactions from the generation of a large amplitude electrostatic (or Langmuir) wave from the propagation of the beat-wave.

2.3.1 Raman Scattering

Raman scattering describes the phenomenon of a laser propagating into a plasma and resulting in a plasmon (plasma oscillation) and a scattered light wave. The conservation of momentum thus demands the relationship:

$$\omega_L = \omega_1 + \left(\omega_p + 3k^2 v_e^2\right)^{\frac{1}{2}} \quad (2.30a)$$

$$k_L = k_1 + k_p \quad (2.30b)$$

where ω_1 and k_1 correspond to the frequency and wavenumber of the scattered light wave and v_e is the velocity of the electrons. The instability arises when an incident electric field forms a plasma wave presented as density perturbations along the laser axis. The plasma wave forms a scattered light wave through the generated current of the moving charge. The generated light then creates its own density perturbation, which continues to evolve and form the instability. The dispersion relation illustrating this interaction is derived to be [13]:

$$\omega^2 - \omega_p^2 - 3k^2 v_e^2 = \frac{\omega^2 k^2 v_{os}^2}{4} \left[\frac{1}{D(\omega - \omega_L, k - k_L)} + \frac{1}{D(\omega + \omega_L, k + k_L)}\right] \quad (2.31)$$

v_{os} is the oscillatory velocity of electrons moving within the field of the light, and $D(\omega,k)$ is the dispersion function. The dispersion relation shows intervals of the dispersion function $\pm\omega_L$ to reflect the fact that only modes close to the original frequency are supported by the plasma; these modes are also called the Stokes and Anti-Stokes. When considering the dispersion relation (2.31), Raman scattering is found to require a plasma density of $n \leq \frac{n_{cr}}{4}$.

2.3.2 Modulational Instability and Cavitons

A modulational instability in plasma arises from a large amplitude Langmuir wave decaying into several different plasma modes [13,16,17]. The plasma waves are non-uniform and

cause electrons to move towards regions where the wave is weaker. High frequency plasma waves are then trapped within a region of comparatively lower density. The wave becomes so impactful that ions begin moving in response towards regions of weaker wave amplitude. The ion density disturbance then modulates the wave trapped in the low-density region such that the non-uniformity increases. This in turn strengthens the effect on ions and continues in a feedback loop to serve as the instability.

One outcome of the modulational instability which is visible in the NCD plasma interactions presented in this work is the formation of a caviton. A caviton is visible in the density profile of a plasma as a density cavity surrounded by regions of higher density. The caviton traps high-frequency plasma waves within its density depression and amplifies the resulting field. The cavitons continue widening until they reach a length on the order of $10 - 20 \, \lambda_{Debye}$ [13]. After reaching this point, the caviton structures break down which strongly impacts the ions. The caviton breakdown thus leads to the formation of a longitudinal ion wave known as an Ion Acoustic Wave [13].

Chapter 3 - Computational Method

The results shown in this work are results of computational studies conducted using the Particle-in-Cell (PIC) code EPOCH to simulate laser-plasma interactions. EPOCH is a PIC code chosen due to its flexibility derived from its nature as an open-source code. To ensure the code properly captures the physics of the interaction, a sufficient understanding of the code is required.

In plasma physics, computational solvers generally fall into two categories: fluid and kinetic. Fluid-based codes examine and solve the magnetohydrodynamic (MHD) equations. MHD codes are most frequently used in research studying large-scale plasmas with complex fields, such as in astrophysics or magnetic fusion devices [18]. Kinetic codes further branch into codes solving either the Vlasov and Fokker-Planck (VFP) equations or using the PIC method. PIC codes begin simulations by initializing macroparticles on a defined grid with fields driving into the plasma. Macroparticles, also called superparticles, are single particles representing the averaged characteristics of larger collection of smaller particles and serve to enhance computational efficiency. At each time step, the relativistic equations of motion are solved for the particles individually using the values of the field at that moment in time. Once the next positions and velocities are determined, the charge and current densities of the plasma species are calculated and collected onto the grid points or nodes. Using these variables, the fields are re-calculated using Maxwell's equations and interpolated to the particle positions to find the force acting upon them. With the new force and fields, the next process repeats at the next time step. VFP codes have an advantage over PIC codes in that PIC approaches require careful consideration of grid spacing and number of particles in each cell, while VFP codes do not

require such parameters. However, PIC codes are often the code of choice in laser-plasma interactions due to high flexibility and low computational costs, especially compared to VFP codes [19].

3.1 Particle-in-Cell Method

3.1.1 Particle-Push Algorithm

The PIC method starts off by solving the equation of motion for the particles represented as:

$$m\frac{d\vec{v}}{dt} = \vec{F} \quad (3.1a)$$

$$\frac{d\vec{x}}{dt} = \vec{v} \quad (3.1b)$$

To solve through a known sequence of time, a finite-difference method is used. The finite-difference method replaces the derivatives in the equations of motion with discrete values based on the old values of velocity and position with the length of the time step. The equations then take the form:

$$m\frac{v_{n+1} - v_n}{\Delta t} = \vec{F}_n \quad (3.2a)$$

$$\frac{x_{n+1} - x_n}{\Delta t} = \vec{v}_{n+1} \quad (3.2b)$$

The subscripts of the variables represent the timesteps taken, where Δt is length of the time step, and $n + 1$ shows the value of the variable at the next time step. PIC codes utilize a finite-difference method known as the Leap Frog method [18,19]. The leap-frog method utilizes time steps that are taken at the half-points rather than integer points for the velocity.
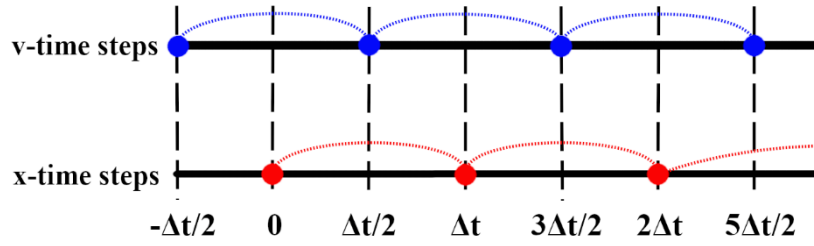
Figure 3.1: Time-steps of the leap-frog method, where the velocity is calculated at the half intervals while the position is at integer intervals.

The code takes in the initial values presented for particle positions, velocities, and electromagnetic forces. From the force values, the velocity at a regressed time step of $n - \frac{1}{2}$ is calculated. The equation of motion at the first step uses the initialized positions and forces to calculate the velocity at the next half time step, $v_{n+\frac{1}{2}}$. The equations of motion reflecting this method are therefore:

$$m \frac{v_{n+\frac{1}{2}} - v_{n-\frac{1}{2}}}{\Delta t} = \vec{F}_n \ (3.3a) \qquad \text{and} \qquad \frac{x_{n+1} - x_n}{\Delta t} = v_{n+\frac{1}{2}} \ (3.3b)$$

The leap-frog method is a desirable computational method due to its symmetry in time. In other words: if the simulation results are taken at a time step much later than the beginning, it could be retraced back to the original starting conditions showing a proper adherence to the conservation of energy.

3.1.2 Field Solver Algorithm

To obtain the electromagnetic fields in the plasma, the charge density is required as a component of Maxwell's equations. The charge density is used with Poisson's equation to calculate the potential within the boundaries specified in the code. To solve the Poisson's

equation in a PIC code, a finite-difference method is employed. When considering a 1D interaction, the equation takes the form [18,19]:

$$\frac{\partial^2 \phi_i}{\partial x^2} = \frac{\phi_{i-1} - 2\phi_i + \phi_{i+1}}{\Delta x^2} = -\frac{\rho}{\epsilon_0} \ (3.4)$$

where the index "i" is illustrated in figure 3.2 as the spatial index of the nodes, and Δx is the distance between nodes.
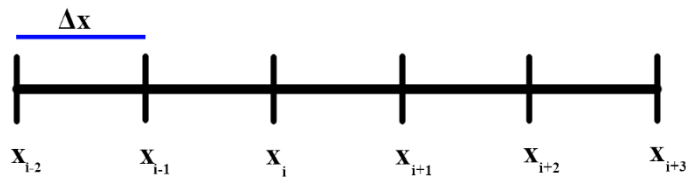
Figure 3.2: 1D spatial grid of nodes separated by a spacing of Δx.

With the derived electric potential, the electric field can be calculated using Faraday's law (2.3c) assuming a static magnetic field. In this case, the electric field follows $\vec{E} = \vec{\nabla}\phi$ or $E = \frac{\partial \phi}{\partial x}$ (3.5) in a 1D case. This differential equation is also solved using a finite-difference method to take the form [19]:

$$E_i = \frac{\phi_{i-1} - \phi_{i+1}}{2\Delta x} \ (3.6)$$

While this differential equation is rather trivial to solve for most of the nodes, the problem becomes difficult at the boundaries of the grid without knowing the boundary conditions. With the electric field at each point solved, the fields are interpolated to the particle positions in each cell. This interpolation works using particle weighting, which connects the discretized quantities such as field to the continuous positions of the particles.

20

3.1.3 Particle Weighting

PIC codes require weighting to convert the continuous distribution of particles throughout the grid to values of charge density and force which are connected to the nodes of the grid. The weighting process applies cells to nodes nearest to them to lead to discrete values. In the simplest weighting process, all particles surrounding a node within a distance of $\frac{\Delta x}{2}$ are gathered and assigned to that point. Figure 3.3 illustrates the way in which this collection occurs.
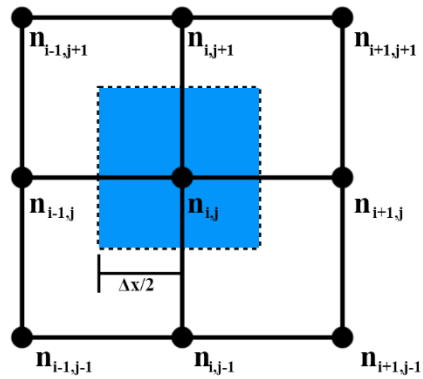
Figure 3.3: Grid of nodes separated by Δx; particles in the blue square are assigned to node $n_{i,j}$.

This method alone is insufficient due to noise generated from particles having drastically different effects when crossing the boundary to another node. This noise is especially evident in cases where there are an insufficient number of macroparticles. As such, this is considered a zeroth order weighting, and a first order weighting exists to decrease noise [19]. In first order weighting, the particles are collected onto all nodes surrounding it with fractional effects depending on the distance from the particle to the node.
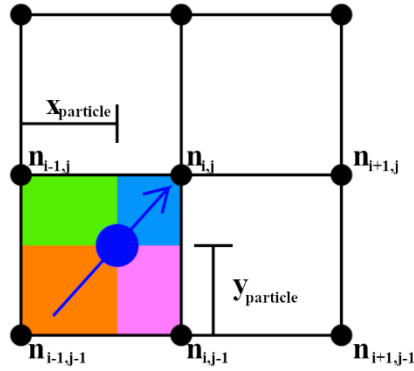
Figure 3.4: For weighting, areas of a cell are considered for each node; the fraction of the cell area occupied by the orange square is applied to node $n_{i,j}$, green square applied to $n_{i,j-1}$, etc.

Once weighting is conducted, the charge density can be calculated by taking the number of particles in the node, multiplying by the charge of the particle, then dividing by the node area. With the charge density now at each node, the electric field is calculated using the methods outlined in section 3.1.2. The fields from each node are interpolated onto the particles which are within a grid spacing length, and the entire process repeats through the time steps of the simulation. Higher order weighting methods exist but will expectedly increase computational costs.

Chapter 4 - Results

4.1 Parameters Examined

The focus of this work is to examine the interaction of a beat-wave with a NCD plasma to enhance the interaction and create an optimal electron beam for electron radiotherapy purposes. Due to the focus on application, the parameters chosen for the PIC simulations presented in this work are chosen to match a potential experimental setup.

In this work, the primary laser has a wavelength of 800 nm, while the second laser has a wavelength of 400 nm to reflect the generation of a frequency doubled harmonic of the primary laser. The energy of both lasers is set as $W_L = 100\ mJ$ when considering a beat-wave. In all simulations using the primary laser alone, $W_L = 200\ mJ$. The primary laser interaction is set with a higher energy to ensure that the total energy interacting with the plasma is the same across all cases. The pulse duration for both lasers in all cases is $t_{fwhm} = 35 fs$. The parameters which differ between the two lasers in the beat-wave case are listed in Table 4.1. The spot size for the primary laser is chosen to be $d_{fwhm} = 10\ \mu m$ as an experimentally obtainable size, while $d_{fwhm} = 5\mu m$ for the secondary laser due to effects of second harmonic generation in a realizable setup. The intensity for each laser is calculated using (2.21a). Additionally, the lasers are examined with both a linear polarization and circular polarization.

Table 4.1: Parameters for the primary and secondary laser.

	λ_{Laser}	$d_{fwhm}\ (\mu m)$	Intensity $[\frac{W}{cm^2}]$	a_0	$Critical\ Density, n_c [cm^{-3}]$
Primary	$800\ nm$	10	$2.5 * 10^{18}$	1.3	$1.7 * 10^{21}$

Secondary	400 nm	5	$9.7 * 10^{18}$	2.7	$6.8 * 10^{21}$

From these parameters, the condition (4.1) leads to a resonance condition when the density is equal to the critical density of the primary laser, which is $1.7 * 10^{21} cm^{-3}$.

This work examines 2D PIC simulation results to ensure effects which cannot be detected in 1D are properly captured. The box initialized by the PIC code is set to have a 40 μm width and 50 μm micron height. Each direction is divided into 1000 grid points which leads to a total of 1000000 grid points in the simulation with 100 particles simulated per cell. As a result, the longitudinal grid spacing, dx, is found to be 0.04 μm, while the transverse spacing, dy, is 0.05μm. The grid spacing in both directions is small enough to capture the physics of the laser, as evidenced by the spacing being much smaller than the laser wavelengths. Additionally, a probe is placed in the vacuum region at $x = 39\mu m$ to measure the characteristics of the particles passing through the plane of the probe and propagating beyond the plasma.

The plasma itself consists of both electrons and ions, where the electrons have a background temperature of $T_e = 10 \ eV$ while the ion temperature is negligible. The plasma density profile follows a gaussian distribution varying longitudinally with a full-width half maximum of 15 μm and centered about $x = 12.5 \ \mu m$. The length of 15 μm is chosen to match the dephasing length of the simulated lower density plasmas. This choice of length was also found to balance overall charge with the maximum energy for the higher density cases in initial, 1D simulations. The density profile is set as a Gaussian to capture effects when using a gas jet target and to examine the propagation of the fields and particles in vacuum. A visualization of this profile is shown in Figures 4.1 and 4.2. The peak of the density profiles is chosen to be NCD to enhance the coupling of the beat-wave to the plasma through the resonance condition (4.1).
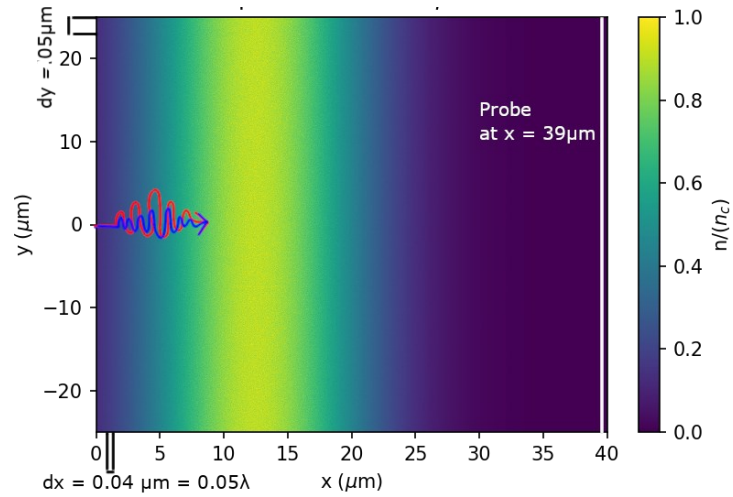
Figure 4.1: 2D presentation of the gaussian density profile varying longitudinally. The probe is at x=39 μm, and the primary and secondary lasers are in red and blue respectively.
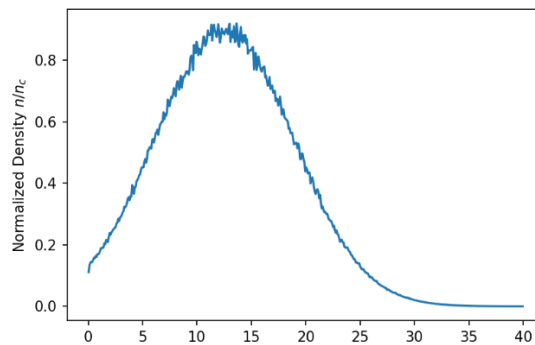
Figure 4.2: 1D cut of the 2D density profile taken across the laser axis, y = 0, for a profile with maximum density of $0.9n_c$.

4.2 Linearly Polarized Laser

4.2.1 Low Density Case

4.2.1a Single Laser Interaction

The first case presented is a plasma with density $n = 0.1n_c = 1.7 * 10^{20} cm^{-3}$ interacting only with the primary laser. This density is chosen to examine the behavior at a density one order below the critical and determine when differences from underdense theory arise. At $0.1n_c$, the interaction resembles that of seen in the underdense case. As the laser propagates through the plasma, a plasma wave is excited with it.
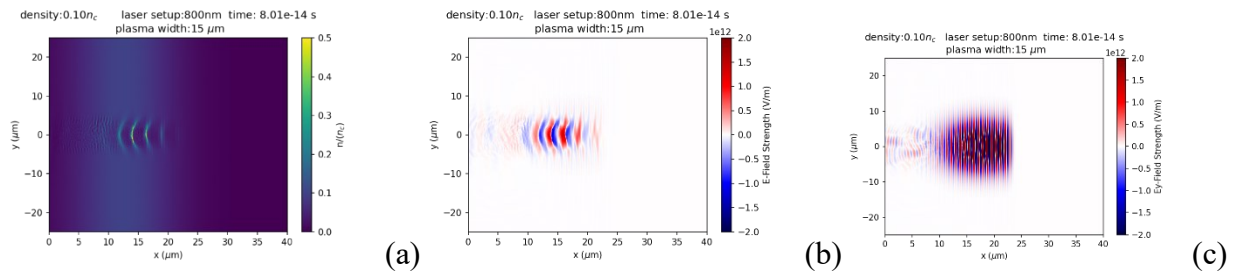
Figure 4.3: (a) Density profile at a snapshot in time where the laser is still present in the plasma. (b) Longitudinal fields, or plasma wave, generated by the laser. (c) Laser field profile.

The plasma wave is shown in Figures 4.3a and 4.3b: Figure 4.3a shows the density gradients forming, while Figure 4.3b shows the longitudinal electric fields resulting from the plasma wave as the laser travels through, as shown in Figure 4.3c. The wave captures electrons within the regions the density gradient regions. Electrons with sufficient energy are accelerated. If the electrons have insufficient energy, such as at the tail end of the velocity distribution, the electrons become trapped within the wave and lead to instability and wave-breaking.
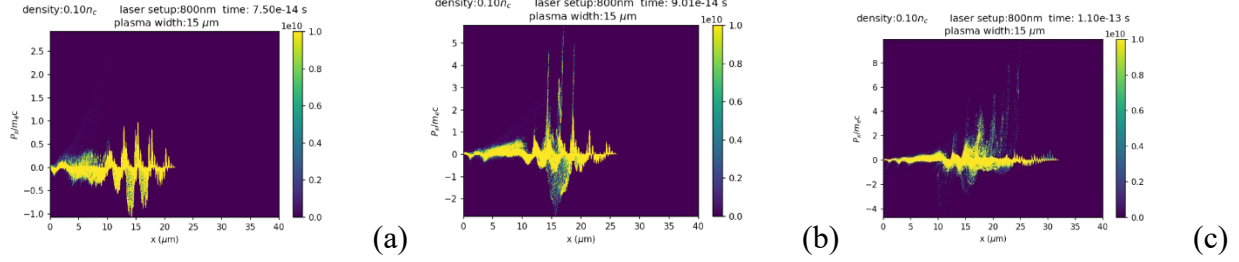
Figure 4.4 (a-c): Phase space evolution of the electrons as the laser passes through the plasma. (a) Initial plasma wave formed from interaction with the laser. (b) Peaks in phase grow until the wave begins to break. (c) The plasma wave fully breaks down which accelerates electrons.

The wave-breaking shown in Figure 4.4c leads to injection of electrons into the remaining accelerating field structures. This injection process leads to visible peaks of varying height in the phase space.

The energy distribution is examined to compare with expected energy values from underdense theory. In Figure 4.5, the energy distribution exhibits wakefield-like behavior as seen through the peak at the tail end of the distribution. The maximum energy measured in this snapshot is found to be 28 MeV, while the peak at the tail corresponds to an energy of ~18 MeV. Based on the energy gain formula of LWFA, equation 2.29, the fields should impart an energy of 18.5 MeV, and it can be assumed that the interaction exhibited here mirrors that predicted by LWFA theory. Additionally, the plasma wavelength can roughly be calculated in the peak region using the formula:

$$\lambda_p = \frac{2\pi c}{\omega_p} \, (4.1)$$

This results in $\lambda_p = 2.6 \ \mu m$, which is a distance resolvable through the setup of the grid and its spacing.

time: 1.15e-13 s
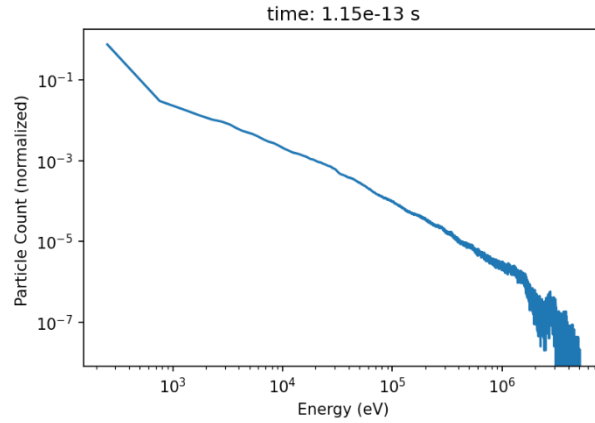
Figure 4.5: Energy distribution of the electron based on true electron count after the onset of

wave-breaking.

density:0.1n_c laser setup:800nm time: 3.00 e-13 s
plasma width:15 μm
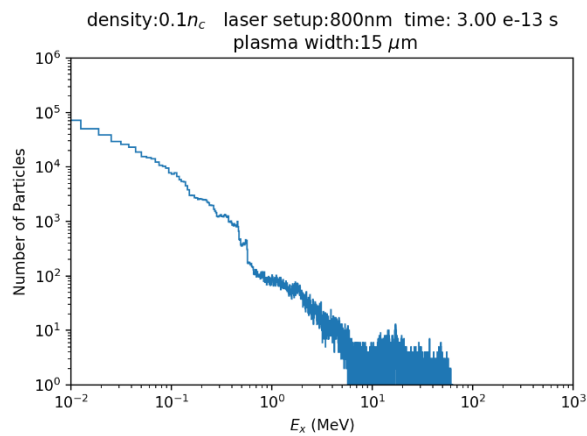
Figure 4.6: Electron macroparticle energy distribution measured by the probe in vacuum. The

distribution is the sum through each time step over 300 fs.

4.2.1b Beat-Wave Interaction

A beat-wave, formed from the beating of the primary and secondary laser, is sent into the

same plasma as in the previous section and exhibits similar behavior.

(a)   (b)
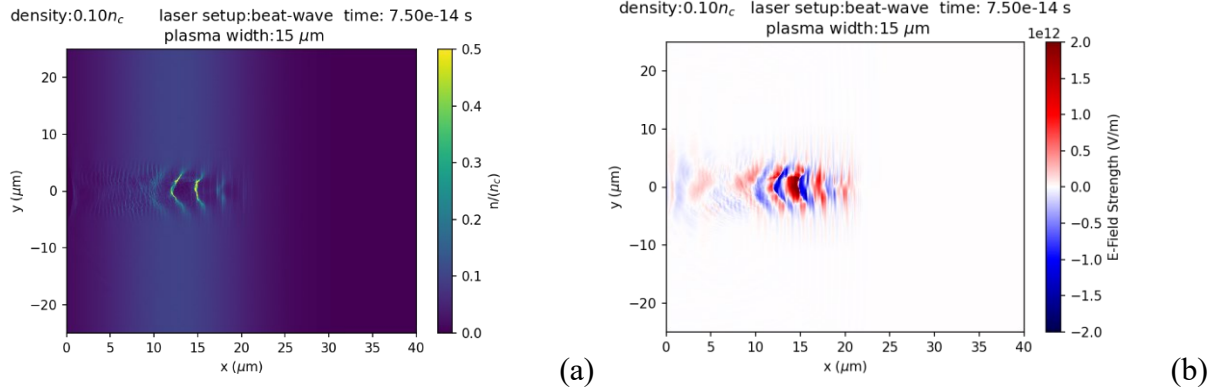
Figure 4.7: (a) Density profile of the plasma in the beat-wave, $0.1n_c$ case when the wave is generated. (b) Longitudinal field profile showing the plasma wave and its resultant accelerating fields.

The wave rapidly reaches the wave-breaking limit, causing injection of electrons into the accelerating fields. In the phase space shown in Figure 4.8 are two clear peaks formed which propagate transversely. Additionally, the peaks are taller and indicate a greater gain of energy.
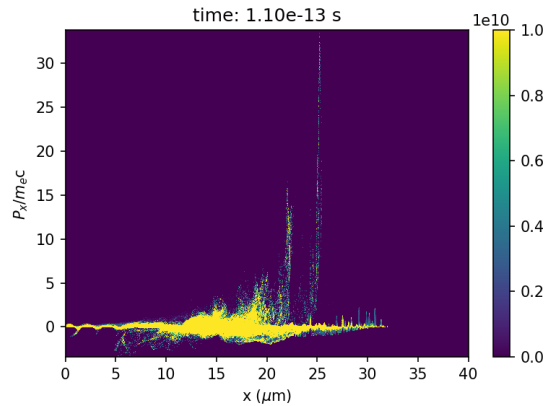
Figure 4.8: Phase space of electrons in the beat-wave, $0.1n_c$ case after wave-breaking.

The expected energy gain from this interaction is calculated to be ~47 MeV through alteration of the use of an effective a_0 taken for the beat-wave. The maximum energy in the distribution after wave-breaking is found to be ~80 MeV, with the peak at the tail corresponding

to an energy of ~50 MeV. The energy at the peak corresponds well to LWFA theory as in the single-laser case, showing that LWFA continues as the primary acceleration mechanism.
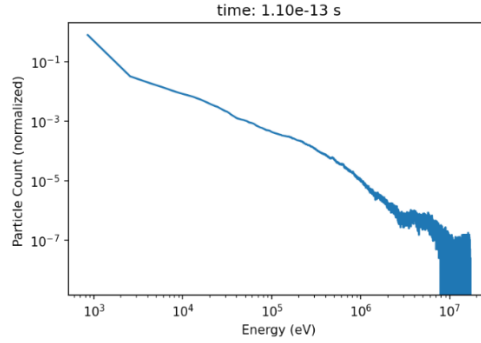
Figure 4.9: Energy distribution in the beat-wave, $0.1 n_c$ case after wave-breaking occurs.
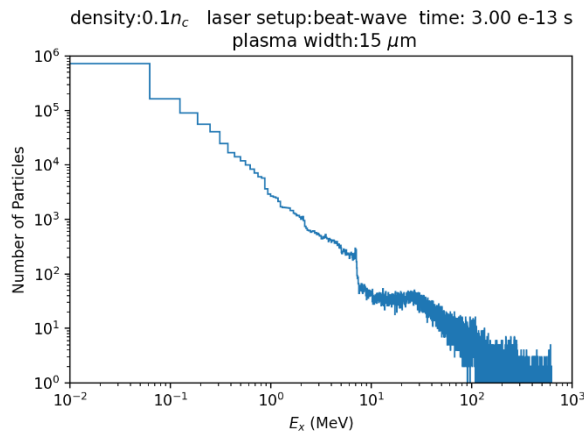
Figure 4.10: Longitudinal electron macroparticle energies measured by the probe in the beat-wave, $0.1 n_c$ case.

The divergence of the electron beam is examined using the characteristics measured by the probe in vacuum and displayed in Figure 4.11. The electrons are primarily diffracted at angles of $\pm 10°$, but the electrons of interest measured in both energy distributions have less divergence.
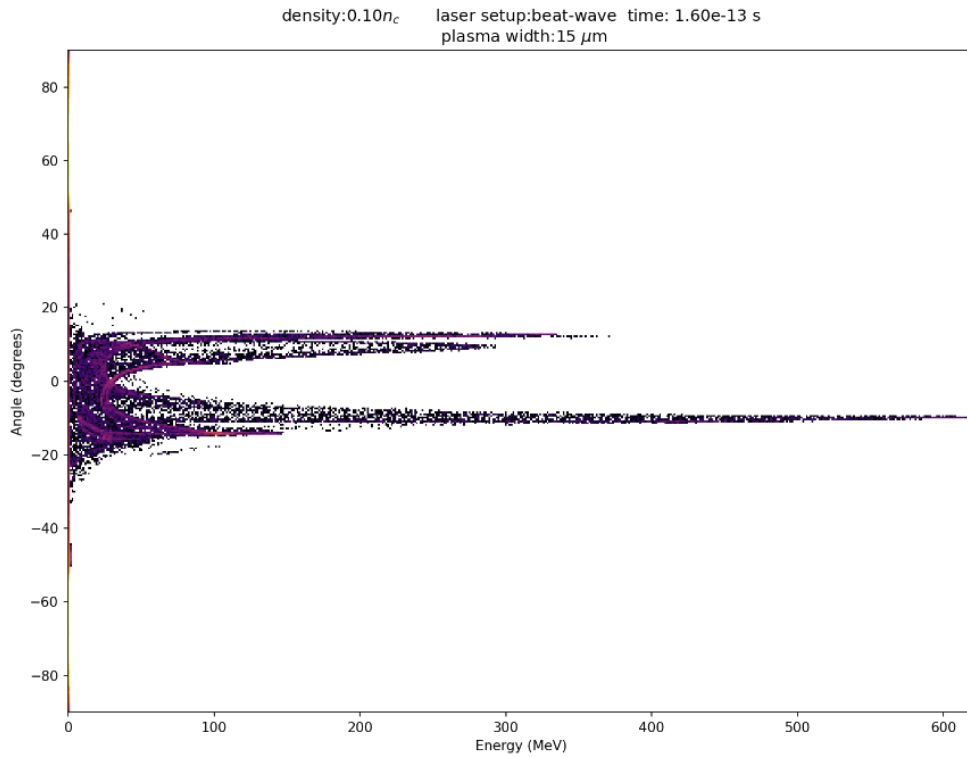
Figure 4.11: Divergence of electrons as a function of their energy in the beat-wave, $0.1n_c$ case.

A comparison of the performance of a single laser to a beat-wave setup shows a greater maximum and peak energy in the beat-wave setup. The charge of electrons measured by the probe in the tail-end of the distribution are similar, but the overall charge of electrons is greater in the beat-wave case. This is of great importance, especially when considering the greater charge occurs in the range of 1-10 MeV.
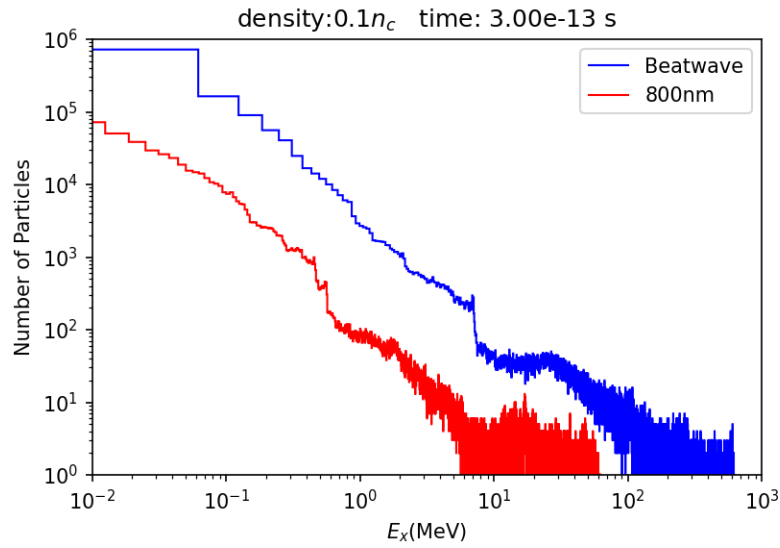
Figure 4.12: Combined plot of electron macroparticle distributions measured by the probes in the single laser and beat-wave case for a density of $0.1n_c$.

4.2.2 Quarter-Critical Density Case

As expressed in 2.4.1, the Raman Scattering instability requires a density $n \leq \frac{n_c}{4}$. To examine the effect of reaching this limit, the peak density in the following simulations is set to $n = 0.25n_c$.

4.2.2a Single Laser Case

In the case of solely the primary laser interacting with the plasma, the density profile already shows a difference in behavior compared to the $n = 0.1n_c$ case. As the laser approaches the peak of the density distribution, a plasma wave is temporarily formed.
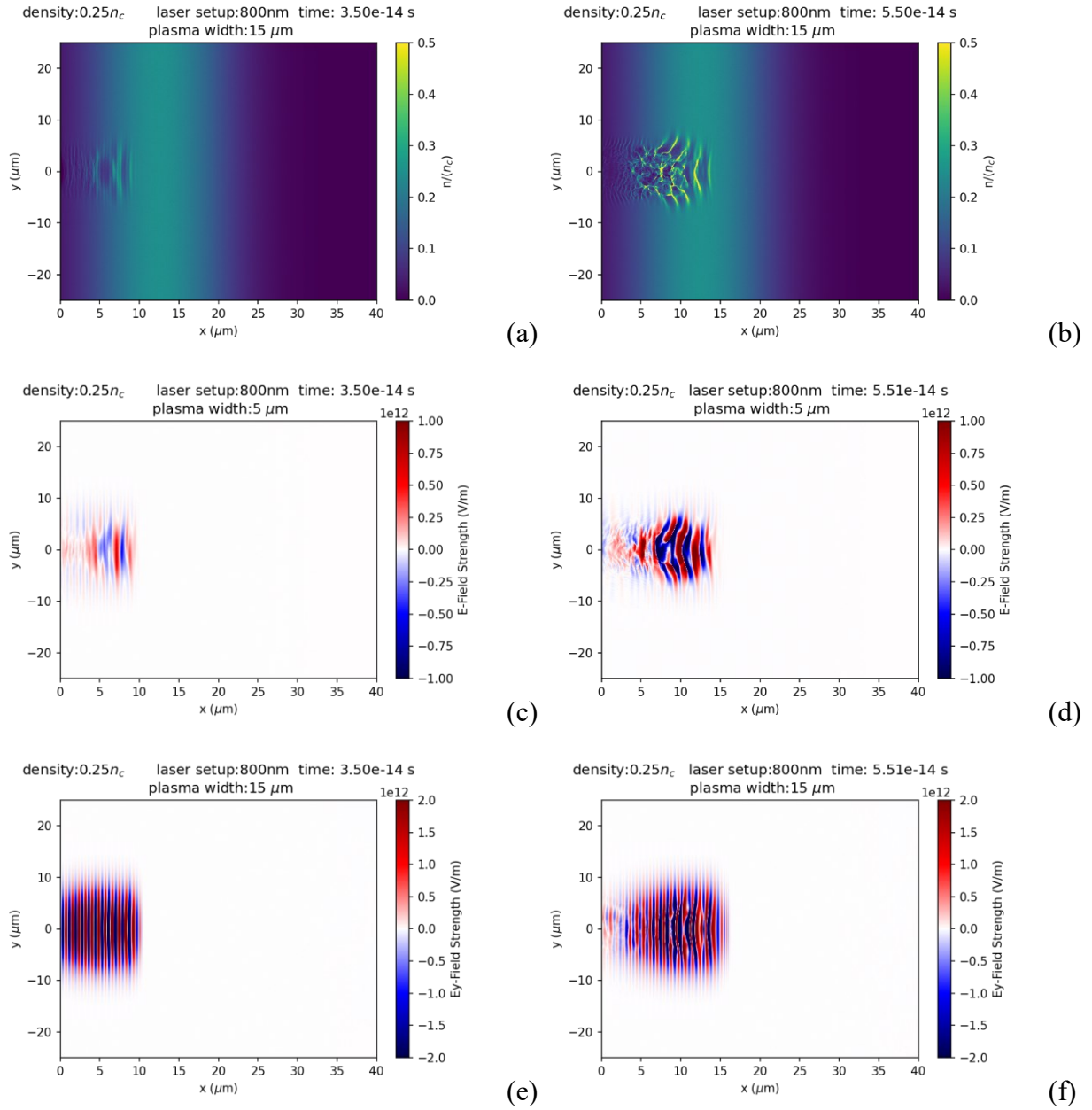
Figure 4.13: (a-b) Density profile of the $0.25n_c$ peak interacting with the primary laser. (c-d) Longitudinal fields representing the fast formation and break-down of the plasma waves. (e-f) Laser profile passing through the plasma.

The wave breaks down faster, where wave-breaking is visible at 55 fs compared to the 90 fs breakdown in the lower density case. The wave-breaking effect is also shown through

examination of the energy distributions in Figure 4.14. Aside from initial interaction between the laser and plasma which causes a transient wave, the tail-end of the distribution does not have a peak. Instead, the overall energy of the plasma increases, showing heating of the plasma resulting from the laser coupling to the bulk of the plasma, while the maximum energy is ~10 MeV.
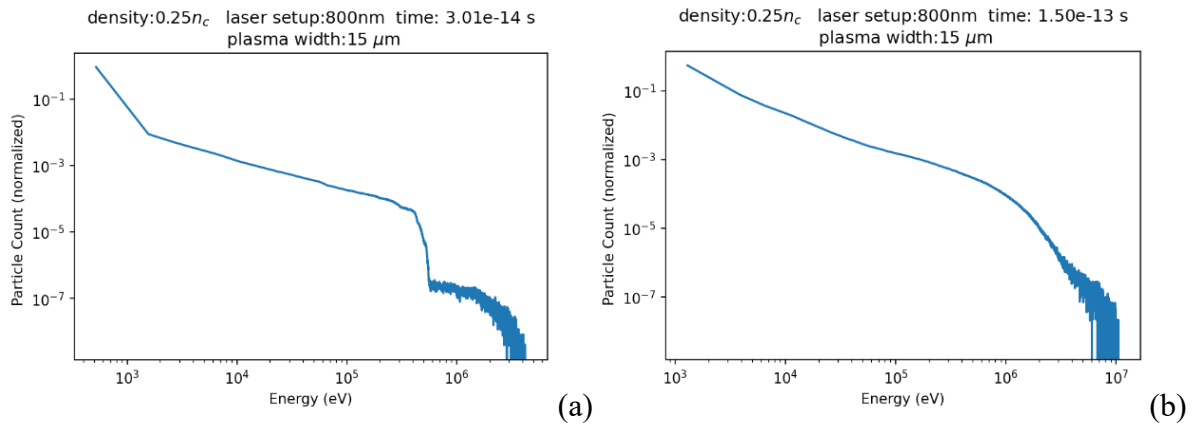
Figure 4.14: Electron energy distributions at $0.25n_c$ interacting with a single laser when (a) the laser first interacts with the plasma and (b) after the laser leaves the plasma.

The electron distribution generated through the probe measurement shows a peak of electrons measured at 0.3 MeV, thereby indicating a potential resonant interaction exciting 0.1 MeV order electrons. This is a shift from the $n = 0.1n_c$ case, where the peak is found in the distribution tail rather than the body. Additionally, the higher energy electrons from this interaction are shown to have a similar divergence angle to that in the lower density case in Figure 4.16.
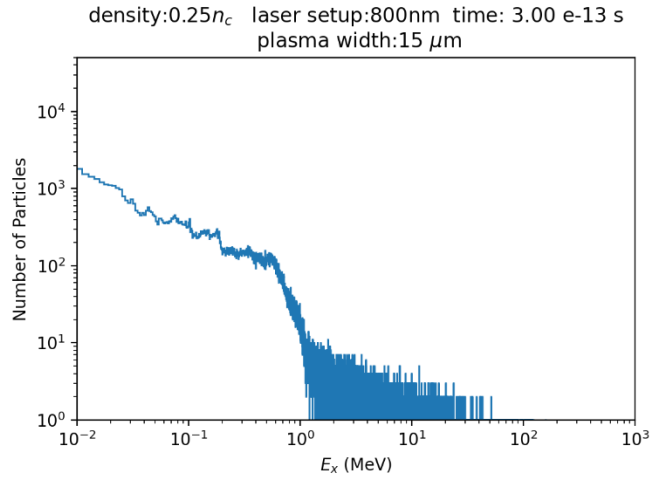
Figure 4.15: Electron macroparticle distribution measured by the probe in the $0.25n_c$, single laser case.
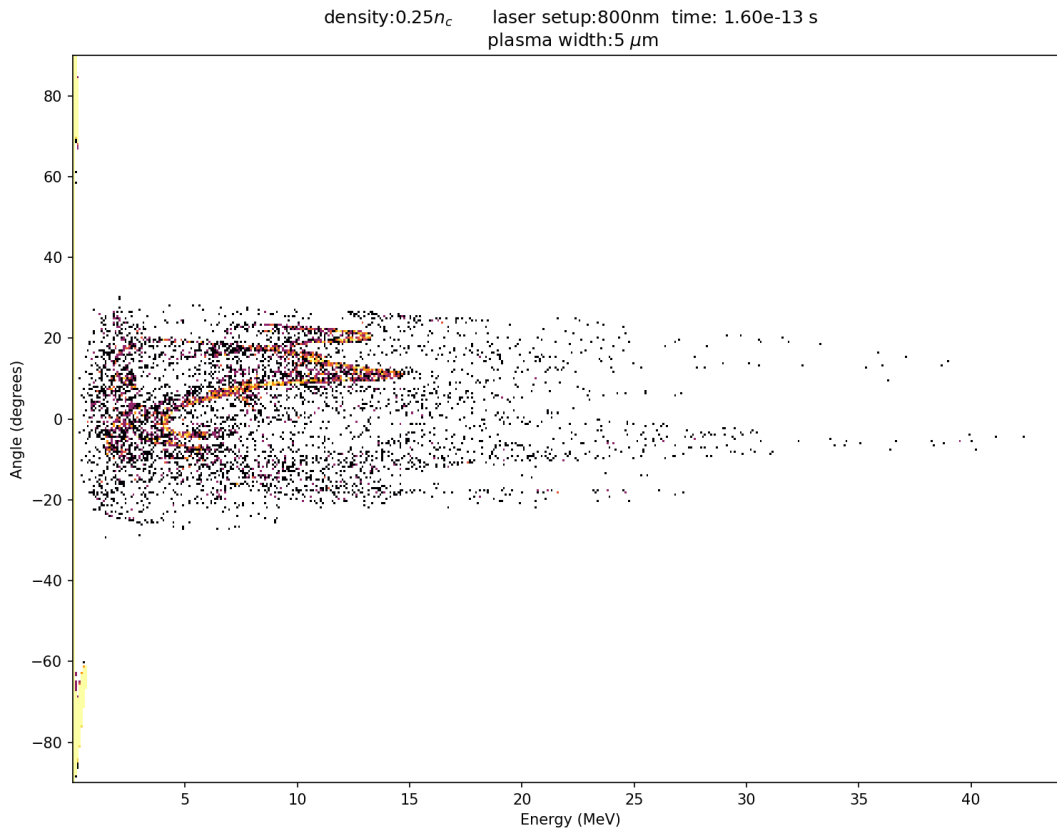
Figure 4.16: Divergence of electrons as a function of their energy in the $0.25n_c$, single laser case.

4.2.2b Beat-wave Case

The beat-wave setup once again shows similar interactions between the laser and plasma as those in the single laser case. The beat-wave excites a plasma wave in the lower-density regions of the density gradient which breaks down upon entering the higher-density region.

(a)

(b)

(c)

(d)

(e)

(f)
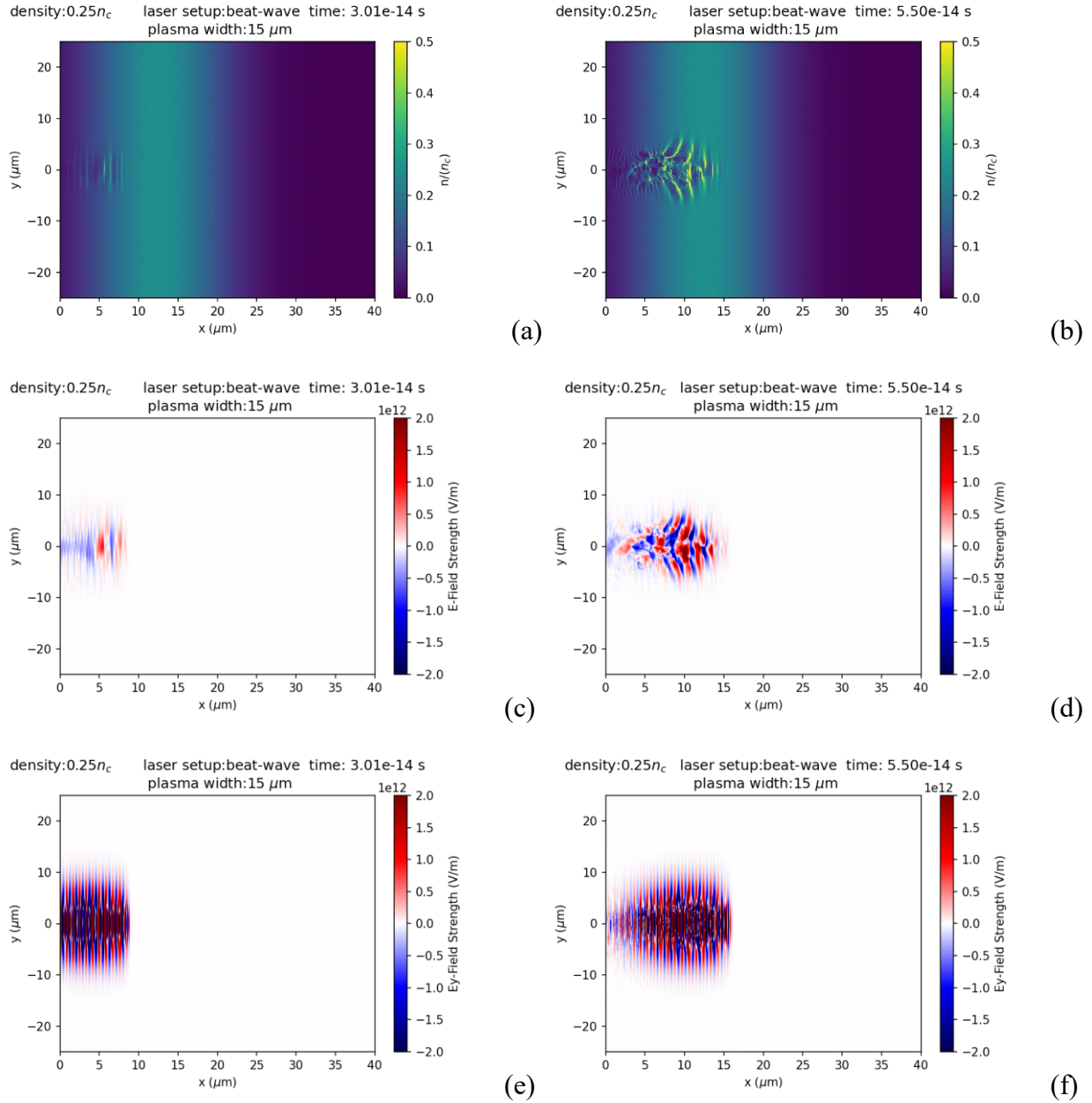
Figure 4.17: (a-b) Density profile of the $0.25n_c$ peak interacting with the laser beat-wave.

(c-d) Longitudinal fields representing the fast formation and break-down of the plasma waves.

(e-f) Laser profile passing through the plasma.

The turbulent interaction between the beat-wave and the plasma can also be seen through the phase space. The wave-breaking injects bulk electrons into accelerating field structures. The more turbulent acceleration thus leads to more electrons accelerated to lower energies, with several peaks visible in the phase space compared to the two peaks visible in the $0.1n_c$ case.

(a)

(b)
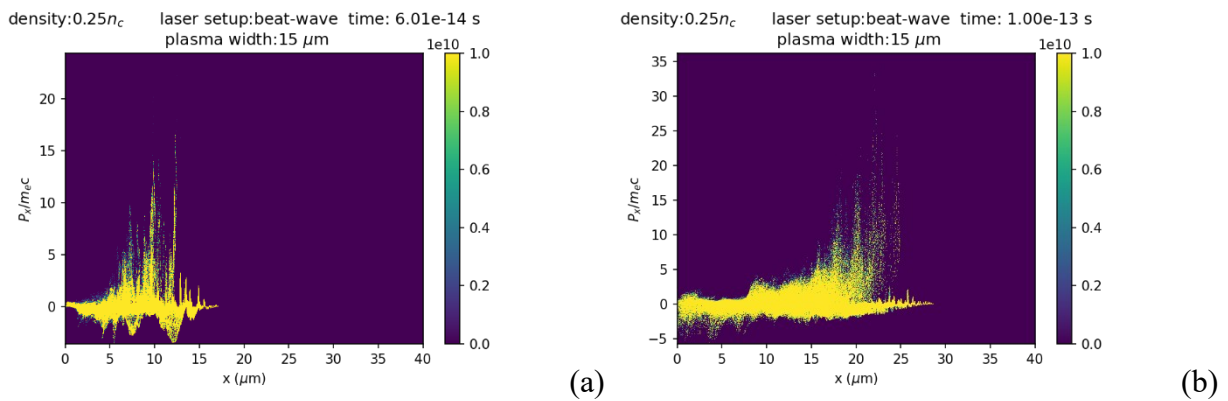
Figure 4.18: (a) Phase space of the $0.25n_c$ plasma interacting with the beat-wave when wave-breaking occurs. (b) Phase space as laser propagates through.
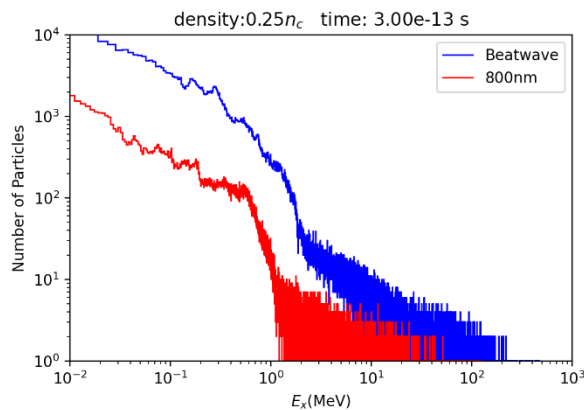
Figure 4.19: Comparison of the time-integrated electron macroparticle distributions measured by the probe at $0.25n_c$ between the beat-wave and single laser case.

When comparing the two probe distributions in Figure 4.19, the overall trend of the distributions is the same in both cases. The beat-wave, however, leads to a higher maximum energy in addition to a slightly higher overall charge up to ~20 MeV. It is also noted that, once again, peak visible at the distribution tail for $0.1n_c$ is no longer visible in the distribution for $0.25n_c$.

The longitudinal fields eventually evolve to form a sheath along the exit of the plasma, as shown in Figure 4.20. The sheath forms towards the end of the simulation where the laser has already fully left the plasma, and the waves formed within the plasma have all broken down. The effect of the sheath is found through an examination of the probe measurements. Figure 4.22 shows electrons continue to accelerate to 1 MeV order energies in the time after the sheath is formed. The sheath acts as both an accelerating structure and a barrier for incident electrons. If the electrons possess sufficient energy, they can overcome the barrier of the negatively polarized portion of the sheath and move into an accelerating region. The electrons then once again experience deceleration after a duration in the positively polarized region. If the electrons cannot escape from the pull of the positive field, they return to the plasma and oscillate about the sheath
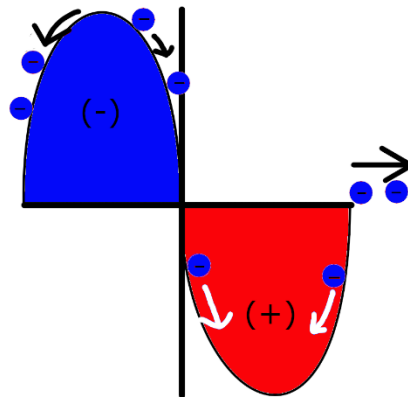
Figure 4.20: Illustration of electrons moving through the region positive (red) and negative (blue) regions of the sheath.
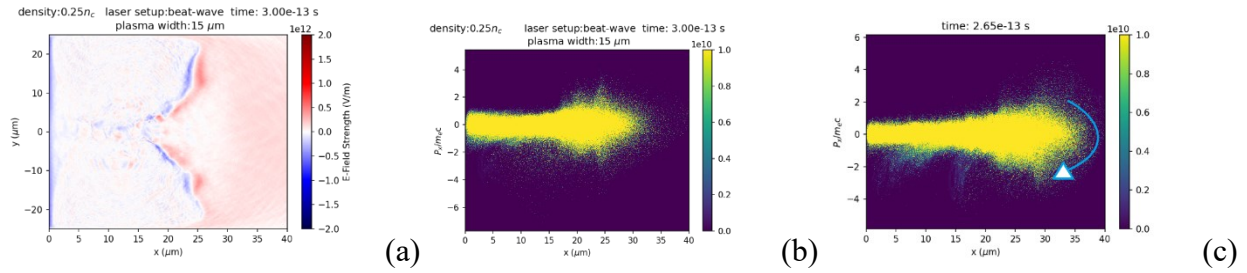
Figure 4.21: (a) Sheath formed at the edge of the plasma at the end of the simulation for $n = 0.5n_c$. (b) Electron phase space at the same moment in time. (c) Arrow shows the trapping of electrons by the sheath causing a vortex in the phase space.

The perpetual oscillation is seen in an analysis of the phase space plot, Figure 4.21b. The sheath is most prominent at $x = 20\mu m$ and $25\mu m$. When examining the same regions in the phase space, we see negative and positive peaks. These are electrons which are being accelerated or decelerated by the sheath fields. If they have sufficient energy after interacting with the sheath, they escape the plasma. However, electrons with insufficient energy follow an orbit in the phase space illustrated in Figure 421, corresponding to the oscillation of electrons about the sheath. Sheaths are not unique to the quarter-critical density case and are still visible in the lower density cases. However, the strength of the sheath from the lower density interactions prevents acceleration to the 1 MeV order as in the quarter-critical case.

density:0.25n_c laser setup:beat-wave time: 2.90e-13 s
plasma width:15 μm
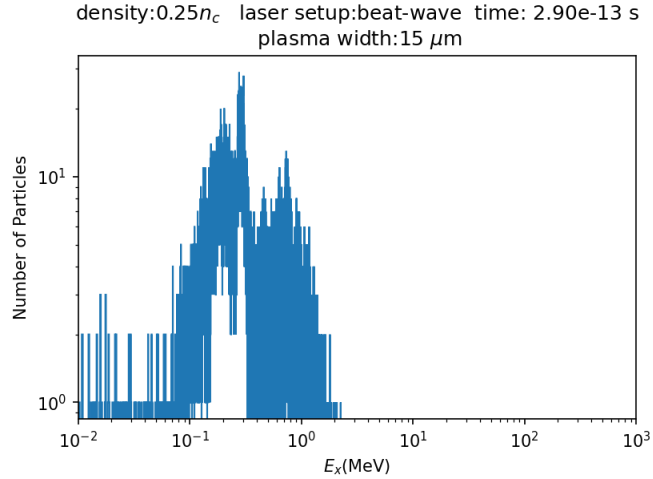
Figure 4.22: Electron macroparticle measurement towards the end of the simulation of the quarter-critical density beat-wave interaction.

In figure 4.19, the density is seen to form a large pair of cavities about the laser axis at $x = 7.5\mu m$, and a channel structure forms along the plasma. The cavities form at $0.25n_c$ but not $0.1n_c$, and the effect of this cavity generation can be seen in Figure 4.23.
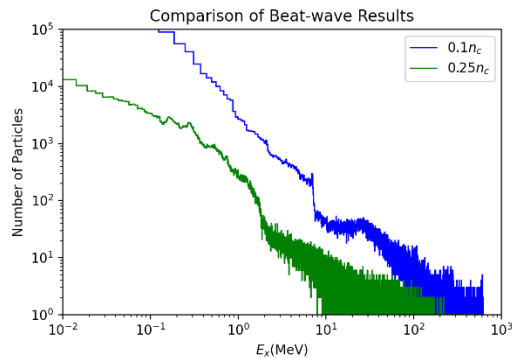
Figure 4.23: Comparison of macroparticle electron distributions measured by the probe for 0.1nc and 0.25nc

The distribution for $0.1n_c$ shows the peak at the tail-end characteristic of wakefield acceleration. However, the $0.25n_c$ distribution does not show this peak forming. As such, the cavities can be determined to not play a role in generation of high-energy electrons. However, a steepened profile occurs

40

at ~1 MeV for $0.25n_c$, showing the increased MeV order generation which occurs in the presence of the fields generated by the cavities.

When examining the divergence of the resulting electron beam, the high-energy electron products are found to have the same divergence as in the previous cases. However, a sizable measurement by the probe is found after the sheaths have formed corresponding to single MeV order electrons accelerated with negligible divergence.
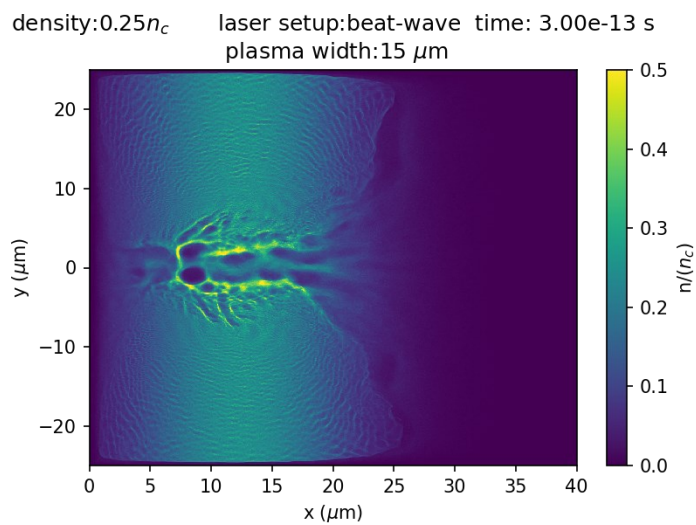
Figure 4.24: Density profile at the end of the simulation for a beat-wave interacting with $n = 0.25n_c$.
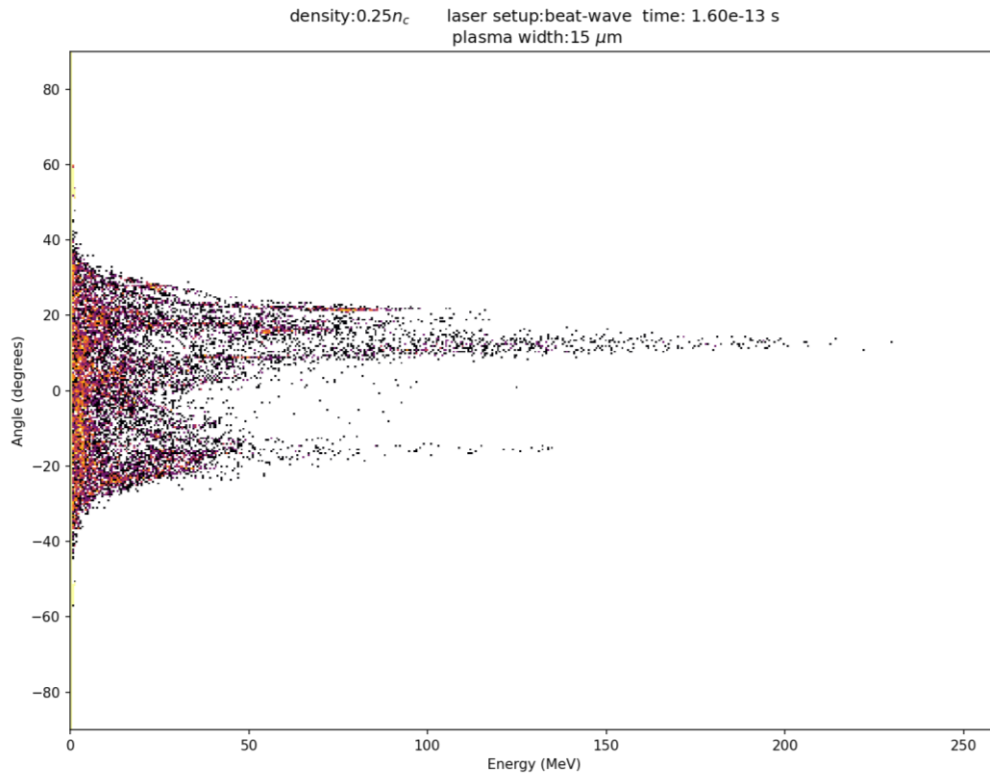
Figure 4.25: Divergence measured by the probe as a function of energy for $n = 0.25n_c$ interacting with the beat-wave for the moment in time when the laser exits the plasma.

density:0.25n_c laser setup:beat-wave time: 2.60e-13 s
plasma width:15 μm
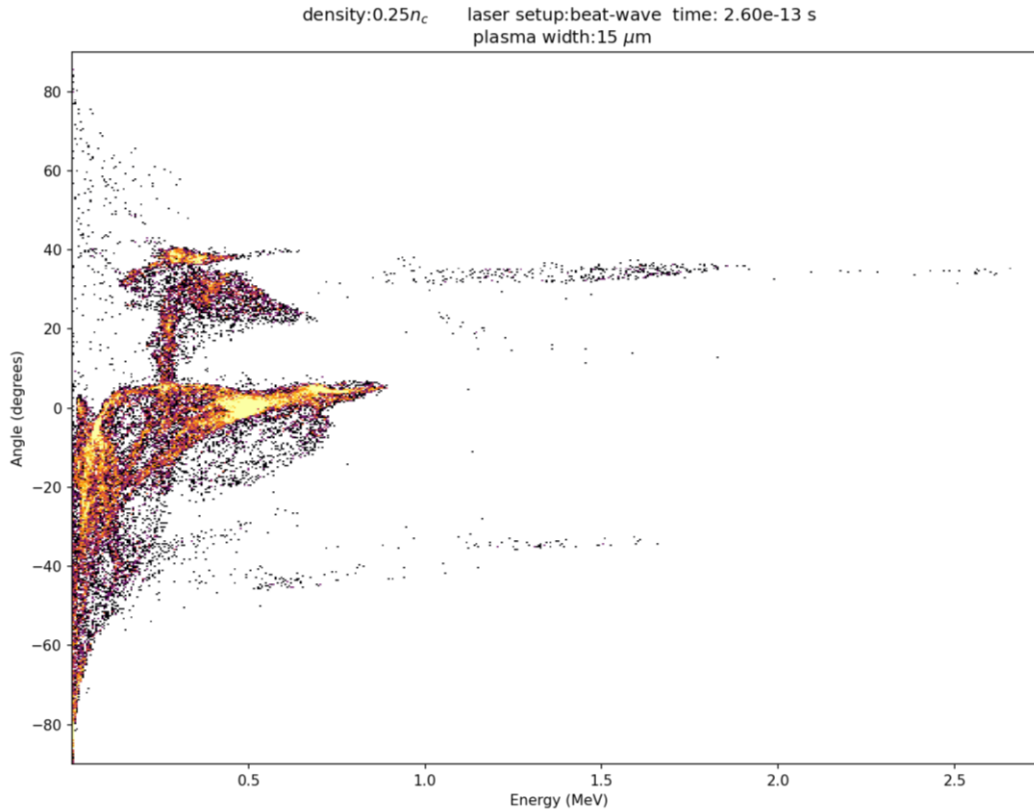
Figure 4.26: Divergence measured by the probe as a function of energy for $n = 0.25n_c$ interacting with the beat-wave for the time where the sheath fields are the dominating structures in the plasma.

4.2.3 Half-Critical Density Case

The quarter-critical density results seem to support a shift in acceleration mechanism from theory predicted from underdense interactions. To examine this shift further, the peak is increased to half the critical density of the plasma, $0.5n_c$. The behavior of this interaction moves even further from that predicted by underdense theory and begins showcasing the most distinct advantage in using a beat-wave rather than a single laser.

4.2.3a Single Laser Case

The density profile in the interaction of the primary laser with the half-critical plasma shows faster break-down of the plasma wave generated by the laser. Due to the higher density, the plasma wave breaks down closer to the initial interaction region. The faster wave-breaking subsequently causes an earlier injection of electrons.

(a)　(b)
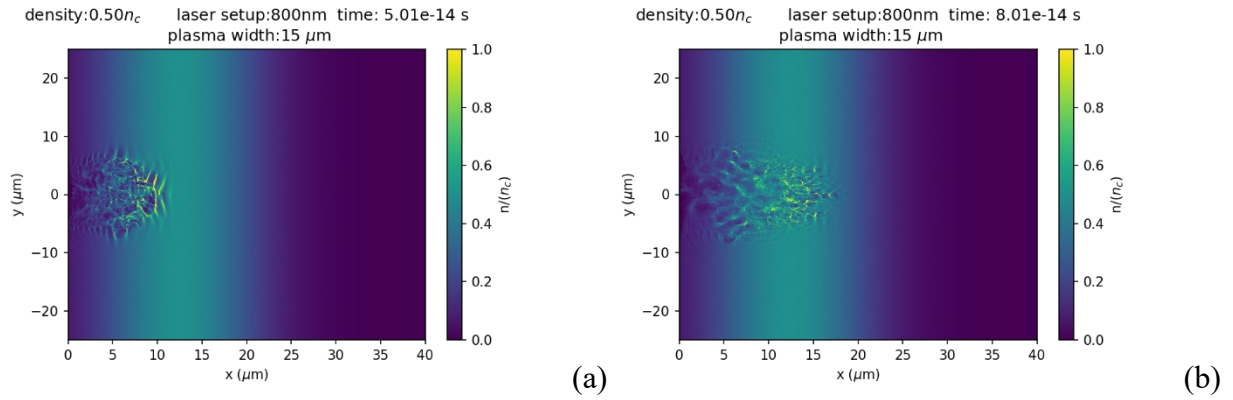
Figure 4.27: (a) Slightly visible plasma wave in the density profile for $n = 0.5n_c$ interacting with the primary laser. (b) Wave-breaking of plasma wave leads to ripples in the density profile.

The interaction results in electrons accelerating to lower energies, compared to the lower densities, with a greater charge.
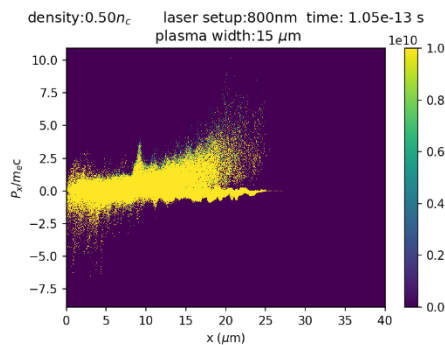
Figure 4.28: Electron phase space snapshot as the laser propagates through the half-critical plasma.

The energy distribution of the interaction shows an initial peak as the laser propagates and first interacts with the plasma. However, the distribution rapidly flattens and leads to a smooth curve with a maximum measured energy of ~2 MeV, corresponding to electrons trapped within the sheath.
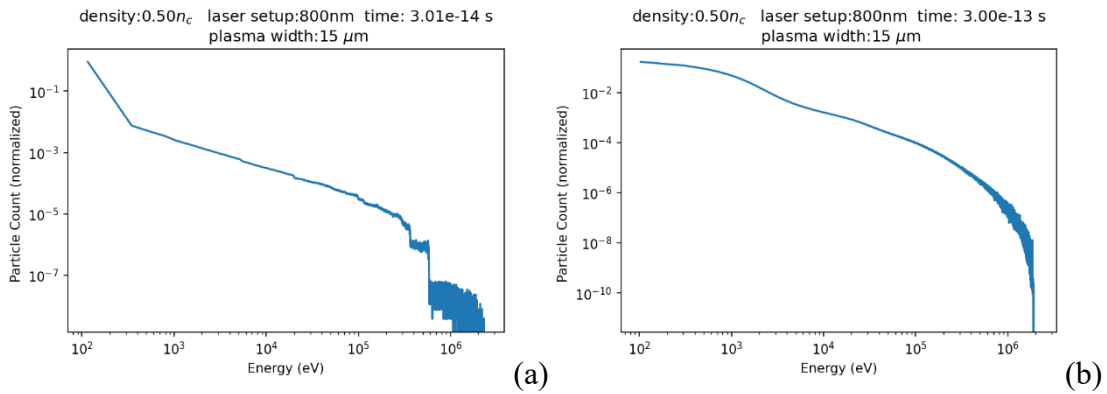
Figure 4.29: (a) Initial electron distribution as the laser first enters the half-critical plasma. (b) Electron distribution at the end of the simulation for the half-critical plasma.

Figure 4.30 shows no peak resulting from interaction with the half-critical plasma. The acceleration of 1 MeV order electrons continually accelerated out of the plasma through the pairing of the sheath and channel structures, as seen in the quarter-critical cases, is no longer found.
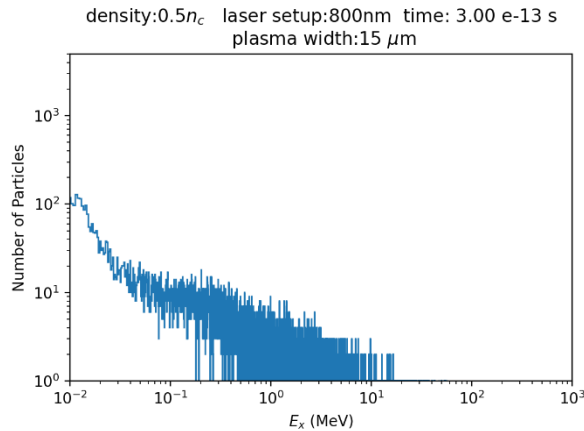
Figure 4.30: Time integrated electron macroparticle distribution of particles measured passing through the plane of the probe.

This deviation in behavior from the quarter-critical single laser interaction can be attributed to the different end behavior shown in the density profile. The half-critical density profile shown in Figure 4.31b shows a more focused channel than the quarter-critical case in Figure 4.31a. However, the quarter-critical profile shows large cavities forming at the center and edge of the plasma, such as those in the beat-wave case. The half-critical profile shows more numerous cavity development that is restricted to the beginning half of the plasma. The cavities do not extend to the exit of the plasma where sheath fields may lie, meaning the electrons are not accelerated to the same energies.
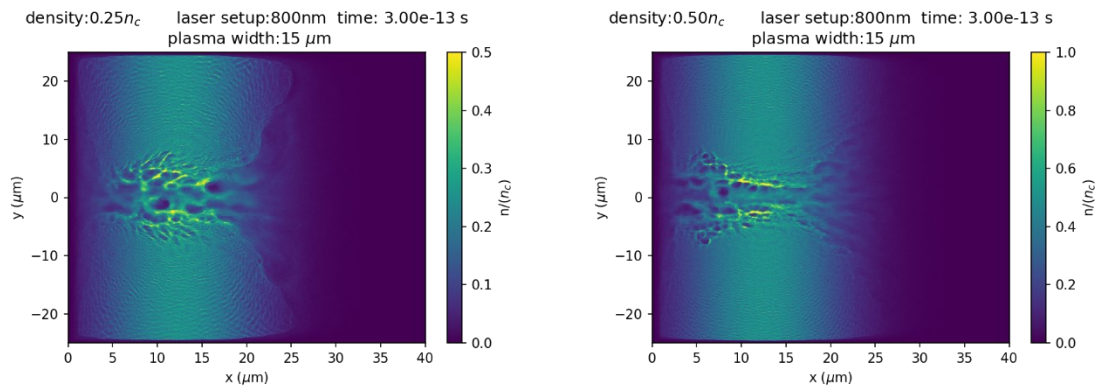
Figure 4.31: (a) Density profile at the end of the simulation for the $n = 0.25n_c$ interacting with a single laser. (b) Density profile at the end of the simulation for the $n = 0.5n_c$ interacting with a single laser.

4.2.3b Beat-wave Case

The beat-wave case once again shows a similar initial interaction to that of the single pulse, where the beat excites a plasma wave which breaks down as the laser approaches the higher density regions of the plasma.

(a)   (b)
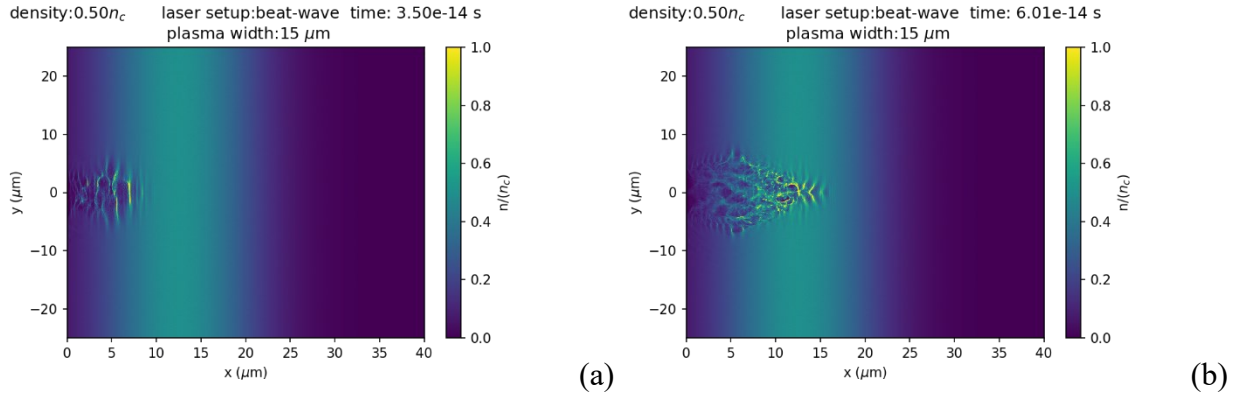
Figure 4.32: (a) Density profile as the laser first enters the half-critical plasma. (b) Density profile as the plasma waves break.

The time-integrated energy distribution of the probe shows many electrons accelerated in the range of 1-3 MeV. This number of electrons were not obtained in the single-laser case.
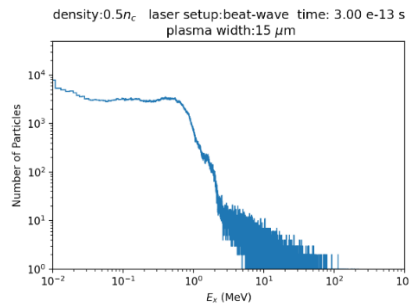
Figure 4.33: Time-integrated energy distribution of electron macroparticles passing through the plane of the probe for the beat-wave at $n = 0.5n_c$.

As initially stated in the previous section, the generation of these 1 MeV order electrons seem to correspond to the presence of a channel and cavity structures throughout the plasma density. The density profile at the end of the simulation for the beat-wave shows prominent cavity generation throughout the entire plasma, as shown in Figure 4.33a.
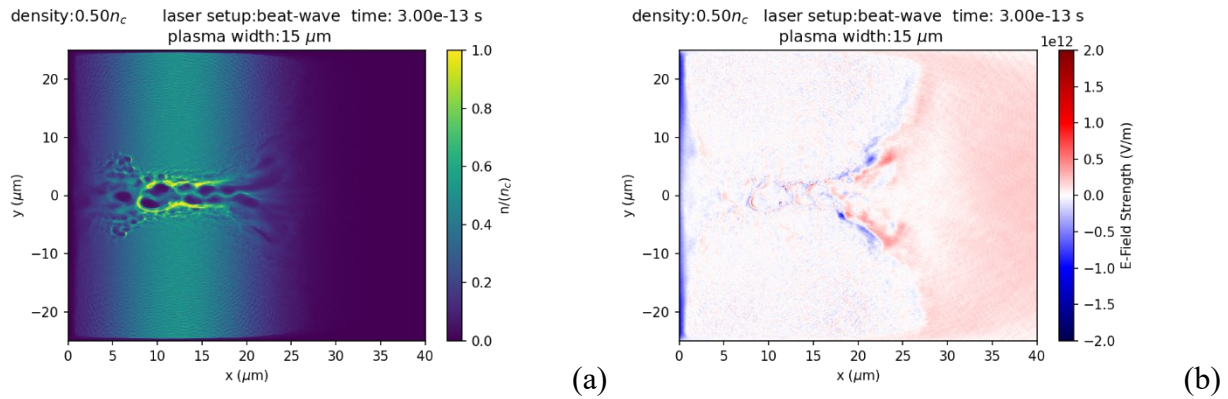
Figure 4.34: (a) Density profile of the half-critical plasma at the end of the simulation after the pulse has left. (b) Longitudinal field profile at the end of the simulation.

Figure 4.34b shows the effect these cavities have as prominent longitudinal fields propelling electrons from within the plasma towards the exit where the sheath structure lies. It is noted that the sheath structure no longer runs along the entire exit edge of the plasma, but it is instead focused about the region the laser has propagated through. Examination of a snapshot of the probe measured electron distribution shows continual generation of single MeV order electrons as the cavities and sheath remain the only structures within the plasma, such as the distribution shown in Figure 4.35. Consequently, the beat-wave interaction leads to an increase in charge for single MeV order electrons despite the same total laser energy. The presence of the secondary laser enhances the characteristics of the accelerated electrons which may be a factor of the secondary laser generating a separate mode in the plasma at the same time as the primary laser.
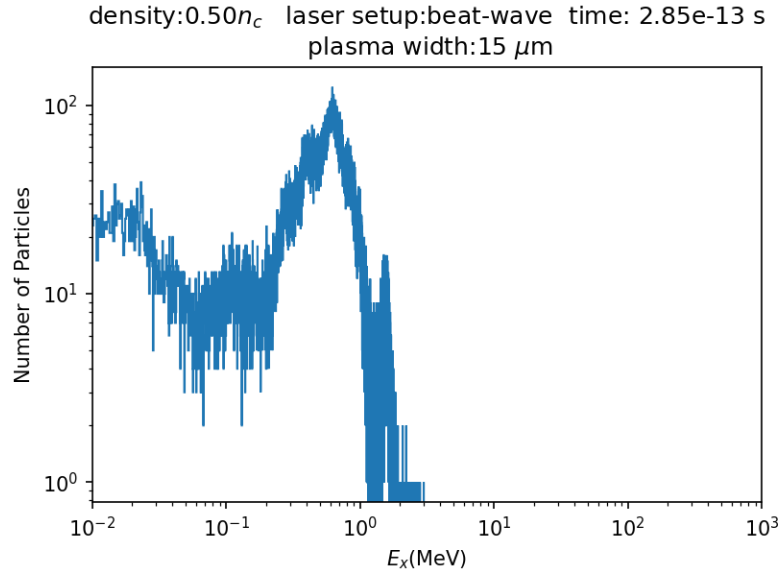
Figure 4.35: Electron macroparticle distribution measured by the probe towards the end of the simulation of the half-critical density plasma interacting with the beat-wave.
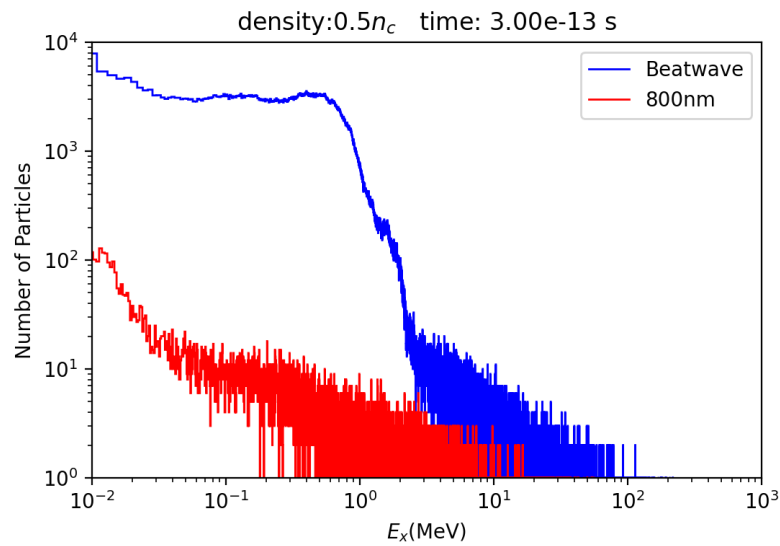
Figure 4.36: Comparison of the single laser and beat-wave interaction for $n = 0.5n_c$ shown through the probe-measured macroparticle distribution.

The continued effect of the cavities is also seen in the comparison of the beat-wave results for $0.25n_c$ and $0.5n_c$. The peak of MeV order electrons first observed at $0.25n_c$ is enhanced as the

density increases to $0.5n_c$. This enhanced peak corresponds to the greater number of cavities generated throughout the density profile of the plasma, as well as the shrunken sheath region compared to the lower simulated densities.
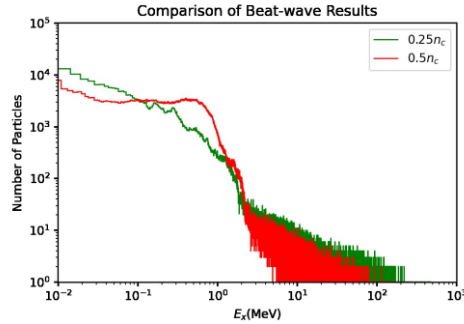
Figure 4.37: Comparison of macroparticle electron distributions measured by the probe for 0.25nc and 0.5nc

4.2.4 Near-Critical Density Case

The final density examined in this work is the density closest to the critical, where $n = 0.9n_c$. This density is chosen as the density closest to the critical density to have the beat frequency close to the plasma frequency. With such a condition, the beat frequency can more easily resonate with the plasma. With the increased plasma density and better coupling to the plasma, a higher charge electron beam is expected and desired from this interaction. As the density increases, a downward trend in sheath field strength at the exit edge of the plasma is observed. Simultaneously, there is improved generation of cavity and channel structures throughout the plasma in the beat-wave interaction. The beat-wave shows an advantage over the single laser interaction once again in this NCD plasma case, where cavity structures are generated completely through the plasma using a beat-wave but not with a single laser.

4.2.4a Single Laser Case

The single laser interaction with a density of $0.9n_c$ amplifies the behavior seen in

interactions moving past $\frac{n_c}{4}$. The plasma density profile in Figure 4.36a shows the initial response

of the plasma to the laser. The small wavenumber plasma wave formed reaches the wave-

breaking limit as soon as the laser pulse moves slightly into the near-critical plasma. The break-

down of the waves leads to the initial formation of cavities shown in Figures 4.34a and 4.34b.

The cavities do not form throughout the plasma and instead stop once they reach the center of the

density profile at $x = 12.5\ \mu m$. Beyond the centerline of the plasma density, the laser produces

ripples, through the ponderomotive force, which propagate through the plasma. By the end of the

simulation, standing cavity structures are visible in the initial half of the plasma.

As expected in a higher-density interaction, the electron distribution, Figure 4.37, shows

that there is no acceleration of the relativistic electrons in the plasma. Instead, there is a coupling

of the laser to the bulk of the plasma. The distribution from the moderate (quarter and half)

densities to NCD in the single laser case all show similar behavior of electrons as a smooth

distribution with a maximum of 2 MeV within the plasma.
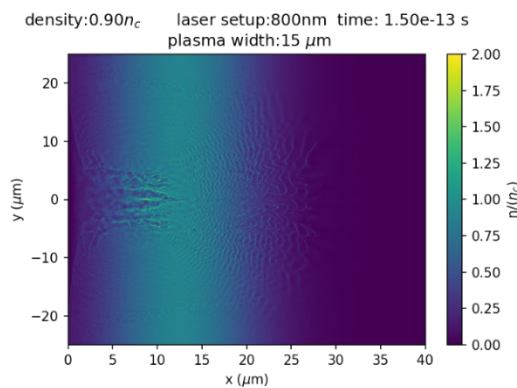
(a)
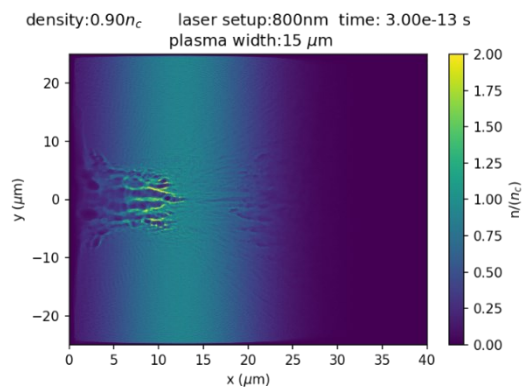
(a)

Figure 4.38: (a) Snapshot when the laser reaches the edge of the plasma showing cavity formation. (b) Standing cavity structures present in the density profile at the end of the simulation.

density:$0.90n_c$ laser setup:800nm time: 3.00e-13 s
plasma width:15 μm
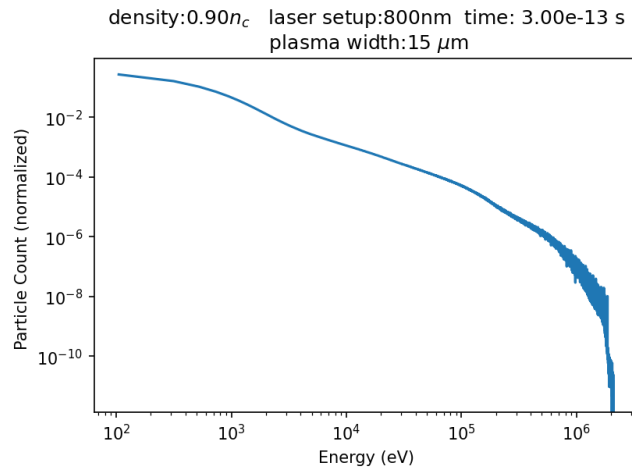
Figure 4.39: Electron energy distribution snapshot at the end of the simulation for the single laser interacting with $n = 0.9n_c$.

As in the half-critical case, the NCD plasma of $n = 0.9n_c$ does not show selective acceleration of single MeV order electrons found in the quarter-critical case, as shown in Figure 4.38. Once again, the distinguishing factor between this case and the quarter-critical, single laser case is the lack of cavity structures throughout the plasma.

density:0.9n_c laser setup:800nm time: 3.00 e-13 s
plasma width:15 μm
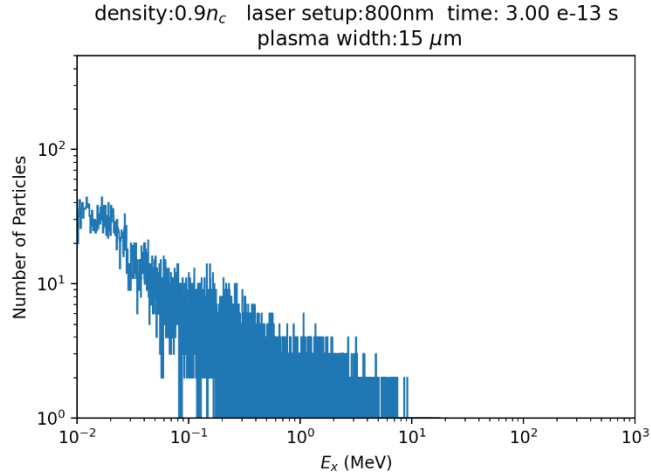
Figure 4.40: Time-integrated energy distribution of electron macroparticles passing through the plane of the probe for the single laser at $n = 0.9n_c$.

4.2.4b Beat-wave Case

The density profiles of the beat-wave interacting with the NCD are shown in Figure 4.41(a-c). Similarly to the half-critical case, the beat-wave couples to the plasma beyond the center of the distribution to create cavity structures throughout the length of the plasma. With these cavities, a peak forms in the energy range of 1-3 MeV in the time-integrated distribution of particles measured by the probe (Figure 4.43). Compared to the previous cases of the beat-wave, the peak of single MeV order electrons is the main characteristic of this distribution. This differs from the half-critical case, for example, in that there are fewer electrons accelerated to energies of less than 1 MeV.

Another behavioral change in this interaction can be seen in the longitudinal electric field profile shown in Figure 4.40. For this iteration of plasma density, there is no longer a polarized sheath field formed at the exit edge of the plasma which is visible in all previous cases. The removal of this sheath leads to electrons selectively accelerating to the MeV order solely through

the cavity fields which are now more pronounced and visible in the longitudinal electric field profile.

(a)

(c)
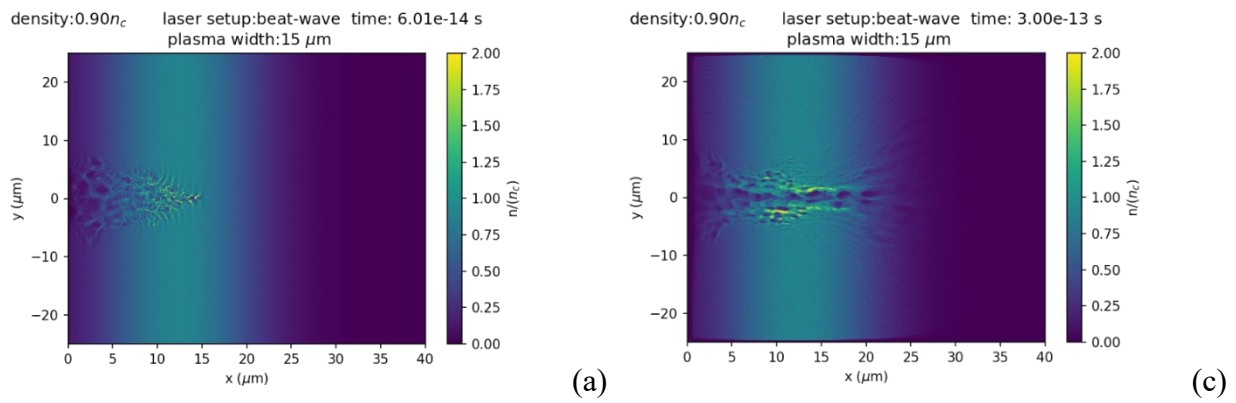
Figure 4.41: (a) Early time snapshot of the density profile from the interaction of the beat-wave with a plasma with peak density $n = 0.9n_c$. (b) Density profile at the end of the simulation.
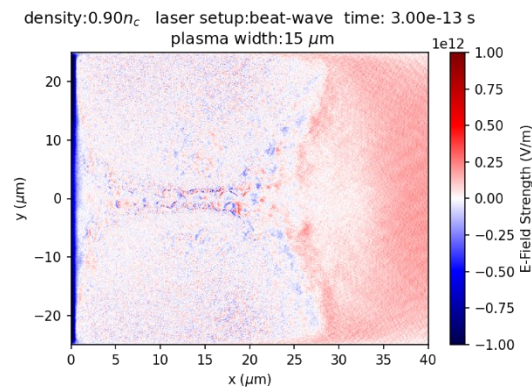
Figure 4.42: Longitudinal electric fields present in the plasma at the end of the simulation.
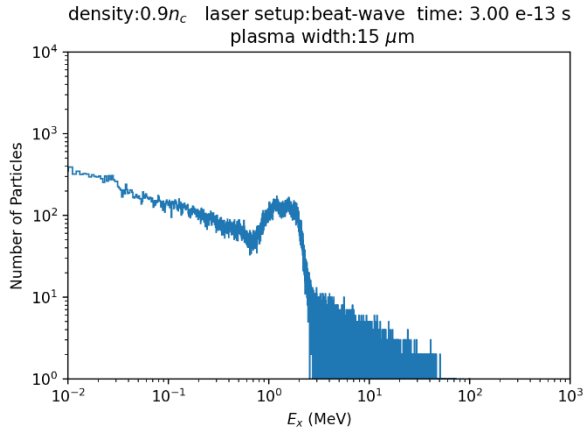
Figure 4.43: Time-integrated electron macroparticle distribution from particles passing through the plane of the probe.
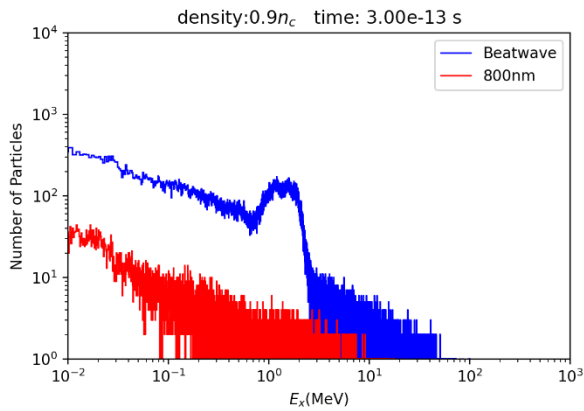
Figure 4.44: Comparison of time-integrated distributions for $n = 0.9n_c$ between the single laser and beat-wave case.

The importance of the cavity structures is shown when comparing the distributions measured by the probe as well as the density profile at the end of the simulation. The beat-wave, due to the presence of the secondary laser, allows these cavities to form throughout the plasma and generate the peak of 1-3 MeV electrons. Without the secondary laser, the laser cannot couple effectively to the latter half of the high-density plasma. Subsequently, the single laser interaction does not form cavities in the second half of the plasma while the beat-wave generates cavities throughout.

The MeV order electrons are also found to have varying levels of divergence, with electrons measured with negligible divergence, as the majority propagate with $\pm 5°$ divergence. The effect of the cavities in accelerating these MeV order electrons is also seen to persist many periods after the laser has left the plasma.
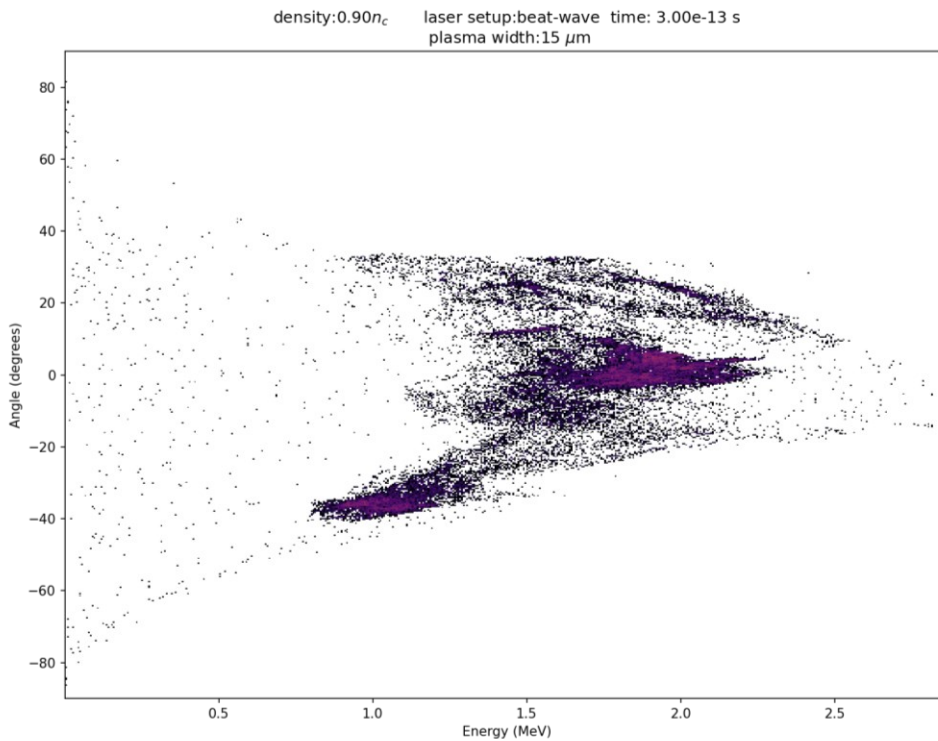
Figure 4.45: Divergence as a function of energy for electrons accelerated by the cavity structures present towards the end of the simulation.

4.3 Circularly Polarized Laser

The interaction between the previous plasmas and circularly polarized lasers are presented in this section. Laser pulses are treated as circularly polarized when two, equal intensity components with the same propagation vector have a 90° phase and are perpendicular to each other, as shown in Figure 4.46. Their superposition results in a seemingly rotating wave.
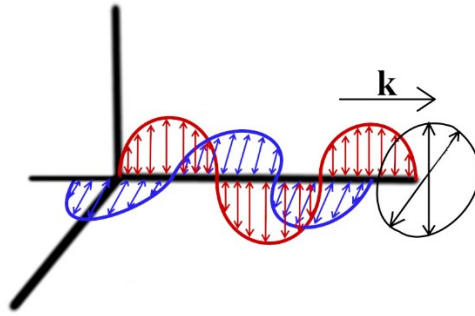
Figure 4.46: Individual, perpendicular linearly polarized lasers with a phase difference of $\frac{\pi}{4}$ copropagating form a circularly polarized wave.

Circularly polarized lasers have a different effect on the plasma compared to linearly polarized lasers, which can be considered a result of the differing ponderomotive force. Circularly polarized lasers are also of interest for the generation of low-divergence electron beams [21, 22].

4.3.1 Low Density Case

The first case examined for the circular polarization interaction is that of $n = 0.1n_c$. Just as in the linearly polarized case, both the single laser and beat-wave lead to interactions similar to the underdense case typically studied in wakefield accelerators; wakes form behind the pulse, and a strong sheath at the edge of the plasma after the wakes dissipate. Unlike the linearly polarized case, the propagating waves are unable to form a peak at the tail-end of the distribution. Additionally, the circularly polarized interaction leads to less maximum energy measured by the probe in both cases. However, the use of the beat-wave still leads to higher maximum energy and greater charge than when using the primary laser alone.
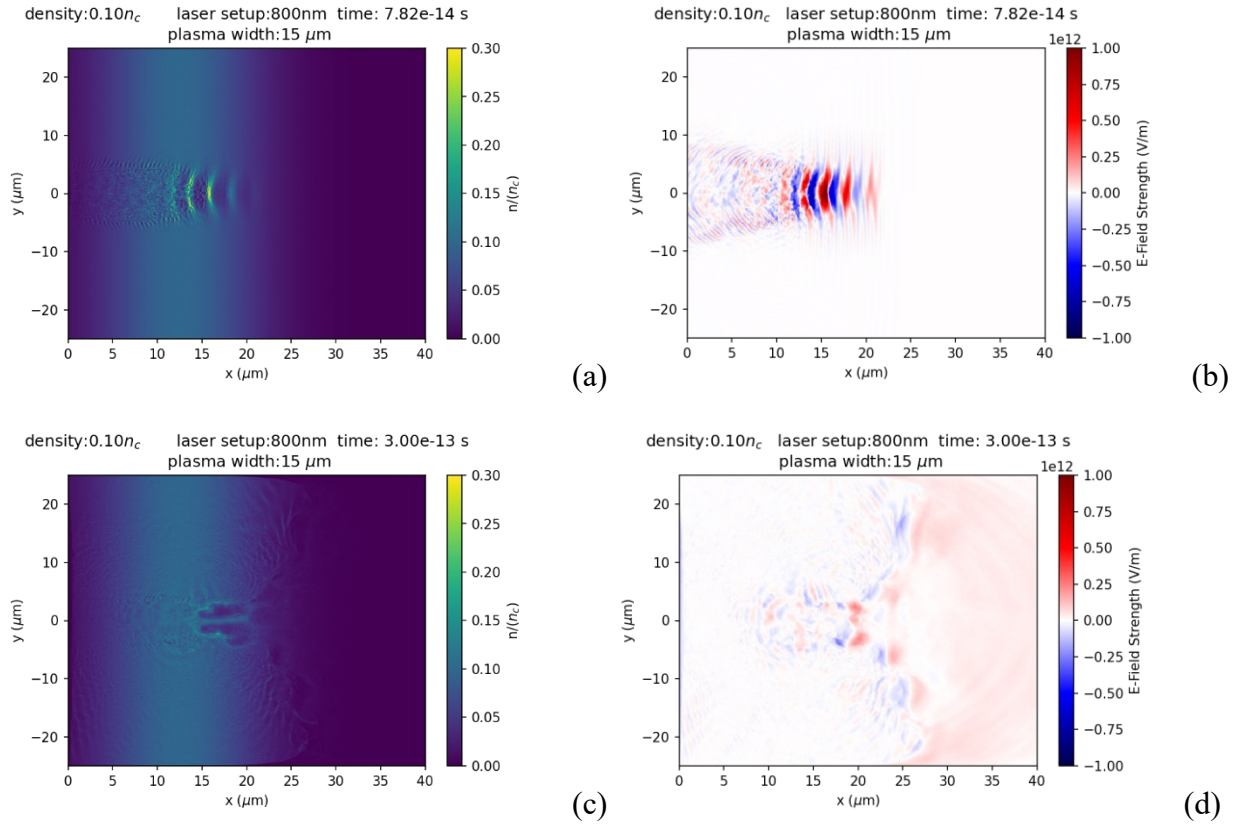
Figure 4.47: (a-b) Density and longitudinal field profiles as the primary laser propagates through and forms a wave. (c-d) Density and longitudinal field profiles at the end of the simulation.
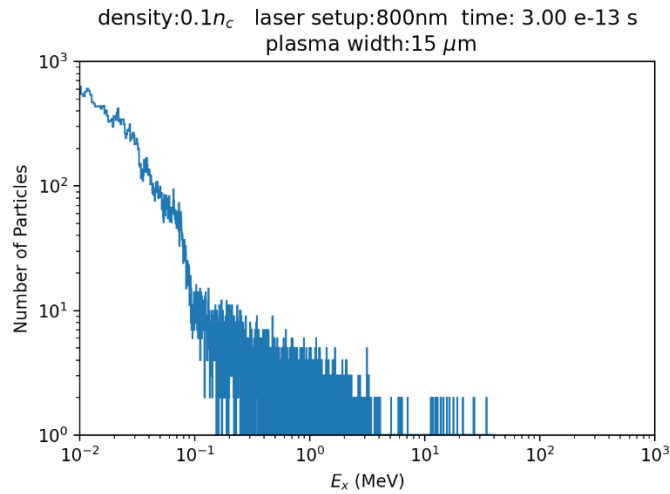
Figure 4.48: Electron macroparticle distribution integrated across the entire simulation for the circularly polarized, primary laser.
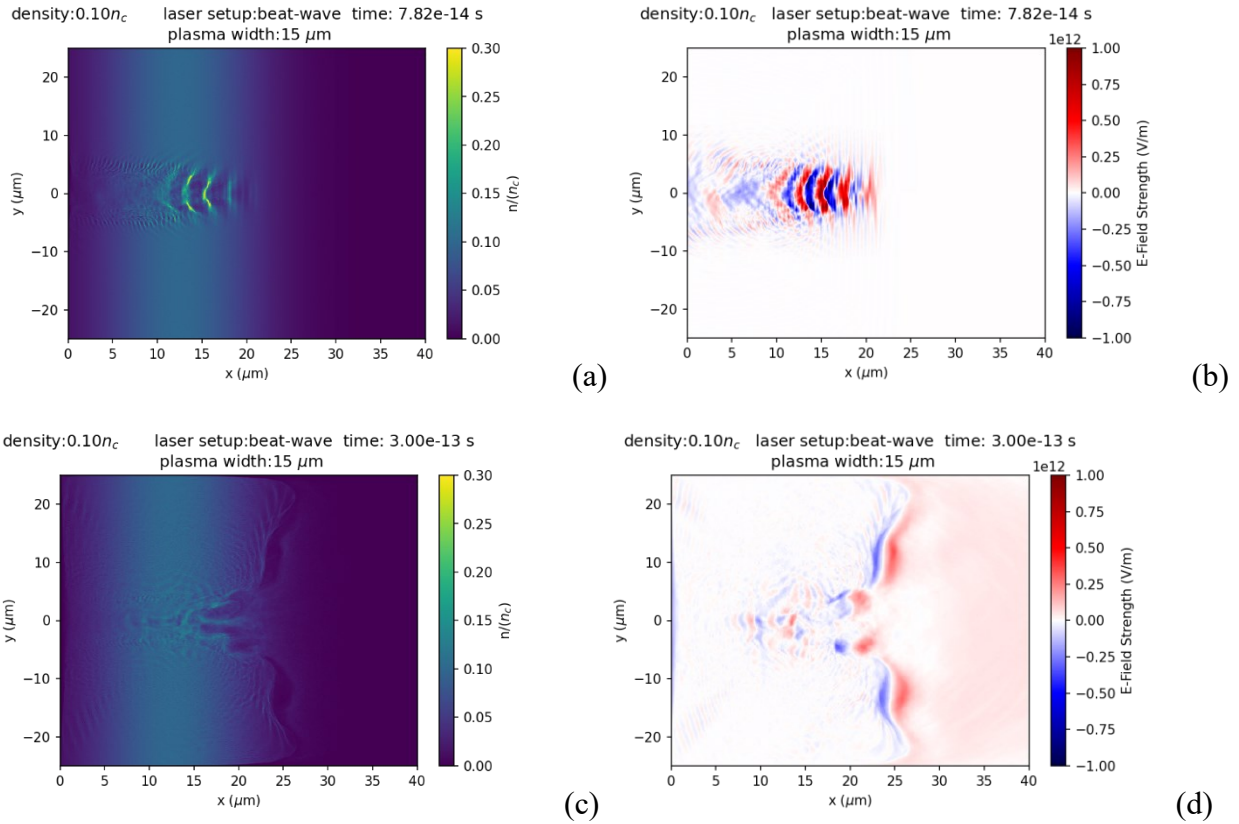
Figure 4.49: (a-b) Density and longitudinal field profiles as the beat-wave propagates through and forms a wave. (c-d) Density and longitudinal field profiles at the end of the simulation.
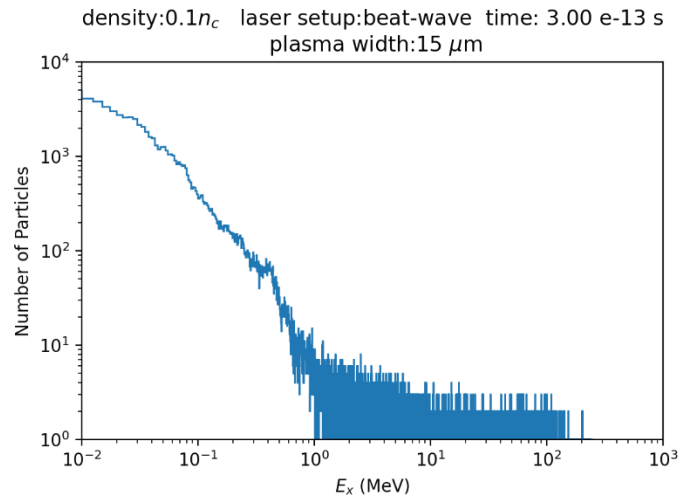
Figure 4.50: Electron macroparticle distribution integrated across the entire simulation for the circularly polarized beat-wave.

When examining the divergence of the interactions of both the primary laser and beat-wave, there is more uniformity in the circularly polarized case. Figure 4.49a and 4.47b both plot the diverging angle as a function of energy of the particles measured by the probe for the beat-wave case. The circularly polarized laser leads to an electron beam with particles diverging singularly at $\sim 20°$, while the linearly polarized case has two peaks which form at $\pm 10°$.

density:0.10n_c laser setup:800nm time: 1.60e-13 s
plasma width:15 μm

(a)

density:0.10n_c laser setup:beat-wave time: 1.64e-13 s
plasma width:15 μm
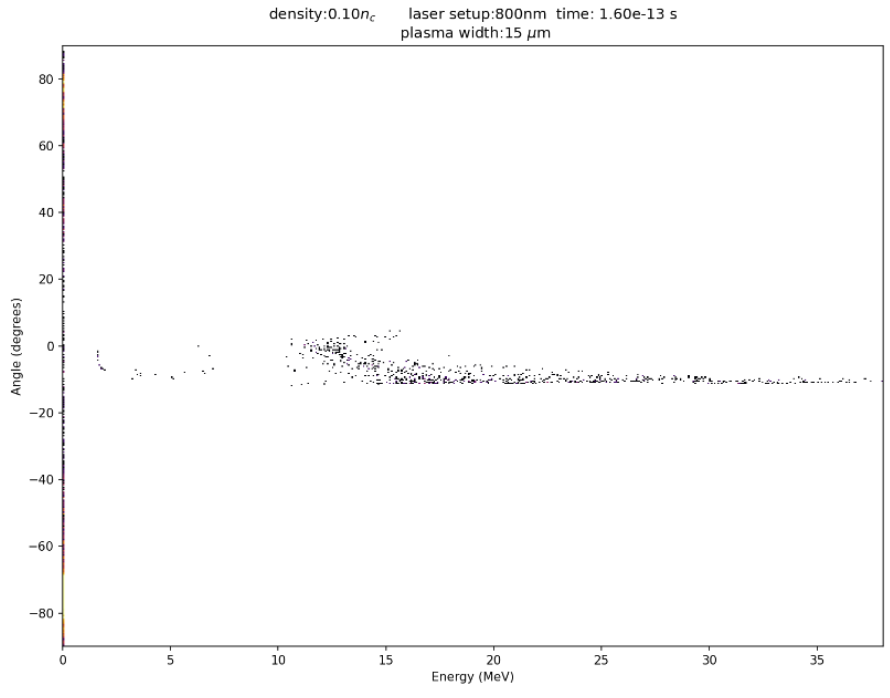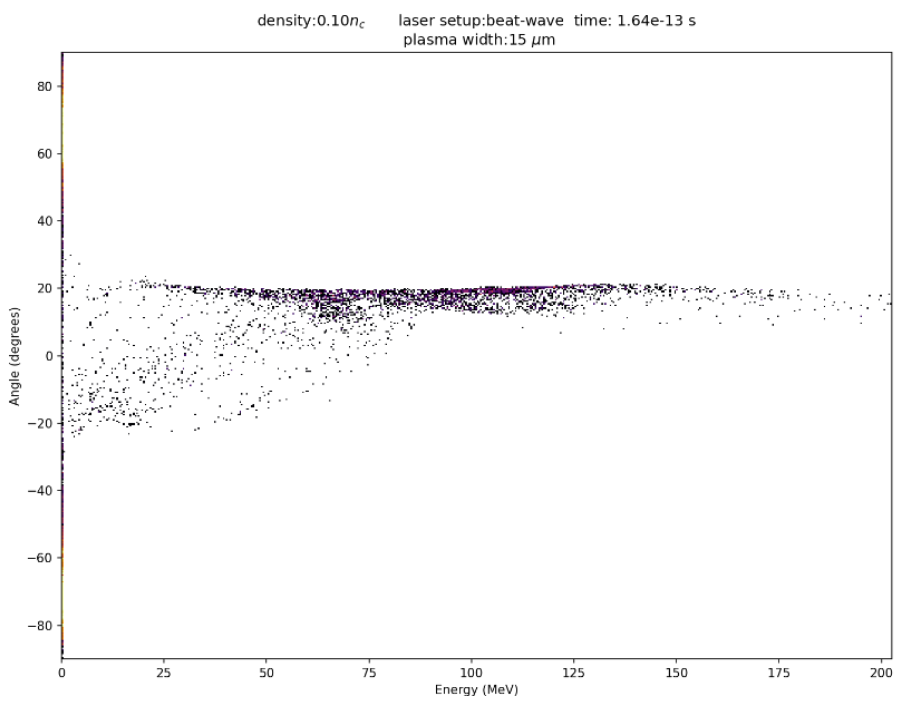
(b)

Figure 4.51: Divergence measured of the electron macroparticles measured by the probe as a function of energy for (a) the single, primary laser and (b) the beat-wave.

4.3.2 Quarter-Critical Density Case

The quarter-critical density plasma interaction with the circularly polarized primary laser exhibits similar overall behavior to the linearly polarized case in that the wave breaks rapidly and results in a strong sheath at the edge of the plasma at the exit edge, along with cavity structures remaining within the plasma itself. The density profile reveals a difference resulting from the polarization and its effects on the ponderomotive force. The end-of-simulation density profile of the linearly polarized laser shows the formation of several cavity structures forming throughout the plasma; the profile of the circularly polarized laser case shows the formation of a single, well-defined cavity at the $x = 10$ μm region rather than several. The result of this single cavity is reflected in the electron beam distribution, Figure 4.51 – the electrons do not reach the same charge, as the cavities are not spread throughout the plasma, but the peak is higher in comparison to the rest of the distribution from the presence of a singular cavity. Additionally, the tail of the distribution is not accelerated to the same extent as in the linearly polarized case, and the electron beam does not show more focus at this density that was visible in the $n = 0.1n_c$ case for the higher-energy population of electrons in the resultant beam. The lower energy electrons accelerated by the presence of the cavity, however, show more focus.

(a)

(b)

(c)

(d)

(e)

(f)
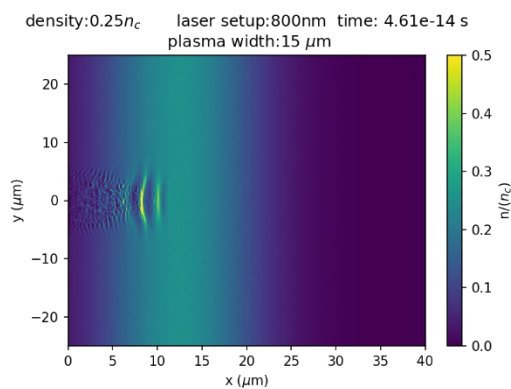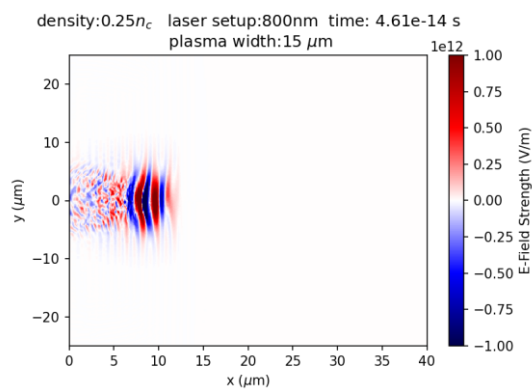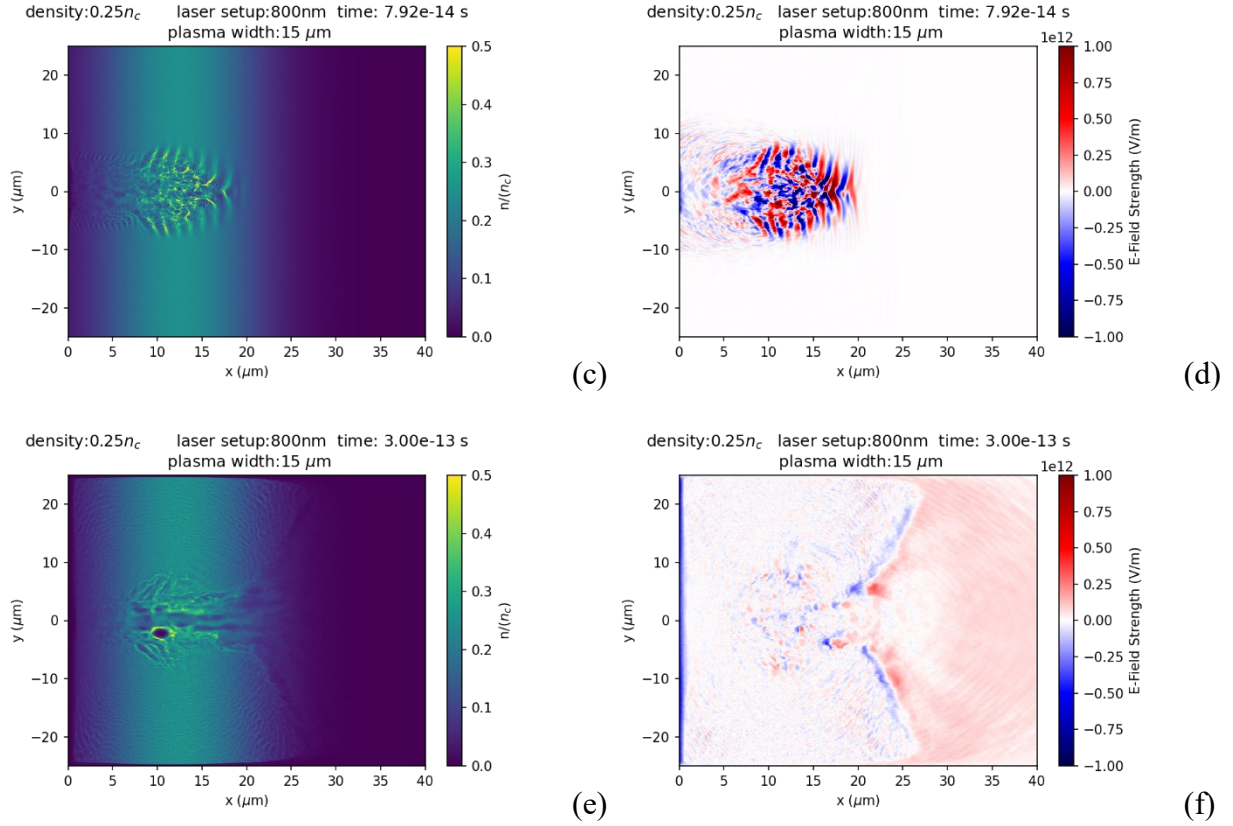
Figure 4.52: Wave evolution in the plasma for the circularly polarized primary laser interacting with $n = 0.25n_c$, where (a-b) shows the beginning formation of the wave, (c-d) shows the breakdown, and (e-f) shows the end behavior cavity formation.
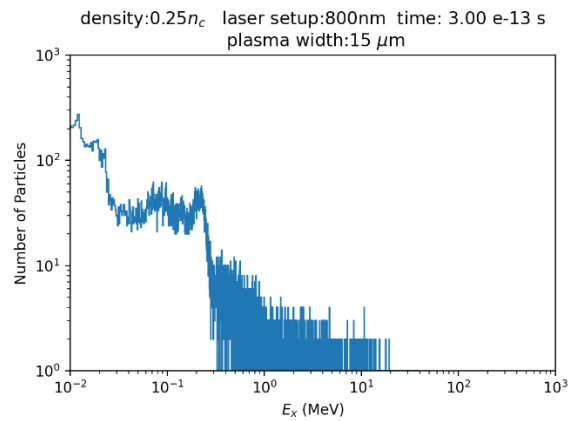
Figure 4.53: Electron macroparticle distribution of the circularly polarized primary laser interacting with the quarter-critical plasma.
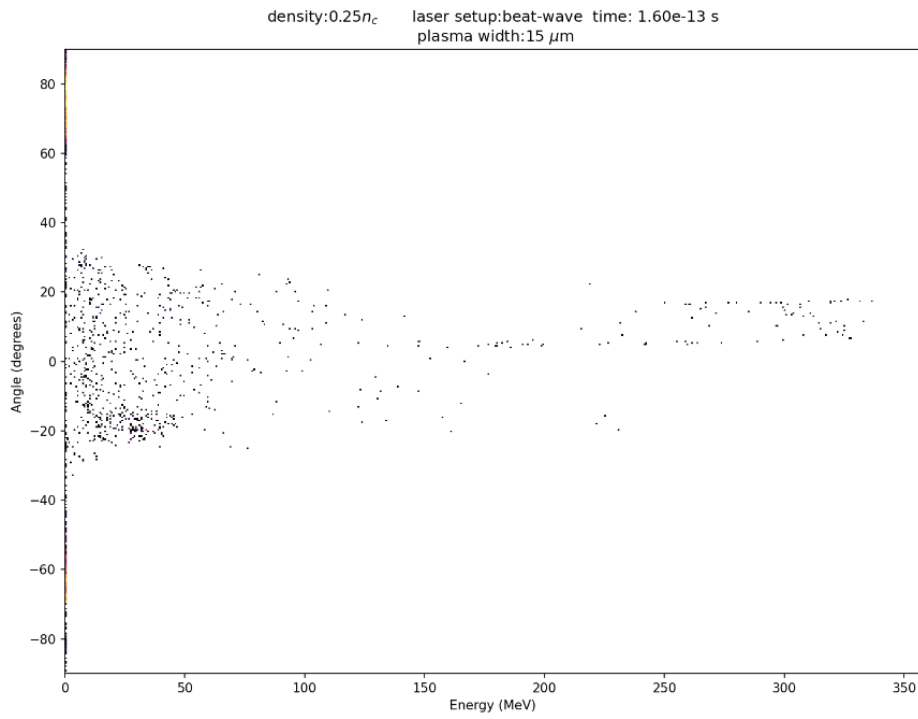
Figure 4.54: Divergence of the electrons following behind the pulse in the case of the circularly

polarized primary laser interacting with the quarter-critical plasma.

density:0.25n_c laser setup:800nm time: 2.29e-13 s
plasma width:15 μm
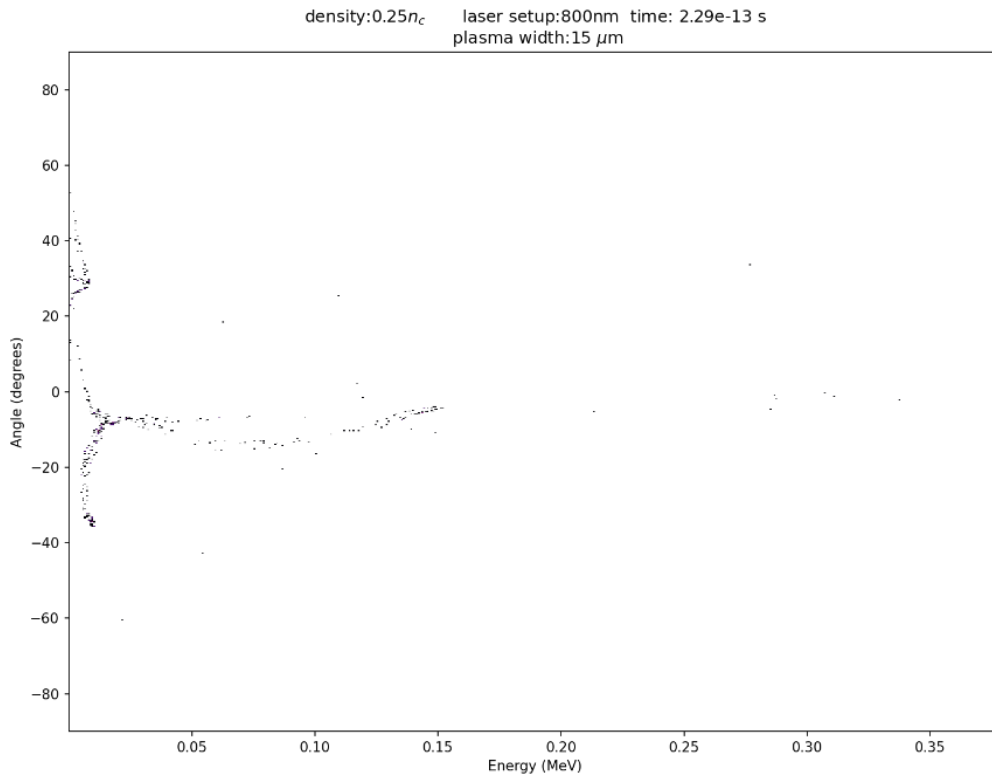
Figure 4.55: Divergence of the electrons accelerated from the cavity structures at the end of the simulation for the circularly polarized primary laser interacting with the quarter-critical plasma.

The circularly polarized beat-wave shows similar behavior to the primary laser, but the density profile of Figure 4.54(e) shows the deviation in behavior due to the presence of the secondary laser. The density profile of the end behavior now shows cavity structures more like the linearly polarized case than the circularly polarized primary laser in that several cavities form throughout the plasma rather than one prominent cavity forming in the middle of the plasma. This difference is once again reflected in the electron beam distribution, Figure 4.55, in that there is a flat region of the curve at ~1 MeV rather than a sharp peak at a singular energy. Additionally,

the maximum energy of electrons in the generated beam higher than the primary laser case and is comparable to that of the linearly polarized beat-wave.

The divergence of the electrons in the resulting beam measured by the probe are shown in Figures 4.54 and 4.55 which show the divergence of the high-energy electrons accelerating behind the pulse and lower energy electrons accelerated by the cavities respectively. In both situations, the beam shows greater focus than the linearly polarized case. The higher-energy electrons show tighter angular peaks, but the electrons which are in the 10 MeV order still have similar angular variance as the linearly polarized case. The lower-energy, 0.1 MeV order electrons all accelerate about a single peak with less spread, such as that shown in Figure 4.25. However, this divergence changes at different snapshots and shows emission of electrons focused at different angles towards the end of the simulation.
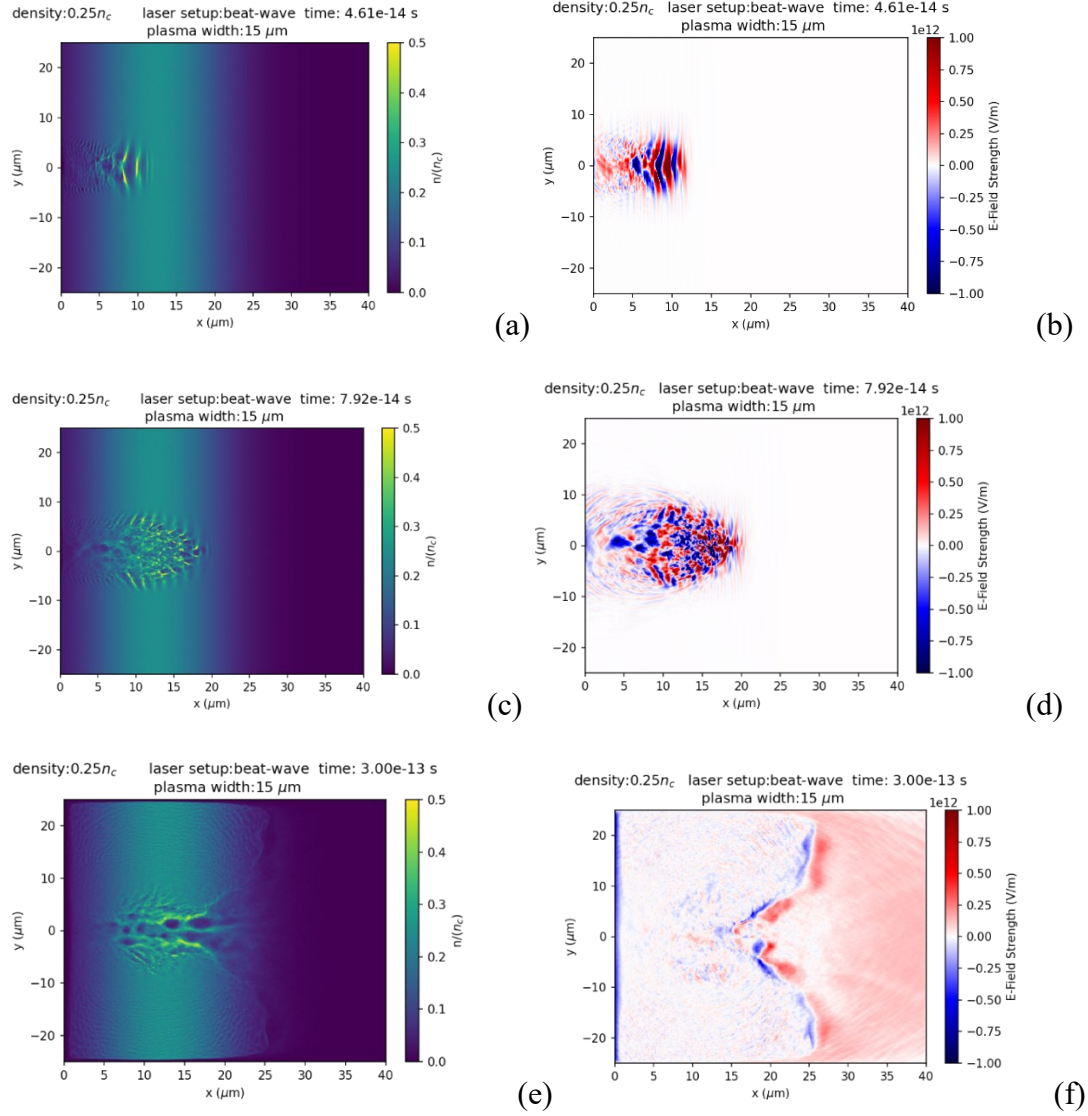
Figure 4.56: Wave evolution in the plasma for the circularly polarized beat-wave interacting with $n = 0.25n_c$, where (a-b) shows the beginning formation of the wave, (c-d) shows the breakdown, and (e-f) shows the end behavior cavity formation.
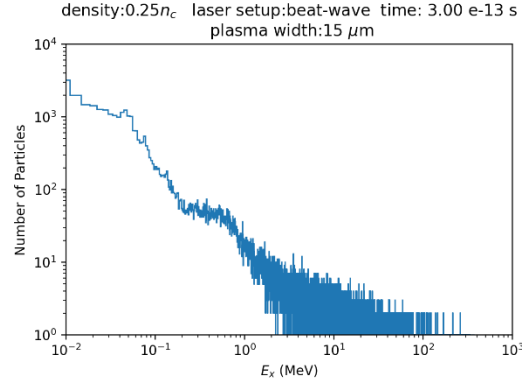
Figure 4.57: Electron macroparticle distribution of the circularly polarized beat-wave interacting with the quarter-critical plasma.

4.3.3 Half-Critical Density Case

The half-critical density interacting with the circularly polarized primary laser shows deviation from the linearly polarized case in the end-behavior. The initial interaction, however, continues to show similarity to the linearly polarized and quarter-critical case. The high-energy electron distribution of the half-critical density interaction has the same maximum energy as the quarter-critical case. The ripples which form in the density profile, 4.56(c), convert into two main cavity structures at both the front and back edge of the fwhm of the density profile rather than a single cavity forming at the front edge. Despite the formation of these cavities, the probe measures fewer electrons on the order of 0.1 MeV than in the previous cases. Additionally, the electron bunches have varying divergence, which is also seen in the linearly polarized case.
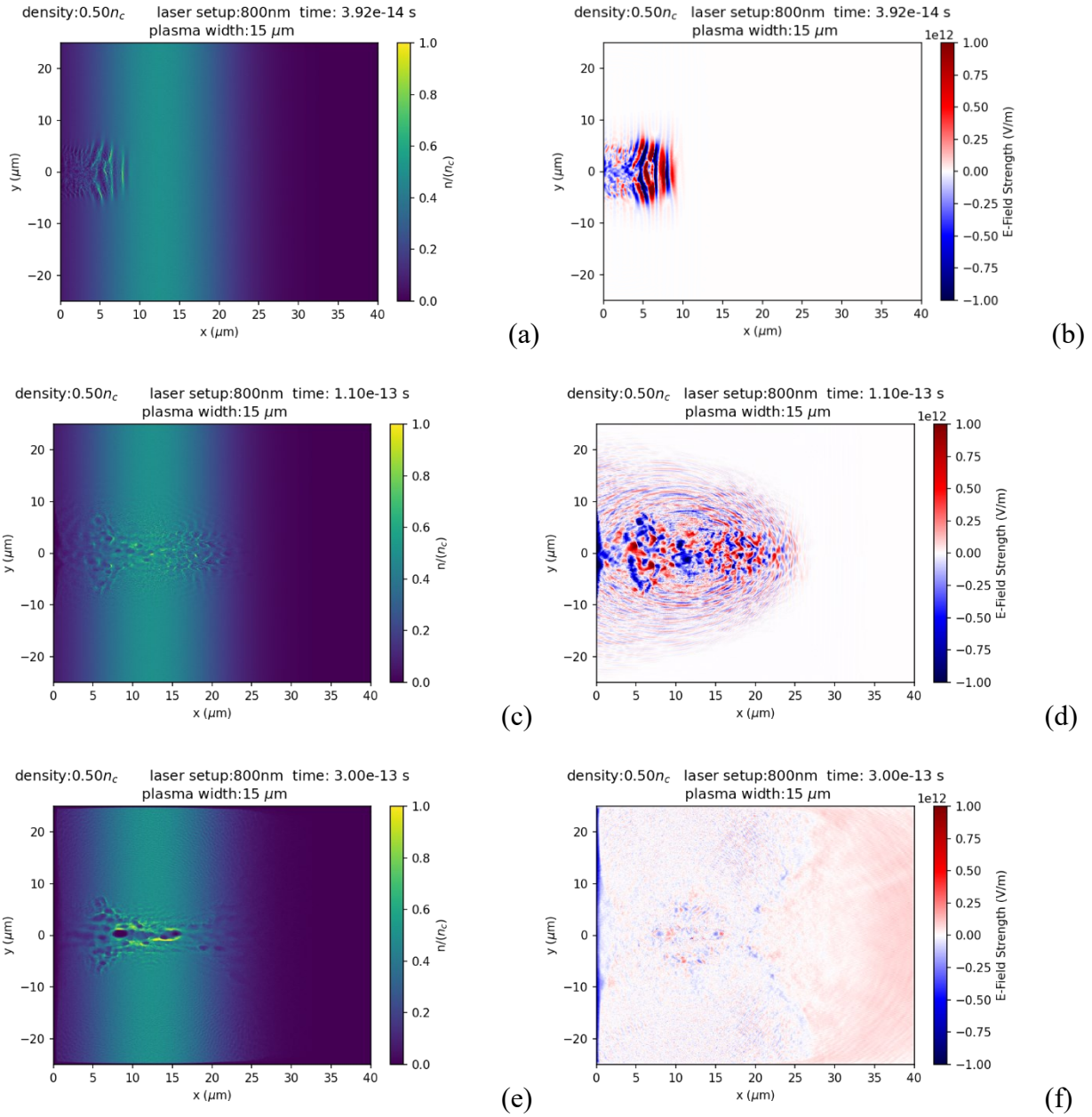
Figure 4.58: Wave evolution in the plasma for the circularly polarized primary laser interacting with $n = 0.5n_c$, where (a-b) shows the beginning formation of the wave, (c-d) shows the breakdown, and (e-f) shows the end behavior cavity formation at the front and back edge of the fwhm of the density profile.
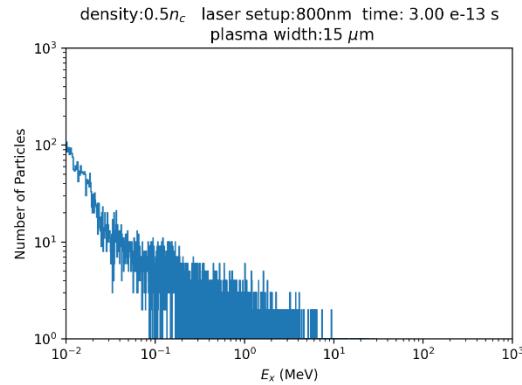
Figure 4.59: Electron macroparticle distribution of the circularly polarized primary laser interacting with the half-critical plasma.

The circularly polarized beat-wave leads to a channel-like formation as cavity structures form along the laser propagation axis. The cavity fields are again seen to grow stronger as the interactions move to higher density, and a sheath forms along the edge of the plasma at the end of the simulation. Compared to the linearly polarized case, the interaction resembles more of a quarter-critical interaction. The cavity structures form throughout the plasma, but the sheath at the exit edge of the plasma forms along the entire edge. This differs from the linearly polarized interaction behavior, as the sheath is less prominent and focused around the laser interaction region in the linearly polarized case. The result of this sheath can be seen in the lower charge measured by the probe. However, the effect of the cavities and density itself is seen through the peak of the measured probe distribution. The peak of the distribution matches the peak of the linearly polarized case with charge lower by an order of 10.

(a)

(b)

(c)

(d)
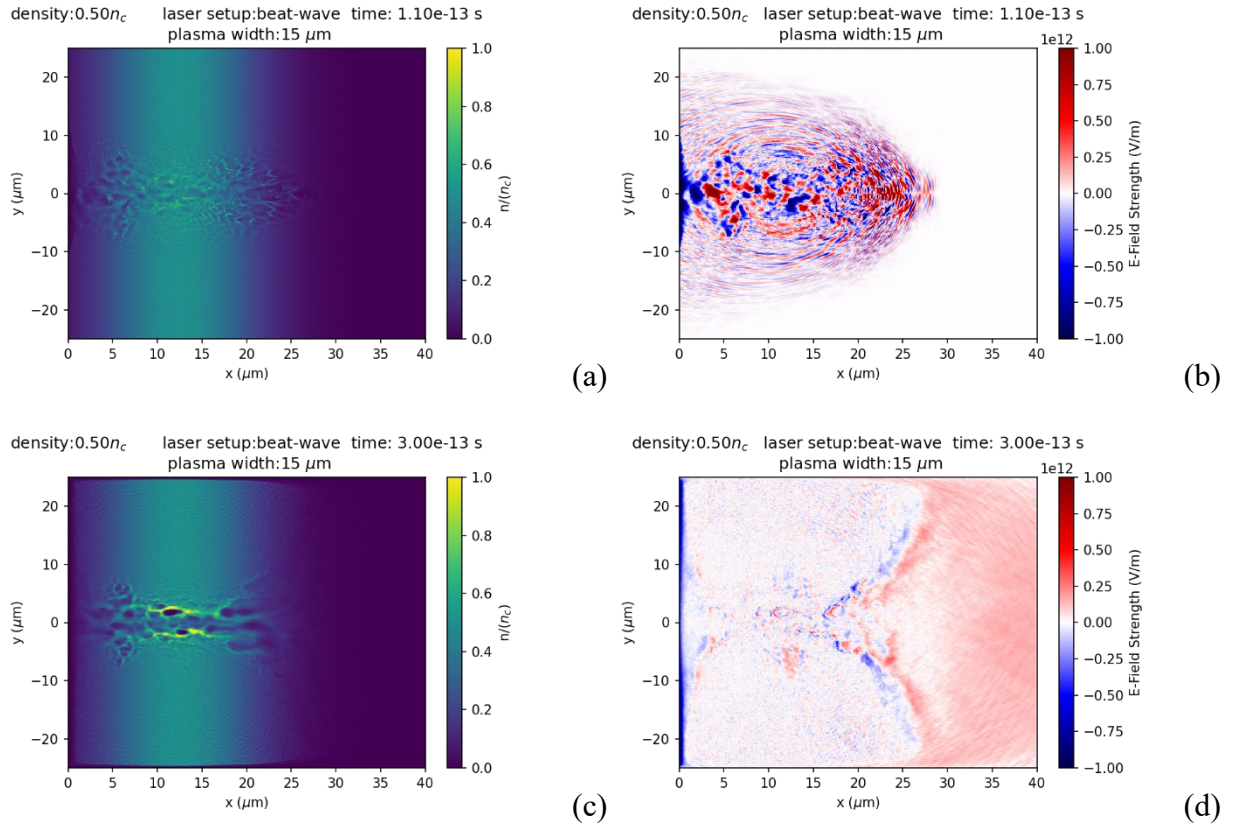
Figure 4.60: Density and longitudinal field profiles from the interaction of the circularly polarized beat-wave with the half-critical plasma (a-b) as the laser exits the plasma and (c-d) at the end of the simulation.
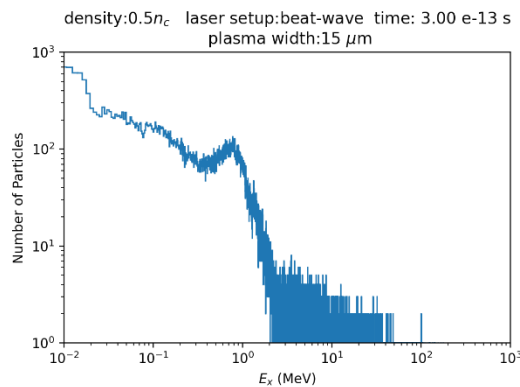
Figure 4.61: Electron macroparticle distribution of the circularly polarized beat-wave interacting with the half-critical plasma.

The impact of the beam polarization on electron divergence lessens as the density increases and causes a more turbulent laser interaction. Additionally, the acceleration of MeV order electrons at the end of the simulation continues to show little dependence on the polarization. Just as in the previous cases, Figure 4.62 shows probe measurements of electrons focusing along a single angle at different points in time at similar angles to that of the linearly polarized lasers.

(a)

density:0.50n_c laser setup:beat-wave time: 2.60e-13 s
plasma width:15 μm

(b)
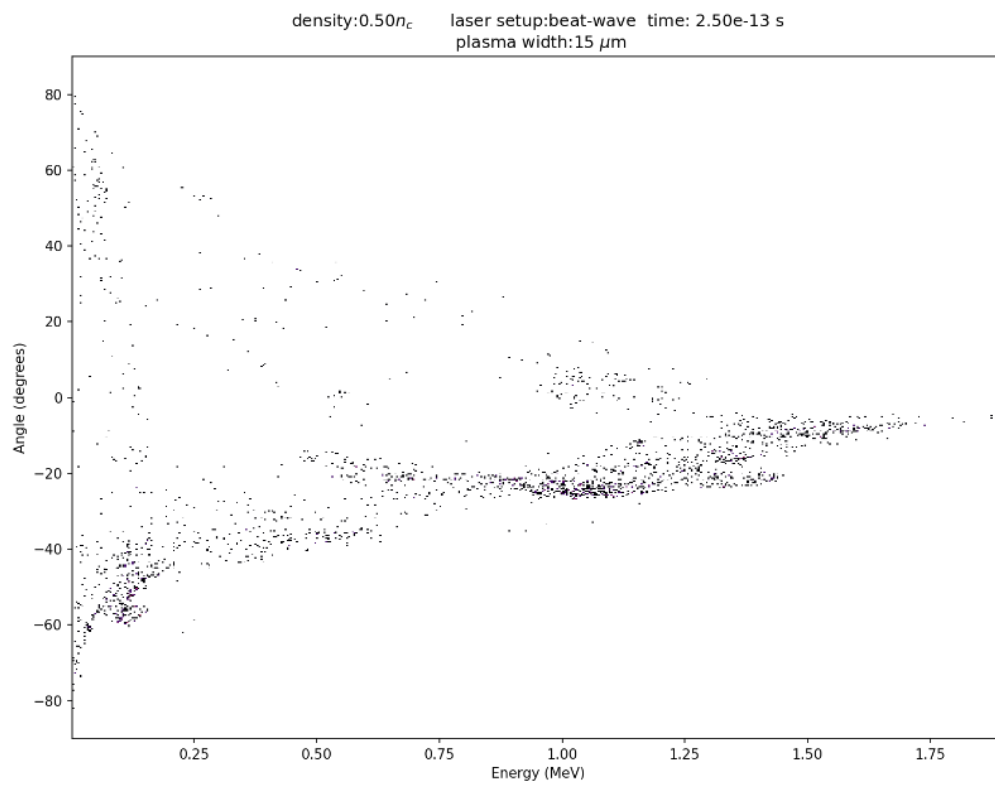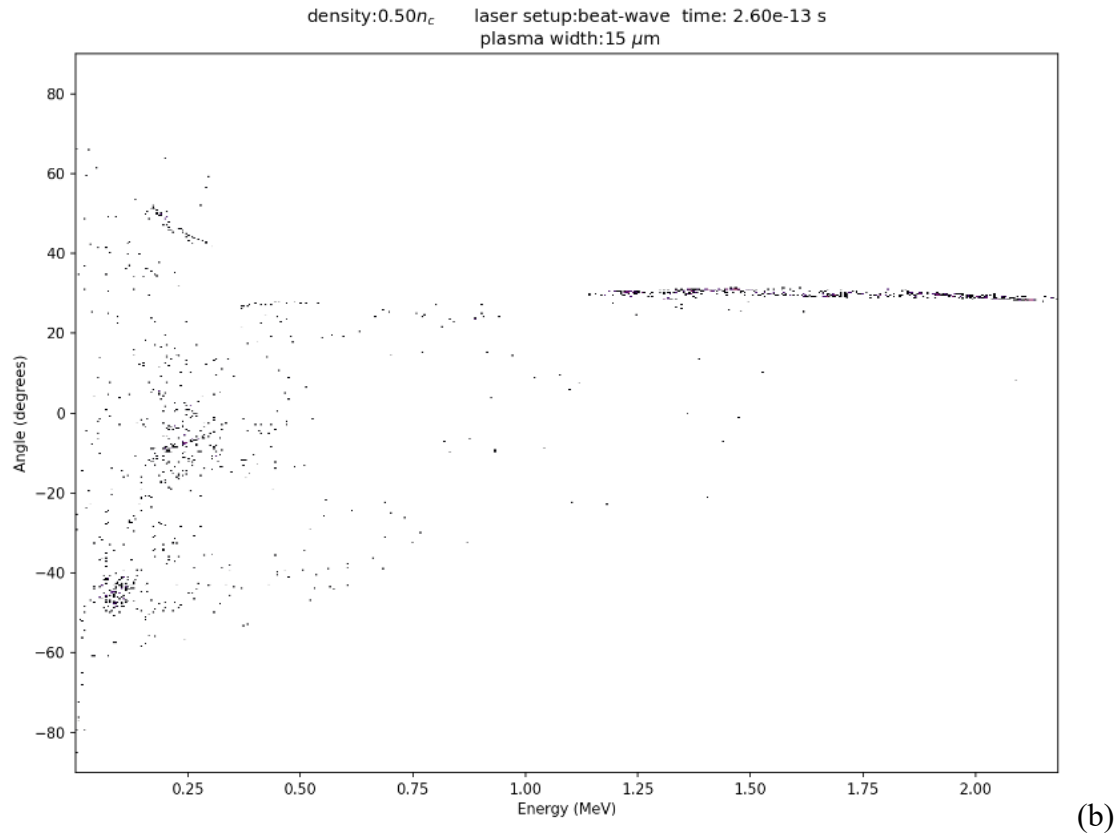
Figure 4.62: Divergence of 1 MeV order electrons accelerated by the cavities in the half-critical

plasma interacting with the circularly polarized beat-wave with (a) 10 fs earlier than (b).

4.3.4 Near-Critical Density Case

The circularly polarized primary laser is insufficient in creating a proper electron beam.

The probe barely measures electrons after the laser exits the simulation with much lower energy

compared to the other cases. The interaction can be examined through the evolution of the

density and field profiles in Figure 4.64. Figure 4.64 (a) and (c) show that the primary cavity

formation is locked into the first half of the plasma rather than throughout. This shows that the

laser has insufficiently coupled to the entire plasma region which leads to the low charge and

energy measured by the probe.
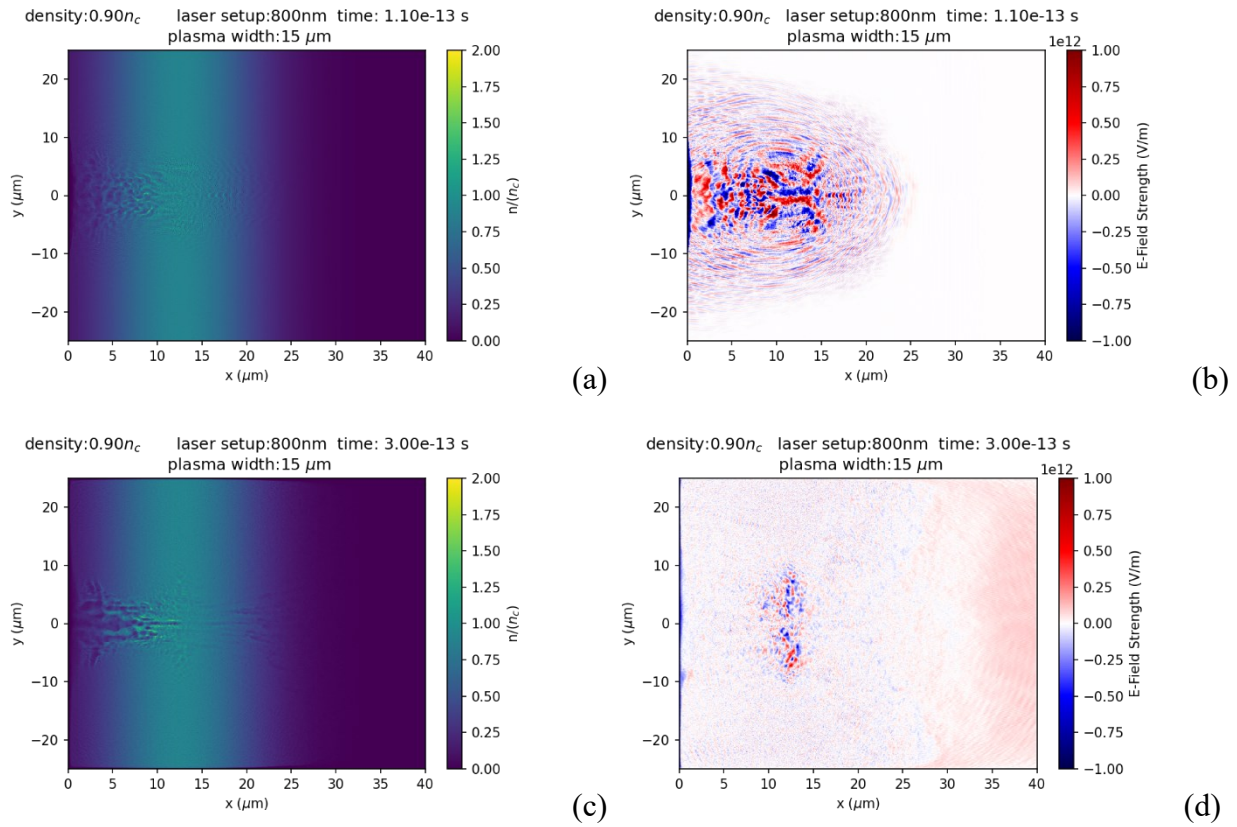
Figure 4.63: The density and longitudinal field profiles for the circularly polarized primary laser

interacting with $n = 0.9n_c$ (a-b) when the laser exits the plasma and (c-d) at the end of the

simulation.
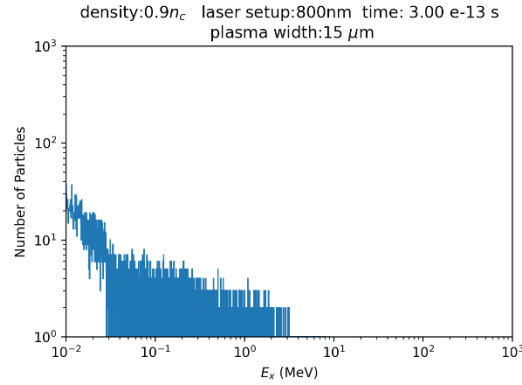
Figure 4.64: Electron macroparticle distribution of the circularly polarized primary laser interacting with a peak of $n = 0.9n_c$.

The beat-wave case shows unique behavior through the presence of two peaks at ~0.1 MeV and ~2 MeV in Figure 4.66. The two distinct peaks coincide with the formation of three prominent cavity structures along the laser propagation axis. This result is similar to that of the quarter-critical interaction with the circularly polarized primary laser generating one prominent cavity responsible for the end-behavior acceleration; in the quarter critical case, the single cavity led to a peak ~0.2 MeV. The presence of these distinct cavities allows electrons to selectively accelerate to the 0.1-1 MeV order through the channel which forms.

The linearly polarized beat-wave has a broad peak which forms from 1-3 MeV accompanied by the presence of many cavities throughout the plasma. However, the fewer cavities in the circularly polarized beat-wave interaction lead to a subsequently narrower peak in the energy spectrum compared to the linearly polarized beat-wave case at the same density. The presence of more cavities in the linearly polarized case thus shows a wider acceleration region for electrons in the bulk plasma to accelerate to the MeV order.

(a)

(b)
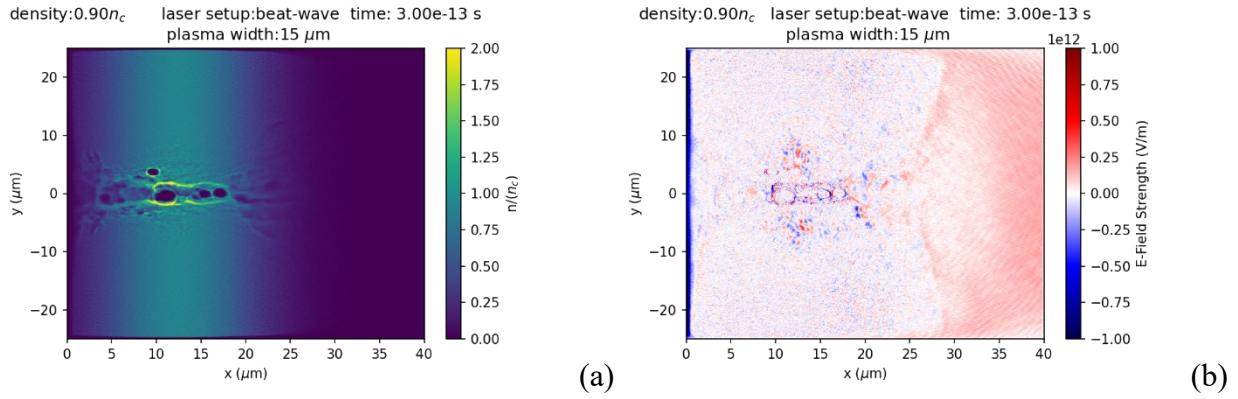
Figure 4.65: The density and longitudinal field profiles for the circularly polarized beat-wave interacting with $n = 0.9n_c$ after the laser has exited the simulation.
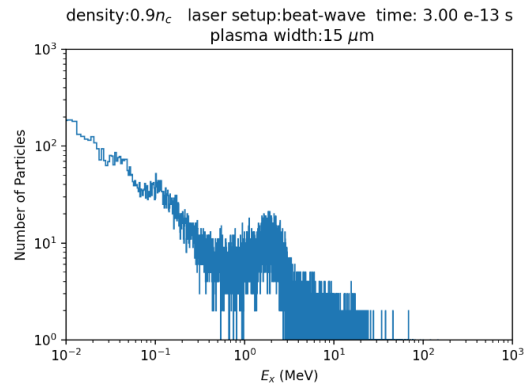
Figure 4.66: Electron macroparticle distribution of the circularly polarized beat-wave interacting with a plasma with peak density $n = 0.9n_c$.

Chapter 5 - Application of Results to Electron Radiotherapy

The objective of this work is to find a potential setup for an electron beam suitable for electron radiotherapy using a laser-plasma accelerator. Higher density plasmas are used to approach the resonance condition of a beat-wave, and higher-density plasmas are also good in applications requiring large charge due to the presence of more particles in general. Current LINAC-based electron radiotherapy beams require energies of 5-25 MeV with a dose rate of 1-10 Grays/min (Gy/min) [10]. The unit Gray represents the amount of radiation absorbed by a target and has the base units of J/kg.

The dose rate is a metric for how much radiation is deposited at a depth determined by the radiation type and energy. Dose rate can be calculated using the particle and/or energy fluence using the following formula [10]:

$$D(E) = 1.602 * 10^{-10} \Phi(E) \cdot \left(\frac{dE}{\rho dx}\right) (5.1)$$

$\Phi(E)$ is the particle fluence, ie the total number of particles at various energies in the beam distribution per unit area, and $\left(\frac{dE}{\rho dx}\right)$ represents the mass stopping power of electrons through water, and $1.602 * 10^{-10}$ represents the conversion from MeV/g to Gy.

When comparing the distributions between the primary laser and beat-wave interactions, such as in Figure 4.40, the beat-wave interaction consistently leads to higher energy beams with greater overall charge. These results continue despite the use of the same overall laser energy of 200 mJ for both cases. The charge of electrons with the required 5-25 MeV energy is considered

to find the optimal density. As expected through the energy gain predicted in laser-plasma theory, the $n = 0.1n_c$ case leads to the highest maximum energy. However, the electron beam in this work is examined and tailored towards electron radiotherapy requirements, meaning the highest energy is not the most important metric. Figure 5.1(b) shows the optimal density in generating charge greater than 5 MeV is $n = 0.9n_c$. This density readily meets the 5-25 MeV requirement for electron radiotherapy. Additionally, the electron population of electrons greater than 1 MeV in energy is optimized at $n = 0.9n_c$. The generation of these electrons is seen as the peak in the distribution between 1-3 MeV. This peak is present in the $0.5n_c$ case and above, showing a different acceleration regime than in the $0.25n_c$ and $0.1n_c$ cases.
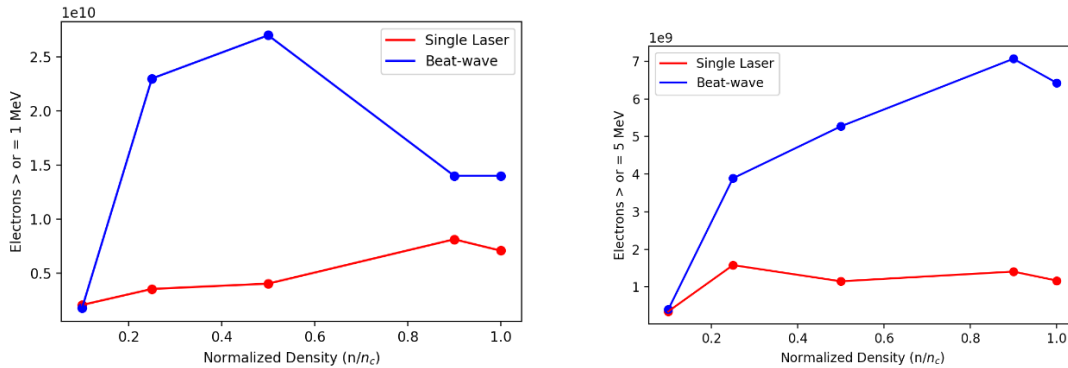
Figure 5.1: Electrons measured by the probe after accounting for weighting of each particle for the linearly polarized single-laser and beat-wave for (a) electrons with energy of at least 1 MeV and (b) electrons with energy of at least 5 MeV.

By using the macroparticle distribution measured by the probe in each case, the particle fluence of electrons at a specific energy can be determined and used to calculate the dose rate. The dose rate is calculated for the $n = 0.9n_c$ of electrons at 5 MeV using equation 5.1 with mass stopping power through water calculated using the NIST database ESTAR [20] as

$1.971 \; MeV \; \frac{cm^2}{g}$. The cross section of the particle fluence, ϕ, follows a simple assumption that

the electron beam follows the spot size of the laser and thus has an area of $A = \frac{\pi d_{fwhm}^2}{4}$.

Equation (5.1) thus results in a dose of $2.4 * 10^6$ Gy, which can be considered as $2.4 * 10^6 \frac{Gy}{s}$ if

the repetition rate is on the order of 1 Hz. Therefore, the electron beam generated by the NCD

interaction easily meets the dose requirement currently met by LINACs. A laser beat-wave

interacting with the presented laser parameters and a target at $n = 0.9 n_c$ proves the most

favorable setup for short penetration depth electron radiotherapy based on the high charge, MeV

order electrons generated. Additionally, the simulations of linearly polarized lasers lead to more

charge than the circularly polarized laser, while the circularly polarized lasers are seen to emit

more focused electron bunches of high-energy electrons than the linearly polarized lasers at the

lower to moderate densities. For the end acceleration, the differing ponderomotive force of the

circularly polarized lasers leads to fewer, distinct cavities with steep density gradients compared

to the linearly polarized interactions.

When considering the generation of 1 MeV or higher energy electrons as the goal, a

target of $n = 0.5 n_c$ leads to twice as many electrons compared to $n = 0.9 n_c$ for the linearly

polarized beat-wave. As such, tailoring of the laser parameters and target may increase this lower

limit to the 5 MeV required for electron radiotherapy and create a higher dose beam. However,

the charge generated for 5 MeV order electrons at $n = 0.25 n_c$ and $0.1 n_c$ is sufficient in

generating at least 10 Gy/min from the simple assumptions made in dose calculation.
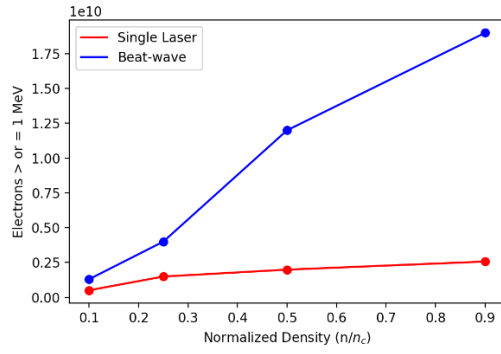
(a)
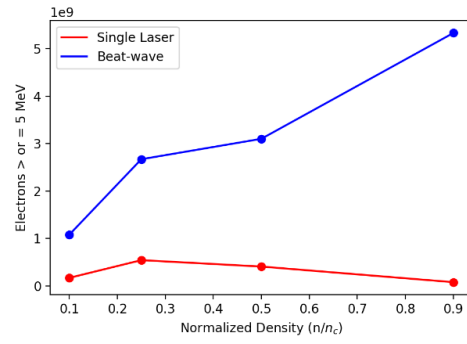
(b)

Figure 5.2: Electrons measured by the probe after accounting for weighting of each particle for the circularly polarized single-laser and beat-wave for (a) electrons with energy of at least 1 MeV and (b) electrons with energy of at least 5 MeV.
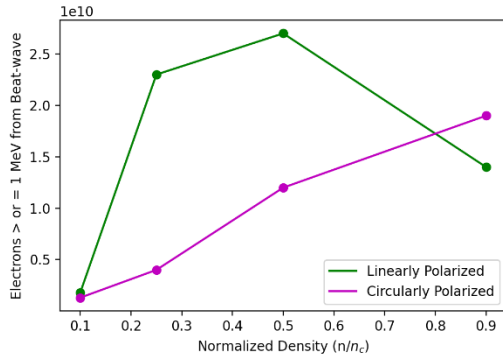
(a)
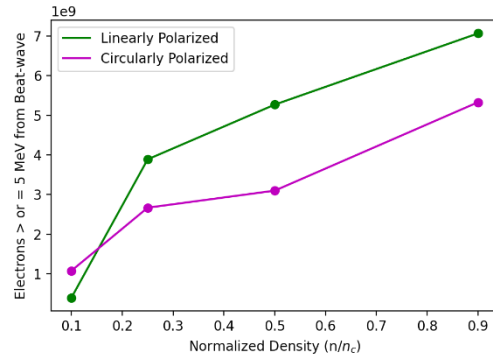
(b)

Figure 5.3: Electrons measured by the probe after accounting for weighting of each particle comparing the results of the differently polarized beat-wave for (a) electrons with energy of at least 1 MeV and (b) electrons with energy of at least 5 MeV.

Chapter 6 - NCD Electron Acceleration Mechanism

From a quarter of the critical density onwards, the main mechanism of electron acceleration shifts away from the known underdense behavior towards a more turbulent method. The moderately dense plasmas of $0.25n_c$ and $0.5n_c$ both show the influence of a sheath forming at the edge of the plasma, while $0.5n_c$ and $0.9n_c$ show the importance of the cavity structures forming in the plasma. The higher density cases with the most prominent cavity formation are shown to accelerate more electrons to the order of 1 MeV than in the cases without. These cavity structures are known as cavitons [13, 23] which trap resultant plasma waves and lead to a soliton wave.

Cavitons are a type of modulational instability arising from a strong initial Langmuir wave amplitude. Cavitons form from the conversion of the laser into a Langmuir wave through the ponderomotive force which then couples and resonates with a local region of the NCD plasma; the plasma in the NCD regime only supports local regions of plasma waves from this interaction from the nature of high-density interactions breaking the pulse and shortening the characteristic length of the resulting wave. The ponderomotive force of the local waves creates a density cavity if the amplitude is sufficiently high which forms the caviton [13, 23, 24]. These cavitons thus form solitons as the density gradients of the cavitons trap the local, high-frequency waves. As the plasma evolves, the caviton continues to widen until reaching 10-20λ_{Debye} [13]. This can be seen in Figure 6.2, where the interaction of a beat-wave and $n = 0.9n_c$ plasma leads to cavitons with a width of 1.2 μm with a debye length of ~ 0.06 μm. The caviton width matches the expected range as it goes up to $20\lambda_{Debye}$. The density cavity creates a polarized region between the electrons and background ions. The cavitons persist long enough for the ions to

experience sizable repulsion between each other [27]. This repulsion causes the ions to start

drifting away from equilibrium and form the channel structures visible in the end-simulation

density profiles of Chapter 4. The damping of the solitons thus forms an ion wave which leads to

the acceleration of ions [13, 26].
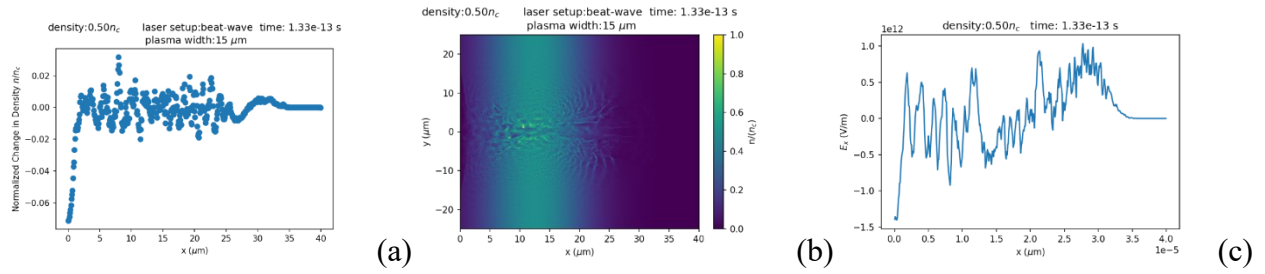
Figure 6.1: (a) 1D averaged density profile plot showing the formation of cavitons in (b) the 2D

density profile for the linearly polarized beat-wave interacting with $n = 0.5n_c$. (c) 1D cut of the

large amplitude plasma waves formed and trapped within the regions of the cavitons.
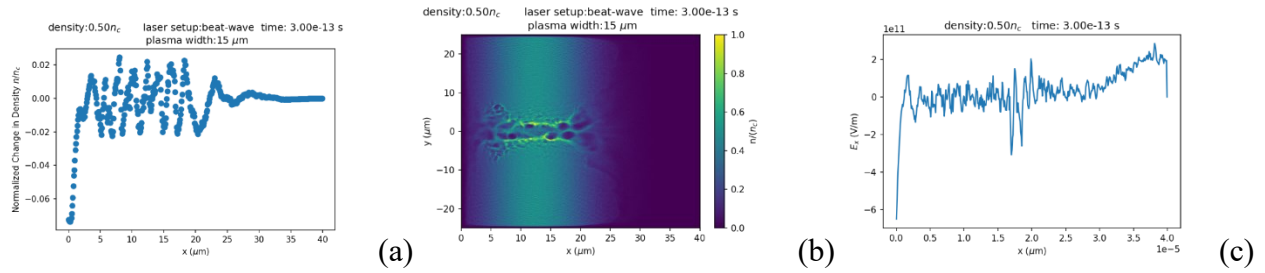
Figure 6.2: (a) 1D averaged density profile showing the cavitons fully formed at the end of the

simulation in (b) the 2D density profile for the linearly polarized beat-wave interacting with $n =$

$0.5n_c$. (c) 1D longitudinal field profile showing the high-frequency solitons trapped within the

cavitons.

   Cavitons are seen in the results of this work in the plasma densities corresponding to

quarter-critical, half-critical, and $0.9n_c$. Additionally, the most prominent formations occur in the

beat-wave cases. The cavitons form the best in these cases due to the ability of the plasma to

couple and resonate with the laser and cascade into higher wave modes easier with the beat-wave. This is supported by the plasma frequency at quarter-critical and $0.9n_c$, where the plasma frequency is half and approximately equal to the beat frequency respectively. At half-critical, the plasma frequency is half the frequency of the secondary laser. The efficient coupling and conversion at these densities is shown in Figure 5.1 which compares the particle count measured by the probe of 1 MeV electrons between the linearly polarized primary laser and beat-wave. The charge of the $n = 0.9n_c$ case for the primary laser shows a peak of electrons with a comparable charge resulting at the critical density itself. The close values of the laser and plasma frequencies enhance the charge through the resonant interaction. In the beat-wave interaction, the resonance occurs in the densities corresponding to half the primary and secondary laser frequency at the quarter and half critical density respectively. Additionally, the 1 MeV order electrons can be considered a result of this resonance and soliton formation.

Chapter 7 – Conclusion

7.1 Summary

The purpose of this work is to examine the interaction of lasers with NCD plasmas to obtain a feasible and optimal setup for electron radiotherapy. 2D simulations were conducted using a PIC code called EPOCH to examine the behavior of the interaction and the resulting electron beam. To compare to the currently used linear accelerators, the generated electron beam must have electrons with energies of 5-25 MeV and a sufficient dose. The use of an NCD plasma as the target is shown to facilitate bulk acceleration of electrons at the lower end of this desired energy range with a large dose. The electrons measured through these simulations show similar energies and high radiation dose, especially in the beat-wave cases. While $n = 0.9n_c$ led to the highest charge generation of 5 MeV order electrons, all higher densities deviating from underdense expectations lead to sufficient dose. The setup thus seems to be a feasible alternative electron source for radiotherapy compared to linear accelerators.

First, the interaction of the plasma with a linearly polarized setup was examined. The lowest density of $n = 0.1n_c$ showcased behavior reminiscent of underdense interactions geared towards LWFA. As the peak density of the plasma increases, lower, MeV order electrons begin to accelerate in bulk. The mechanism for these electrons accelerating is determined to be through cavitons and the ability of the laser to generate cavitons throughout the plasma. The cases where cavitons could form in one specific region of the plasma lead to fewer MeV order electrons measured by the simulated probe in vacuum. In these higher density cases, the beat-wave allowed for better penetration into and coupling with the plasma. This results in a charge ten times greater than that of the single laser interaction. The caviton acceleration is aided by the

lesser sheath formed along the back edge of the plasma, as electrons can then accelerate and leave the plasma without interference from the sheath.

The same plasma and laser parameters were simulated with circular polarization rather than linear. The circularly polarized lasers led to better focus in the resulting electron beams in the low and quarter-critical density cases compared to the linearly polarized lasers. However, the circularly polarized lasers showed little benefit in the higher density cases of half-critical and $0.9n_c$ where caviton formation becomes the main accelerating mechanism. The charge generated by the beat-wave is similar between the circular and linear polarization cases. However, circular polarization leads to generation of fewer cavitons than linear polarization. Additionally, the peaks in the electron count graphs shown in Chapter 5 at quarter-critical and half-critical for linear polarization are absent in the circular polarization graph. The linearly polarized case thus shows better mode conversion/plasma wave cascade in caviton and soliton formation.

7.2 Potential Next Steps

Through examination of these results, a potential experimental setup involving a target of $n = 0.9n_c$ with a linearly polarized beat-wave proves favorable. As such, the transition to an experimental setup is a logical next step in verifying the feasibility of this regime in electron radiotherapy. However, the soliton acceleration mechanism of the quarter-critical and half-critical case leads to a much higher amount of 1 MeV order electrons than at $0.9n_c$. The laser parameters and density can be altered to examine the possibility of raising the peak seen in the charge distribution spanning from 1-3 MeV to 5 MeV, thereby meeting the minimum energy desired by electron radiotherapy. This can be done by examining the effect of the laser intensity which can be altered through parameters such as the spot size and pulse duration. Additionally,

the generation of the plasma target itself proves a challenge due to the high density desired. Gas jet are used to create plasma targets and can vary the nozzle to meet different density requirements, such as the profile or the density value itself. Experiments utilizing an 800nm laser have been shown to generate maximum densities of $\frac{n}{n_c} = 0.43$ [21]. However, going to a density such as $\frac{n}{n_c} = 0.9$ proves difficult due to the high pressure generated from such a configuration. As such, a potential experimental setup would require careful consideration of the plasma target. However, the simulations shown in this work show that sufficient dose can be created from the interaction between the beat-wave and $n = 0.5n_c$ and $0.25n_c$ to keep in line with the caviton formation seen as the density increases.

With a computational study, the ion characteristics can be examined in addition to the electron characteristics; additionally, 3D simulations can be conducted to supplement findings from 2D simulations. The structures seen in the higher density plasmas show the formation of cavitons which are known to decay into Ion Acoustic Waves [13]. The ion behavior in these interactions can thus be examined to determine feasibility of this laser setup for other applications, such as proton-based radiotherapy. To ensure that the characteristics are properly captured, 3D simulations can support the 2D work conducted. The transition to 3D is desired due to the impact the transition from 1D to 2D had on the simulations. In lower densities, 1D simulations proved sufficient in capturing wakefield behavior. However, as the density increases, 1D becomes insufficient in capturing effects from parameters such as the laser spot size. Likewise, 2D effects may not properly capture effects such as the effect of a circularly polarized laser on the plasma due to no particles simulated in the direction of the laser oscillating in the z-direction. However, 2D simulations prove sufficient in examining the effect of the linearly polarized lasers as well as caviton generation.

References

[1] P. J. Bryant, "A brief history and review of accelerators," *Cern Eur. Organ. Nucl. Res.*, pp. 1–1, 1994.

[2]   N. Pichoff, "Introduction to RF Linear Accelerators (LINACS)," *CAS-CERN Accel. Sch.*, pp. 105–128, 1994.

[3]   M. Vretenar, "Linear accelerators," *Proc. CAS-CERN Accel. Sch. Adv. Accel. Phys.*, vol. 009, no. August 2013, pp. 295–329, 2013, doi: 10.5170/CERN-2014-009.295.

[4] J. Wenz and S. Karsch, "Physics of Laser-Wakefield Accelerators (LWFA)," 2020, [Online]. Available: http://arxiv.org/abs/2007.04622

[5] W. Horton and T. Tajima, "Laser beat-wave accelerator and plasma noise," *Phys. Rev. A*, vol. 31, no. 6, pp. 3937–3946, 1985, doi: 10.1103/PhysRevA.31.3937.

[6] "SLAC Aerial Photo," Energy.gov. Accessed: Jun. 6, 2023. [Online]. Available: https://www.energy.gov/sites/default/files/styles/full_article_width/public/2017/11/f46/SLAC%20Aerial%20Photo.jpg?itok=ovT3PBzR

[7] T. Tajima and J. M. Dawson, "Laser electron accelerator," *Phys. Rev. Lett.*, vol. 43, no. 4, pp. 267–270, 1979, doi: 10.1103/PhysRevLett.43.267.

[8] Grüner, "Shooting Ahead with Wakefield Acceleration," APS (2019), physics.aps.org/articles/v12/19

[9]   S. Gianfaldoni, R. Gianfaldoni, U. Wollina, J. Lotti, G. Tchernev, and T. Lotti, "An overview on radiotherapy: From its history to its current applications in dermatology," *Open Access Maced. J. Med. Sci.*, vol. 5, no. 4 Special Issue GlobalDermatology, pp. 521–525, 2017, doi: 10.3889/oamjms.2017.122.

[10] R. Polanek *et al.*, "1 kHz laser accelerated electron beam feasible for radiotherapy uses: A PIC–Monte Carlo based study," *Nucl. Instruments Methods Phys. Res. Sect. A Accel. Spectrometers, Detect. Assoc. Equip.*, vol. 987, no. October 2020, 2021, doi: 10.1016/j.nima.2020.164841.

[11] J. D. Jackson, *Classical electrodynamics*, 3rd ed. New York, NY: Wiley, 1999.

[12] F. F. Chen, *Introduction to Plasma Physics and Controlled Fusion*. 2018. doi: 10.1007/978-3-319-22309-4_11.

[13] W. L. Kruer, *The Physics of Laser Plasma Interactions*. 2019. doi: 10.1201/9780429502798.

[14] J. W. H. Peter E. Powers, *Fundamentals of Nonlinear Optics*. 2017. [Online]. Available: https://www.taylorfrancis.com/books/9781315116433

[15] T. T. X. Q. Y. T. Ebisuzaki, *Wakefield acceleration*. Springer Singapore, 2020. doi: 10.1007/s41614-020-0043-z.

[16] McKinstrie, C. J., and R. Bingham. "The Modulational Instability of Coupled Waves." *Physics of Fluids B*, vol. 1, no. 1, 1989, pp. 230–37, doi:10.1063/1.859095.

[17] A. Von Boetticher, R. Walczak, and S. M. Hooker, "Modulational instability in large-amplitude linear laser wakefields," *Phys. Rev. E*, vol. 107, no. 2, pp. 1–6, 2023, doi: 10.1103/PhysRevE.107.L023201.

[18] C. K. Birdsall and A. B. Langdon, *Plasma physics via computer simulation*. 2004. doi: 10.1016/0010-4655(86)90240-7.

[19] Arber, T. D., et al. "Contemporary Particle-in-Cell Approach to Laser-Plasma Modelling." *Plasma Physics and Controlled Fusion*, vol. 57, no. 11, IOP Publishing, 2015, doi:10.1088/0741-3335/57/11/113001.

[20] Berger, M.J., Coursey, J.S., Zucker, M.A., and Chang, J. (2005), *ESTAR, PSTAR, and ASTAR: Computer Programs for Calculating Stopping-Power and Range Tables for Electrons, Protons, and Helium Ions* (version 1.2.3). [Online] Available: http://physics.nist.gov/Star, National Institute of Standards and Technology, Gaithersburg, MD.

[21] F. Salehi *et al.*, "MeV electron acceleration at 1 kHz with10 mJ laser pulses," *Opt. InfoBase Conf. Pap.*, vol. Part F66-F, no. 2, pp. 2–5, 2017, doi: 10.1364/FIO.2017.FM2B.2.

[22] Y. Ma *et al.*, "Polarization-Dependent Self-Injection by Above Threshold Ionization Heating in a Laser Wakefield Accelerator," *Phys. Rev. Lett.*, vol. 124, no. 11, pp. 1–7, 2020, doi: 10.1103/PhysRevLett.124.114801.

[23] S. Sharma, R. K. Khardekar, and H. C. Pant, "Generation of density cavitons in laser produced plasmas," *Phys. Scr.*, vol. 1990, no. T30, pp. 95–106, 1990, doi: 10.1088/0031-8949/1990/T30/014.

[24] N. J. Sircombe, T. D. Arber, and R. O. Dendy, "Accelerated electron populations formed by Langmuir wave-caviton interactions," *Phys. Plasmas*, vol. 12, no. 1, pp. 1–8, 2005, doi: 10.1063/1.1822934.

[25] H.H. Chen and C.S. Liu, "Soliton Formation and Saturation ofDecay Instability of an Electromagnetic Wave into Two Plasma Waves",*Phys. Rev. Let.* vol. 39, no. 14, pp. 881–884, 1977.

[26] P. K. Singh *et al.*, "Electrostatic shock acceleration of ions in near-critical-density plasma driven by a femtosecond petawatt laser," *Sci. Rep.*, vol. 10, no. 1, pp. 1–10, 2020, doi: 10.1038/s41598-020-75455-1.

[27] S. M. Hooker, "Developments in laser-driven plasma accelerators," *Nat. Photonics*, vol. 7, no. 10, pp. 775–782, 2013, doi: 10.1038/nphoton.2013.234.

[28] C. B. Schroeder, "Raman Forward Scattering of High-Intensity Chirped Laser Pulses," pp. 737–750, 2003, doi: 10.1063/1.1524929.

[29] D. Anderson, A. Bondeson, and M. Lisak, "Soliton formation at critical density in laser-irradiated plasmas," *J. Plasma Phys.*, vol. 22, no. 2, pp. 339–352, 1979, doi: 10.1017/S002237780001014X.

[30] N. J. Sircombe, T. D. Arber, and R. O. Dendy, "Local electron acceleration by breaking Langmuir waves The Relativistic Vlasov-Poisson System Cavitons and Phase Space Jets," vol. 28, no. July, pp. 2–5, 2004.

[31] V.V. Vaskov, A.V. Gurevich, and Ya. S. Dimant, "Multiple acceleration of electrons in plasma resonance," *Physics (College. Park. Md).*, vol. 548, no. April 1982, pp. 310–316, 1983.

[33] M. V. Goldman, "Strong turbulence of plasma waves," *Rev. Mod. Phys.*, vol. 56, no. 4, pp. 709–735, 1984, doi: 10.1103/RevModPhys.56.709.

[34] E. Barraza-Valdez, T. Tajima, D. Strickland, and D. E. Roa, "Laser Beat-Wave Acceleration near Critical Density," *Photonics*, vol. 9, no. 7, 2022, doi: 10.3390/photonics9070476.

[35] R. J. Shalloo *et al.*, "Generation of laser pulse trains for tests of multi-pulse laser wakefield acceleration," *Nucl. Instruments Methods Phys. Res. Sect. A Accel. Spectrometers, Detect. Assoc. Equip.*, vol. 829, pp. 383–385, 2016, doi: 10.1016/j.nima.2016.02.044.

[36] D. W. Phillion, D. L. Banner, E. M. Campbell, R. E. Turner, and K. G. Estabrook, "Stimulated Raman scattering in large plasmas," *Phys. Fluids*, vol. 25, no. 8, pp. 1434–1443, 1982, doi: 10.1063/1.863920.

[37] L. Papiez, C. DesRosiers, and V. Moskvin, "Very high energy electrons (50 - 250 MeV) and radiation therapy," *Technol. Cancer Res. Treat.*, vol. 1, no. 2, pp. 105–110, 2002, doi: 10.1177/153303460200100202.

[38] J. Badziak, "Laser-driven ion acceleration: Methods, challenges and prospects," *J. Phys. Conf. Ser.*, vol. 959, no. 1, 2018, doi: 10.1088/1742-6596/959/1/012001.

[39] J.-H. Ha, S. Kim, D. Ryu, and H. Kang, "Effects of Multiscale Plasma Waves on Electron Preacceleration at Weak Quasi-perpendicular Intracluster Shocks," *Astrophys. J.*, vol. 915, no. 1, p. 18, 2021, doi: 10.3847/1538-4357/abfb68.

[40] C. P. Olivier, F. Verheest, and S. K. Maharaj, "A small-Amplitude study of solitons near critical plasma compositions," *J. Plasma Phys.*, vol. 82, no. 6, 2016, doi: 10.1017/S0022377816001082.

[41] W.L. Kruer, J.M. Dawson, and R.N. Sudan, "Trapped particle instability," *Phys. Fluids*, vol. 19, no. 1, pp. 173–174, 1976, doi: 10.1063/1.861306.

[42] R. Bingham *et al.*, "Particle acceleration in lower-hybrid cavitons Particle Acceleration in Lower-Hybrid Cavitons," 1994.

[43] N. Barov, M. E. Conde, W. Gai, and J. B. Rosenzweig, "Propagation of short electron pulses in a plasma channel," *Phys. Rev. Lett.*, vol. 80, no. 1, pp. 81–84, 1998, doi: 10.1103/PhysRevLett.80.81.

[44] A. V. Arefiev, V. N. Khudik, A. P. L. Robinson, G. Shvets, L. Willingale, and M. Schollmeier, "Beyond the ponderomotive limit: Direct laser acceleration of relativistic electrons in sub-critical plasmas," *Phys. Plasmas*, vol. 23, no. 5, 2016, doi: 10.1063/1.4946024.

[45] S. N. Chen *et al.*, "Absolute dosimetric characterization of Gafchromic EBT3 and HDv2 films using commercial flat-bed scanners and evaluation of the scanner response function variability," *Rev. Sci. Instrum.*, vol. 87, no. 7, 2016, doi: 10.1063/1.4954921.

[46] K. Krushelnick *et al.*, "Plasma channel formation and guiding during high intensity short pulse laser plasma experiments," *Phys. Rev. Lett.*, vol. 78, no. 21, pp. 4047–4050, 1997, doi: 10.1103/PhysRevLett.78.4047.

[47] J. Fuchs *et al.*, "Transmission through highly overdense plasma slabs with a subpicosecond relativistic laser pulse," *Phys. Rev. Lett.*, vol. 80, no. 11, pp. 2326–2329, 1998, doi: 10.1103/PhysRevLett.80.2326.

[48] S. Y. Tochitsky *et al.*, "Enhanced acceleration of injected electrons in a laser-beat-wave-induced plasma channel," *Phys. Rev. Lett.*, vol. 92, no. 9, pp. 3–6, 2004, doi: 10.1103/PhysRevLett.92.095004.

[49] B. S. Nicks, T. Tajima, D. Roa, A. Nečas, and G. Mourou, "Laser-wakefield application to oncology," *Int. J. Mod. Phys. A*, vol. 34, no. 34, pp. 1–14, 2019, doi: 10.1142/S0217751X19430164.

[50] J. Cowley *et al.*, "Excitation and Control of Plasma Wakefields by Multiple Laser Pulses," *Phys. Rev. Lett.*, vol. 119, no. 4, pp. 1–6, 2017, doi: 10.1103/PhysRevLett.119.044802.

[51] I. V. Pogorelsky *et al.*, "Laser energy conversion to solitons and monoenergetic protons in near-critical hydrogen plasma," *IPAC 2010 - 1st Int. Part. Accel. Conf.*, pp. 4446–4448, 2010.

[52] C. M. Tang, P. Sprangle, and R. N. Sudan, "Excitation of the plasma waves in the laser beat wave accelerator," *Appl. Phys. Lett.*, vol. 45, no. 4, pp. 375–377, 1984, doi: 10.1063/1.95225.

[53] M. N. Rosenbluth and C. S. Liu, "Excitation of plasma waves by two laser beams," *Phys. Rev. Lett.*, vol. 29, no. 11, pp. 701–705, 1972, doi: 10.1103/PhysRevLett.29.701.

[54] P. Chen and R. D. Ruth, "A comparison of the plasma beat wave accelerator and the plasma wake field accelerator," vol. 1985, no. March, pp. 213–225, 2008, doi: 10.1063/1.35302.

[55] T. Y. B. Yang, W. L. Kruer, R. M. More, and A. B. Langdon, "Absorption of laser light in overdense plasmas by sheath inverse bremsstrahlung," *Phys. Plasmas*, vol. 2, no. 8, pp. 3146–3154, 1995, doi: 10.1063/1.871146.

[56] J. D. Lawson, "Beat-wave accelerator studies at the Rutherford Appleton Laboratory," vol. 120, no. 1985, pp. 120–129, 2008, doi: 10.1063/1.35317.

[57] O. Jakobsson, S. M. Hooker, and R. Walczak, "Gev-Scale Accelerators Driven by Plasma-Modulated Pulses from Kilohertz Lasers," *Phys. Rev. Lett.*, vol. 127, no. 18, p. 184801, 2021, doi: 10.1103/PhysRevLett.127.184801.

[58] J. Faure *et al.*, "A review of recent progress on laser-plasma acceleration at kHz repetition rate," *Plasma Phys. Control. Fusion*, vol. 61, no. 1, 2019, doi: 10.1088/1361-6587/aae047.

[59] A. E. Hussein *et al.*, "Towards the optimisation of direct laser acceleration," *New J. Phys.*, vol. 23, no. 2, pp. 0–13, 2021, doi: 10.1088/1367-2630/abdf9a.

[60] F. Sylla *et al.*, "Short intense laser pulse collapse in near-critical plasma," *Phys. Rev. Lett.*, vol. 110, no. 8, pp. 1–5, 2013, doi: 10.1103/PhysRevLett.110.085001.

[61] R. Focia, D. Montgomery, J. Fernández, and R. Johnson, "Observation of Multiple Cascade Steps of the Langmuir Decay instability in a laser plasma," no. July, 2001, [Online]. Available: http://www.researchgate.net/publication/237744532_OBSERVATION_OF_MULTIPLE_CASCADE_STEPS_OF_THE_LANGMUIR_DECAY_INSTABILITY_IN_A_LASER_PLASMA/file/5046352b2579779248.pdf

[62] K. M. M. Rafi, B. A. H. Fahd, M. Deepu, and G. Rajesh, *Experimental and Numerical Studies on the Plume Structure of Micro-nozzles Operating at High-Vacuum Conditions*. 2019. doi: 10.1007/978-3-319-91020-8_111.

[63] S. Heuraux and G. Leclert, "Generalized Zakharov equations for a streaming or drifting plasma," *Plasma Phys. Control. Fusion*, vol. 36, no. 6, pp. 991–996, 1994, doi: 10.1088/0741-3335/36/6/003.

[64] M. Roth and M. Schollmeier, "Ion Acceleration - Target Normal Sheath Acceleration (CERN Yellow Reports)," *Proc. CAS-CERN Accel. Sch. Plasma Wake Accel. Geneva, Switz.*, vol. 001, no. November 2014, p. Volume 1 231-270, 2016.

[65] B. S. Nicks, T. Tajima, D. Roa, A. Nečas, and G. Mourou, "Laser-wakefield application to oncology," *Int. J. Mod. Phys. A*, vol. 34, no. 34, pp. 1–14, 2019, doi: 10.1142/S0217751X19430164.

[66] B. Gonzalez-Izquierdo *et al.*, "Optically controlled dense current structures driven by relativistic plasma aperture-induced diffraction," *Nat. Phys.*, vol. 12, no. 5, pp. 505–512, 2016, doi: 10.1038/nphys3613.

[67] D. R. Welch, T. C. Genoni, C. Thoma, D. V. Rose, and S. C. Hsu, "Particle-in-cell simulations of laser beat-wave magnetization of dense plasmas," *Phys. Plasmas*, vol. 21, no. 3, 2014, doi: 10.1063/1.4868225.

[68] S. Perri, A. Bykov, H. Fahr, H. Fichtner, and J. Giacalone, "Recent Developments in Particle Acceleration at Shocks: Theory and Observations," *Space Sci. Rev.*, vol. 218, no. 4, 2022, doi: 10.1007/s11214-022-00892-5.

[69] C. Gong, S. Y. Tochitsky, F. Fiuza, J. J. Pigeon, and C. Joshi, "Plasma dynamics near critical density inferred from direct measurements of laser hole boring," *Phys. Rev. E*, vol. 93, no. 6, pp. 1–6, 2016, doi: 10.1103/PhysRevE.93.061202.

[70] A. Bigongiari, M. Raynaud, C. Riconda, A. Héron, and A. MacChi, "Efficient laser-overdense plasma coupling via surface plasma waves and steady magnetic field generation," *Phys. Plasmas*, vol. 18, no. 10, 2011, doi: 10.1063/1.3646520.

[71] A. V. Arefiev, G. E. Cochran, D. W. Schumacher, A. P. L. Robinson, and G. Chen, "Temporal resolution criterion for correctly simulating relativistic electron motion in a high-intensity laser field," *Phys. Plasmas*, vol. 22, no. 1, 2015, doi: 10.1063/1.4905523.

[72] [1]   Y. J. Gu, Q. Kong, Y. Y. Li, H. Y. Ban, Z. Zhu, and S. Kawata, "Steady plasma channel formation and particle acceleration in an interaction of an ultraintense laser with near-critical density plasma," *Phys. Plasmas*, vol. 18, no. 3, 2011, doi: 10.1063/1.3559463.

[73] [1]   Y. Wu, G. Jain, T. Sizyuk, X. Wang, and A. Hassanein, "Dynamics of laser produced plasma from foam targets for future nanolithography devices and X-ray sources," *Sci. Rep.*, vol. 11, no. 1, pp. 1–14, 2021, doi: 10.1038/s41598-021-93193-w.

[74] F. Albert and A. G. R. Thomas, "Applications of laser wakefield accelerator-based light sources," Plasma Phys. Control. Fusion, vol. 58, no. 10, 2016.

[75] V. I. Eremin, A. V. Korzhimanov, and A. V. Kim, "Relativistic self-induced transparency effect during ultraintense laser interaction with overdense plasmas: Why it occurs and its use for ultrashort electron bunch generation," Phys. Plasmas, vol. 17, no. 4, 2010.

[76] C. M. Lazzarini et al., "50 MeV electron beams accelerated by a terawatt scalable kHz laser," pp. 1–9, 2023.

[77] S. Chakraborty, G. Pakira, and A. Roy Chowdhury, "On the Envelope Soliton near Critical Density in a Plasma with Cold Ions and Two-Temperature Electrons," Il Nuovo Cimento D, **15**, 1043–1051 (1993).

[78] J. Zhang *et al.*, "Multiple beam two-plasmon decay: Linear threshold to nonlinear saturation in three dimensions," *Phys. Rev. Lett.*, vol. 113, no. 10, pp. 1–5, 2014, doi: 10.1103/PhysRevLett.113.105001.

[79] E. Esarey, P. Sprangle, J. Krall, and A. Ting, "Overview of plasma-based accelerator concepts," *IEEE Trans. Plasma Sci.*, vol. 24, no. 2, pp. 252–288, 1996, doi: 10.1109/27.509991.

[80] P. Gibbon, "Introduction to plasma physics," *CAS-CERN Accel. Sch. Plasma Wake Accel. 2014, Proc.*, vol. 001, no. November 2014, pp. 51–65, 2014, doi: 10.5170/CERN-2016-001.51.